UAV Icing: Numerical and Experimental Study of Performance Penalties on an RG-15 Airfoil

Master's thesis
by
Johannes Wolfgang Oswald

Institute for Aerodynamics and Gas Dynamics
of the University Stuttgart
&
Environmental and Applied Fluid Dynamics Department of the von Karman Institute for Fluid Dynamics
in Sint-Genesius-Rode, Belgium
&
Department of Engineering Cybernetics
of the Norwegian University of Science and Technology

Stuttgart, May 2021

Universität Stuttgart

Institut für Aerodynamik und Gasdynamik
Direktor: Prof. Dr.-Ing. Ewald Krämer

IAG

Masterarbeit
für Herrn Johannes Oswald
(durchgeführt am VKI unter Mitbetreuung der NTNU)

UAV Icing: Numerical and Experimental Study of Performance Penalties on an RG-15 Airfoil

A key limitation to the operational envelope of medium-sized fixed-wing unmanned aerial vehicles (UAVs) today is the risk of atmospheric in-flight icing. In contrast to icing in manned aviation, UAV icing is not well established and is an emerging research topic. The Norwegian University of Science and Technology (NTNU) in collaboration with the von Karman Institute for Fluid Dynamics (VKI) offer an experimental master thesis on UAV icing.

The main objective of this project is to provide experimental data on the performance penalties of ice shapes on a typical UAV airfoil for low Reynolds numbers and to compare them to numerical simulations. Wind tunnel experiments will be conducted on an RG-15 airfoil at low Reynolds numbers (ca. 600,000-1,200,000), as is typical for UAV cruise speeds. The experimental tests will be conducted at the conventional wind tunnels at VKI. First, the baseline aerodynamic performance of the clean wing will be measured. Then, artificial, 3D printed ice shapes will be used to determine the performance penalties (lift, drag, stall, moment) of the ice. The experimental data will be compared to computational fluid dynamic (CFD) simulations with ANSYS FENSAP-ICE. The thesis is to be conducted in English at VKI in Rhode-Saint-Genese, Belgium.

Tasks:

- Literature study on aerodynamics of iced UAV airfoils and experimental methods
- Wind tunnel experiments to determine lift, drag, stall, moments on the clean RG-15
- Lift, drag, stall, moment measurements on 3-6 different 3D printed ice shapes, depending on tunnel availability. Pressure measurements if the wing model allows it
- Investigation of transition sensitivity of the airfoil
- Option of using particle image velocimetry (PIV) methods, depending tunnel availability
- CFD simulation of the clean and iced geometries in 2D and comparison to experiments
- Critical discussion of results

Die Arbeit wird am VKI in Rhode-Saint-Genese (Belgien) unter Mitbetreuung der NTNU in Trondheim (Norwegen) durchgeführt.

Betreuerin seitens des VKI:	Adriana Enache
Betreuer seitens NTNU:	Dipl.-Ing. Richard Hann
Betreuer seitens des IAGs:	Dr.-Ing. Thorsten Lutz, MSc. Jonas Romblad
Ausgabetermin:	2.11.2020
Spätester Abgabetermin:	30.4.2021

Prof. Dr.-Ing. Ewald Krämer

Erklärung

Hiermit versichere ich, dass ich diese Masterarbeit selbstständig mit Unterstützung des Betreuers / der Betreuer angefertigt und keine anderen als die angegebenen Quellen und Hilfsmittel verwendet habe.

Die Arbeit oder wesentliche Bestandteile davon sind weder an dieser noch an einer anderen Bildungseinrichtung bereits zur Erlangung eines Abschlusses eingereicht worden.

Ich erkläre weiterhin, bei der Erstellung der Arbeit die einschlägigen Bestimmungen zum Urheberschutz fremder Beiträge entsprechend den Regeln guter wissenschaftlicher Praxis[1] eingehalten zu haben. Soweit meine Arbeit fremde Beiträge (z.B. Bilder, Zeichnungen, Textpassagen etc.) enthält, habe ich diese Beiträge als solche gekennzeichnet (Zitat, Quellenangabe) und eventuell erforderlich gewordene Zustimmungen der Urheber zur Nutzung dieser Beiträge in meiner Arbeit eingeholt. Mir ist bekannt, dass ich im Falle einer schuldhaften Verletzung dieser Pflichten die daraus entstehenden Konsequenzen zu tragen habe.

.....

Ort, Datum, Unterschrift

Statement of Originality

This thesis has been performed independently with support of my supervisor/s. It contains no material that has been accepted for the award of a degree at this or any other university. To the best of my knowledge and belief, this thesis contains no material previously published or written by another person except where due reference is made in the text.

I further declare that I have performed this thesis according to the existing copyright policy and the rules of good scientific practice. In case this works contains contributions of someone else (e.g. pictures, drawings, text passages etc.), I have clearly identified the source of these contributions, and, if necessary, have obtained approval from the originator for making use of them in this thesis. I am aware that I have to bear the consequences in case I have contravened these duties.

[1] Nachzulesen in den DFG-Empfehlungen zur "Sicherung guter wissenschaftlicher Praxis" bzw. in der Satzung der Universität Stuttgart zur "Sicherung der Integrität wissenschaftlicher Praxis und zum Umgang mit Fehlverhalten in der Wissenschaft"

Acknowledgements

My special thanks are dedicated to my supervisors Dr. Richard Hann (NTNU), PhD candidate Adriana Enache (VKI) and Dr.-Ing. Thorsten Lutz (IAG) for their support and guidance throughout my master's thesis.

I wish to thank Prof. van Beeck (VKI) and Jonas Romblad (IAG) for vivid discussions on the topic.

I would like to thank the technical engineer Gert-Jan Glabeke (VKI) and the technical staff of the VKI for their help on operating and preparing the wind tunnel experiments.

It was an honour and pleasure for me to get the opportunity of working together with the named colleagues and to conduct my experiments inside the huge L1-B wind tunnel.

Finally, I do not want to miss the chance of expressing my thankfulness for the unconditional support of my beloved Daniela and family, which helped me a lot in sometimes frustrating times to refocus and refresh my mindset.

Contents

Nomenclature

Acronyms

2D	Two-dimensional
3D	Three-dimensional
AoA	Angle of attack
AoAc	Corrected angle of attack
CFD	Computational fluid dynamic simulations
FAA	Federal Aviation Administration, USA
F3B	Competition class of radio controlled model sailplanes
FAI	World air sports federation
IAG	Institute for Aerodynamics and Gas Dynamics of the University of Stuttgart
L/D	Lift force to drag force ratio
LS	Lower airfoil side
LSB	Laminar separation bubble
LWC	Liquid water content
MVD	Droplet median volume diameter
NTNU	Norwegian University of Science and Technology, Trondheim, Norway
RANS	Reynolds-averaged Navier-Stokes equations
SLD	Supercooled large droplets
SR	Surface roughness
UAV	Unmanned aerial vehicles
US	Upper airfoil side
USA	United States of America
VKI	Von Karman Institute for Fluid Dynamics, Sint-Genesius-Rode, Belgium
VTT	Technical Research Centre of Finland Ltd, Espor, Finland

Roman symbols

$\mathbf{A}$	[6x6]	Balance calibration matrix
AR	[-]	Aspect ratio of an airfoil
b	[m]	Wing model span-width
c	[m]	Chord length
δc	[m]	Uncertainty of the chord length
c_d	[-]	Drag coefficient

c_{d_0}	[-]	Drag coefficient at zero lift
δc_d	[-]	Uncertainty of the drag coefficient
Δc_d	[-]	Jacob's drag coefficient correction
$\Delta c_{d,min}$	[%]	Minimum drag coefficient penalty
$\Delta c_{d,-1.3}$	[%]	Drag coefficient penalty at -1.3°
c_l	[-]	Lift coefficient
c_{l_α}	[-]	Local slope of the lift coefficient versus angle of attack
$c_{l_{\alpha_0}}$	[-]	Slope of the lift coefficient versus angle of attack near zero lift
δc_l	[-]	Uncertainty of the lift coefficient
$\Delta c_{l,max}$	[%]	Maximum lift coefficient penalty
$\Delta c_{l,-1.3}$	[%]	Lift coefficient penalty at -1.3°
c_m	[-]	Pitching moment coefficient
δc_m	[-]	Uncertainty of the pitching moment coefficient
$\Delta\delta c_m$	$\left[\frac{1}{\text{rad}}\right]$	Slope of the moment coefficient penalty
$\Delta c_{m,-1.3}$	[%]	Moment coefficient penalty at -1.3°
c_p	[-]	Local pressure coefficient
δc_p	[-]	Uncertainty of the local pressure coefficient
D	[N]	Drag force
ΔD	[N]	Total error of the drag force measurement
E	[J]	Total energy
$F_{indexed}$	[N]	Balance load measurement
g	$\left[\frac{m}{s^2}\right]$	Gravity acceleration constant
h	[m]	Height
H	[J]	Total enthalpy
$\vec{F}_{loads}$	[1x6]	Balance load readout vector
k	$\left[\frac{W}{mK}\right]$	Thermal conductivity coefficient
K	$\left[\frac{J}{kg}\right]$	Turbulent kinetic energy
l	[m]	Distance between calibration resolve centre and wing quarter point
L	[N]	Lift force
ΔL	[N]	Total error of the lift force measurement
L/D	[-]	Lift to drag ratio
$\delta L/D$	[-]	Uncertainty of the lift to drag ratio
$\Delta L/D$	[%]	Maximum lift to drag ratio penalty
$\Delta L/D_{-1.3}$	[%]	Lift to drag ratio penalty at -1.3°
M	[Nm]	Pitching moment
ΔM	[Nm]	Total error of the pitching moment measurement
$M_{indexed}$	[Nm]	Moment
Ma	[-]	Mach number
n	[-]	Number of calibration runs

N	[-]	Number of samples
p	[Pa]	Pressure
p_0	[Pa]	Total pressure
p_{amb}	[Pa]	Ambient pressure
δp_{amb}	[Pa]	Uncertainty of the ambient pressure
Δp_i	[Pa]	Total error of the pressure measurement
p_s	[Pa]	Free stream static pressure
q	[Pa]	Dynamic pressure
δq	[Pa]	Uncertainty of the dynamic pressure
R	$\left[\frac{J}{kgK}\right]$	Specific gas constant
Ra	[m]	Surface roughness
Re	[-]	Reynolds number
Δs	[m]	Initial wall spacing
S	$\left[m^2\right]$	Wing/airfoil reference area
δS	$\left[m^2\right]$	Uncertainty of the wing/airfoil reference area
S_{ij}	[3x3]	Strain-rate tensor
T	[K]	Absolute static temperature
T_{acc}	[℃]	Ice accretion temperature
T_{amb}	[K]	Ambient temperature
t	[m]	Airfoil maximum thickness
t_{acc}	[s]	Ice accretion time
$\vec{U}_{cells}$	[1x6]	Balance voltage readout vector
v_∞	$\left[\frac{m}{s}\right]$	Free stream velocity
δv_∞	$\left[\frac{m}{s}\right]$	Uncertainty of the free stream velocity calculation
v_i	$\left[\frac{m}{s}\right]$	Velocity component in one Cartesian coordinate direction
$y+$	[-]	Dimensionless wall distance of the nearest wall grid point
x, y, z	[m]	Cartesian coordinates

Greek symbols

α	[°]	Angle
$\Delta\alpha_{c_{d,min}}$	[°]	Angle penalty at the minimum drag coefficient
$\Delta\alpha_{c_{l,max}}$	[°]	Angle penalty at the maximum lift coefficient
$\Delta\alpha_{L/D}$	[°]	Angle penalty of the maximum lift to drag ratio
δ	[m]	Boundary layer thickness
δ_{ij}	[3x3]	Kronecker symbol; a second-order 3x3 identity matrix tensor
ε	[m]	Equivalent sand-grain roughness
$\triangle\eta_i$	[%]	Balance relative precision per load measuring cell
μ	$\left[\frac{kg}{ms}\right]$	Dynamic viscosity coefficient

μ_T	$\left[\frac{m^2}{s}\right]$	Eddy viscosity
$\tilde{\nu}$	$\left[\frac{m^2}{s}\right]$	Modified eddy viscosity
ν	$\left[\frac{m^2}{s}\right]$	Kinematic viscosity
ν_L	$\left[\frac{m^2}{s}\right]$	Laminar kinematic viscosity
$\Delta\xi$	[Pa], [N], [Nm]	Total error of a measurement chain
$\Delta\xi_{AMS5812}$	[Pa]	Pressure sensor manufacturing error
ξ_{bias}	[Pa], [N], [Nm]	Bias error of a measurement
$\Delta\xi_{calibration}$	[Pa]	Pressure sensor calibration error
ξ_{random}	[Pa], [N], [Nm]	Random or systematic error of a measurement
ρ	$\left[\frac{kg}{m^3}\right]$	Density
$\delta\rho$	$\left[\frac{kg}{m^3}\right]$	Uncertainty of the density calculation
σ	[-]	Airfoil geometry factor
$\sigma_{indexed}$	[Pa], [N], [Nm]	Standard deviation of a measurement
$\Delta\varsigma_i$	[%]	Balance accuracy per load measuring cell
τ	[-]	Tunnel geometry factor
τ_{ij}	[3x3]	Viscous stress tensor
${\tau_{ij}}^R$	[3x3]	Reynolds-stress tensor
Λ	[-]	Airfoil geometry factor
Ω_{ij}	[3x3]	Rotation-rate tensor

List of Figures

List of Tables

Übersicht

Die vorliegende Arbeit befasst sich mit der Evaluation von aerodynamischen Einschränkungen, die ein typisches unbemanntes Flugobjekt-Profil (UAV-Profil) durch Flügelvorderkanteneis erfährt. Das hierbei untersuchte RG-15-Profil ist spezialisiert auf einen Operationsbereich mit niedrigen Reynolds-Zahlen und seine aerodynamische Charakteristik ist auf die der Profile von mittelgroßen Starrflügler-UAVs übertragbar. Motiviert durch fehlende experimentelle Validierungsdaten für die Anwendung existierender numerischer Programme der generellen Luftfahrt auf den Operationsbereich des genannten UAV-Typs sind experimentelle und numerische Studien angefertigt worden. Der stetig wachsende kommerzielle und militärische UAV-Marktanteil fördert zudem das Interesse an der Forschung zu Flugbereichsgrenzen der UAVs. Einer der Schlüsselfaktoren, der den Flugbereich der UAVs beeinträchtigt, ist die Vereisung der UAVs während des Fluges. Um die effiziente Entwicklung von Anti-Vereisungstechnologien zu ermöglichen, müssen zuvor die existierenden numerischen Methoden für den Operationsbereich der mittelgroßen Starrflügler-UAVs validiert werden. Aus diesem Grund sind die Ziele dieser Arbeit, sowohl experimentelle Daten zu den aerodynamischen Einschränkungen von Flügelvorderkantenvereisung im Flug zu generieren als auch numerische Simulationen mit dem FENSAP-Modul von ANSYS anzufertigen und diese mit den ermittelten experimentellen Daten zu vergleichen. Diesen Aufgaben widmete sich ein Konsortium aus drei Institutionen: das Institut für Aerodynamik und Gasdynamik (IAG) der Universität Stuttgart, das Department of Engineering Cybernetics der Norwegian University of Science and Technology (NTNU) und das Environmental and Applied Fluid Dynamics Department des von Karman Institutes for Fluid Dynamics (VKI) in Rhode-Saint-Genese, Belgien.

Die experimentelle Messkampagne fand im großen Windkanal L1-B des VKIs statt und es wurden hierbei drei unterschiedliche Eistypen und drei Reynolds-Zahlbereiche untersucht. Die Reynolds-Zahlbereiche sind angesiedelt bei 200.000, 400.000, und 750.000 und spiegeln somit typisch auftretende Reynolds-Zahlen des untersuchten UAV-Typs wieder. Zum Erreichen einer möglichst zweidimensionalen (2D) Profilumströmung des verwendeten UAV-Profils ist ein in der Breite kleinerer 2D-Windkanalabschnitt innerhalb der größeren Testsektion des L1-B konstruiert worden. Das RG-15-Windkanalmodell wurde zudem auf der Ober- und Unterseite mit jeweils 23 Druckmesslöchern versehen und die wirkenden aerodynamischen Kräfte wurden mit einer Sechskomponenten-Plattformwaage gemessen. Als Eistypen kamen dreidimensional (3D) gedruckte, extrapolierte 2D-Schnitte von Eisflächen aus drei unterschiedlichen Vereisungsbedingungen zum Einsatz. Diese sind von der NTNU aus früheren Vereisungsexperimenten von UAV-Flügeln zur Verfügung gestellt worden. Die verwendeten Eistypen sind "Glaze", "Rime" und "Mixed"-Eisflächen und weisen unterschiedlich stark ausgeprägte Verwerfungen auf. Das reine RG-15-Profil wurde mit einer Winkelauflösung von 3° zwischen den Anstellwinkeln (AoA) -7,3°<AoA<13,8° als Referenzfall getestet. Ab einem Anstellwinkel von AoA=7,8° wurde die Winkelauflösung auf 1° erhöht, um das Strömungsabrissverhalten zu untersuchen. Jeder der 3D-gedruckten Eistypen wurde an der Flügelvorderkante befestigt. Das künstliche Glaze-Eis ist mit einer Winkelauflösung von 3° zwischen -7,3°<AoA<7,8° und mit einer Winkelauflösung von 1° zwischen 7,8°<AoA<9,8° in den Reynolds-Zahlbereichen von 200.000 und 400.000 getestet worden. Alle drei Eistypen wurden in allen drei Reynolds-Zahlbereichen unter einem Anstellwinkel von -1.3°getestet. Die Auswertung der experimentell ermittelten aerodynamischen Koeffizienten zeigt

auf, dass das Glaze-Eis die höchsten aerodynamischen Einschränkungen verursacht. Der minimale Widerstand des reinen RG-15-Windkanalmodells bei einer Reynolds-Zahl von 750.000 wurde durch das Anbringen des Glaze-Eismodells um +130%, durch das Mixed-Eismodell um +117% und durch das Rime-Eismodell um +92% erhöht. Hierbei trat die Analogie auf: je höher die Reynolds-Zahl, desto höher der minimale Widerstand des reinen RG-15-Windkanalmodells durch die Anbringung des jeweiligen Eismodells. Zudem verursachte das Glaze-Eismodell ein destabilisierendes abnickendes Moment.

Numerisch wurde die experimentelle Messkampagne mit dem FENSAP-Modul von ANSYS durchgeführt. Als Turbulenzmodell diente das Spalart-Allmaras-Modell. Der Strömungsumschlag von laminarer zu turbulenter Strömung wurde für die 2D-Reynolds-gemittelten Navier-Stokes (RANS) computergestützten fluid-dynamischen (CFD) Simulationen des reinen RG-15-Profils vorgegeben. Eine Validierung der hybriden O-Vernetzung fand mithilfe von experimentellen Literaturdaten bei einer Reynolds-Zahl von 200.000 statt. Ein Vergleich der CFD-Simulationen mit den im Zuge dieser Arbeit durchgeführten Experimenten zeigt Limitierungen des gewählten Simulationsansatzes bezüglich der Vorhersage des erreichten maximalen Auftriebs und Strömungsabrissverhaltens auf. Der Widerstandskoeffizient wurde insgesamt zu niedrig widergespiegelt. Allerdings sind deutliche Anzeichen für eine Kontaminierung der gemessenen Widerstandsbeiwerte durch 3D-Strömungsinteraktionen mit den Grenzschichten der Windkanalwände vorhanden. Ein Vergleich mit anderen Experimenten aus der Literatur zum Thema der aerodynamischen Einschränkungen durch Vereisung zeigt auf, dass das gewählte Spalart-Allmaras-Turbulenzmodell möglicherweise ungeeignet für den betrachteten niedrigen Reynolds-Zahlbereich ist. Es wird dahingehend nahegelegt, weitere Untersuchungen mit Turbulenzmodellen höherer Ordnung durchzuführen, sowie in zukünftigen Messkampagnen auch Strömungsvisualisierungstechniken einzusetzen. Ebenso sind einige Verbesserungen des methodischen Ansatzes der durchgeführten experimentellen Messkampagne vorgeschlagen worden, um weitere fundierte Daten für die fortlaufende Validierung der numerischen Modelle der generellen Luftfahrt für den Anwendungsbereich der mittelgroßen Starrflügler-UAVs zu generieren.

Abstract

A key limitation to the operational envelope of medium-sized fixed-wing unmanned aerial vehicles (UAVs) today is the risk of atmospheric in-flight icing. This type of UAV with a wingspan of up to several meters requires an all-weather capability for long-endurance and long-range missions. In contrast to icing in manned aviation, UAV icing is not well established and is an emerging research topic. Previous numerical and experimental studies showed especially at the UAV's low Reynolds number regimes significant aerodynamic penalties ranging from ice-accretion on the wing leading edges and propellers. This encourages the development of ice protection systems also for UAVs, which relies on efficient and validated numerical tools. A cooperation consisting out of the Department of Engineering Cybernetics of the Norwegian University of Science and Technology (NTNU), the Environmental and Applied Fluid Dynamics Department of the von Karman Institute for Fluid Dynamics (VKI) and the Institute for Aerodynamics and Gas Dynamics (IAG) of the University of Stuttgart, is aiming to contribute to the ongoing validation process of established numerical tools of the manned aviation also for the one order of magnitude lower Reynolds number regimes of medium-sized fixed-wing UAVs. To achieve the main objective, an experimental study inside the largest wind tunnel facility of the VKI, a numerical study of the experiments with the ANSYS FENSAP module, and a final comparison of both campaign results are conducted for the purpose of evaluating the ice-induced aerodynamic performance penalties.

The experimental study was initially set out to test angular sweeps of 3D-printed artificial glaze, rime and mixed ice shapes, installed at the leading edge of an RG-15 airfoil at Reynolds number regimes of 200,000, 400,000, and 750,000 to mostly cover general UAV flight envelopes. Ultimately, it was only possible to perform the angular sweep for the glaze ice shape at the Reynolds numbers regimes of 200,000 and 400,000. Nevertheless, each ice shape was tested at all three Reynolds number regimes at an angle of attack of -1.3°. Two dimensional and steady-state Reynolds-averaged Navier-Stokes equations simulations (RANS) were conducted with the ANSYS FENSAP module to analyse the aerodynamic parameters of the baseline and the iced airfoil. The comparison of the conducted numerical and experimental study is regarded to be a key element to contribute to the validation of the ANSYS FENSAP module for the low Reynolds number regimes of typical UAV flight envelopes. The results indicated that the chosen one-equation Spalart-Allmaras turbulence model has a limited capability of capturing the onset of stall behaviour and achievable maximum lift of the clean and artificial iced RG-15 airfoil, but is in general able to predict the order of the induced drag and moment penalties.

1. Introduction

Forecasts of unmanned aerial vehicle (UAV) market growth rates may differ in numbers, but are overall agreeing on predicting an annual growth rate between 10% and 25% from 2014 to 2025 [22, 41]. A recently published report from the Federal Aviation Administration (FAA) [22] reveals a noteworthy difference of the private and commercial UAV sector in the United States of America (USA). According to the report, the private sector is predicted to most likely stagnate at a stable level of 1.4 million units aloft by the end of 2023. In contrast to that, the commercial non-model aircraft market is estimated to triple from 277,000 units in 2018 up to 835,000 in 2023. The FAA mentions amongst other things the limited mission profile of the private sector and diminishing unit prices to be the reasons behind this trend. Consequently, the commercial UAV missions are typically more diverse: Around 21% of the commercial missions today are covered by research, development, and training. Another 21% are filming and entertainment missions, followed with approximately 16% by industrial and environmental missions [22]. With improved technology in e.g. battery life and safety, as well as more clarified flight regulations and authorisations by the national institutions, the operational portfolio of non-model unmanned aircrafts will be able to expand. Conceivable future applications could be e.g. blood deliveries to hospitals, commercial package deliveries, search-and-rescue operations, and wireless networking applications [22, 47].

Besides the technical and regulatory limitations, another key limitation to the operational envelope of medium-sized fixed-wing UAVs today is the risk of atmospheric in-flight icing [25]. Motivated by icing-related accidents of aircrafts and limited available information on several icing parameters evaluated Bernstein et al. [11] icing conditions aloft for Canada and the continent of the United States. Especially in the highly populated areas of the eastern and western USA remains the risk of atmospheric in-flight icing in summer 10% and rises up to 60% for the winter months. In a follow-up paper, Bernstein et al. [10] analysed the icing conditions aloft over Europe, Asia and the Globe. Restricted to Europe, the full year icing frequency is above 15%, but reaches farther North over 55% for e.g. Norway. Especially the risk of supercooled large droplets (SLD) is peaking over the northern European countries like Great Britain and Norway with a frequency of 14% [10]. SLD icing conditions are particularly hazardous, because they typically lead to large ice-covered lifting surface areas. This is caused by the possible occurrence of significantly higher ice-accretion rates within the SLD icing conditions compared to in-cloud icing [25]. The evaluated icing condition altitudes by Bernstein et al. [10] over Europe are similar to the ones reported by Politovich [38]: Icing conditions can occur between 0m and 6000m above sea level. In winter, the icing condition frequency is up to 40% at heights between 0m and 2000m, while in summer the altitudes for icing condition occurrence generally raises but remains above 15% between 3000m and 5000m. These altitudes are well in range of today's medium-sized fixed wing UAV flight envelopes with ceiling heights between 5500m and 6000m [25]. This is why these typically long-endurance and long-range UAVs are requiring an all weather capability [23]. Furthermore, the all weather capability requirement motivates ice protection technologies for UAVs like the "D•ICE" system by the Norwegian company UBIQ Aerospace [40]. Since the existing icing simulation tools are validated for manned aviation operating typically at Reynolds numbers one order of magnitude higher than UAVs [23], the enabling of the ice protection technologies for UAVs still requires the validation of the numerical methods onto the low Reynolds

number UAV-applications as recommended by Hann and Johansen [25].

In flight-icing of an UAV or any other aircraft is described as the process of accretion of freezing liquid droplets, when they are impinging onto the UAV fuselage, propeller, sensors, etc.. The UAV is prone to in-flight icing, when the flightpath is passing through clouds or precipitations [25]. On average, icing environments have been reported by pilots to set place at altitudes around 3000m up to 6000m above mean sea level [38], but can also occur in the first 1000m to 2000m above the ground [11, 10]. The icing environment is mostly dependant on the ambient temperature and the airspeed [24]. However, for defining the accreting ice topology, the liquid water content, the droplet size and the accretion time are playing also an important role [24]. Under certain icing conditions inside SLD clouds, so called freezing clouds, different ice shape morphologies form: glaze, rime, and mixed ice. A fourth ice shape accretion, which occurs more rarely, is taking place in freezing precipitations and is characterized by SLD icing [24].

Glaze ice shapes typically accrete, when the temperatures are near the freezing point and the droplets do not directly freeze on impact with a cold surface. Instead, the accumulating liquid water film gradually freezes on the surface and a clear ice with a smooth surface accretes [25]. The irregularly accreting glaze ice can exhibit large *horn-ice* shapes with key geometry parameters like horn angle, size, and location. Large flow separation regions and bubbles characterise the flow-field, which are growing with increasing angle of attack (AoA) and resulting in high aerodynamic penalties [13].

If the air temperature is low enough to let liquid droplets instantly freeze while impinging on a cold surface, *rime ice* shapes typically accrete. Enclosed tiny air-bubbles are responsible for the white, opaque appearance of the rime ice [25]. The resulting topology and aerodynamic flow features can be associated with Bragg et al.'s [13] contour following *streamwise ice*. The aerodynamics are not as much affected by the streamwise ice compared to the horn ice, because the resulting separation bubble is typically small compared to horn-ice induced ones and the aerodynamic penalties are less severe [13].

A transition between the icing conditions to form glaze and rime ice shapes often causes *mixed ice* shapes to accrete. Herein, the droplets only partially freeze on impact and at the same time a liquid water film arises on the surface. This results in a mixture of ice geometries to accrete, ranging from horn-like features to more streamwise elements [25]. Especially in icing conditions provoking the accretion of mixed and glaze ice shapes, *spanwise-ridge ice* can form farther downstream of the airfoil and act like a flow obstacle. If also horn-ice features are present, separation regions are formed down- and up-stream of the ridge and can effect the airfoil performance to a great extend [13]. The three ice topologies: horn, streamwise and spanwise-ridge ice are displayed schematically in Figure 1.1 and were adapted from Bragg et al. [13] by Hann [25]. In comparison, Hann's Figures 1.2 until 1.5 [24] are showing accreted ice profiles of glaze, rime and mixed ice shapes.

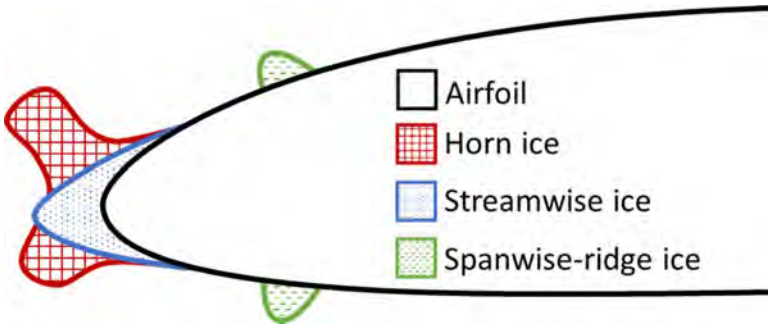

Fig. 1.1.: Typical Ice morphologies on an airfoil. From Hann and Johansen (2020) [25].

Fig. 1.2.: Profile of glaze ice on an airfoil. Photo from Hann (2020) [24].

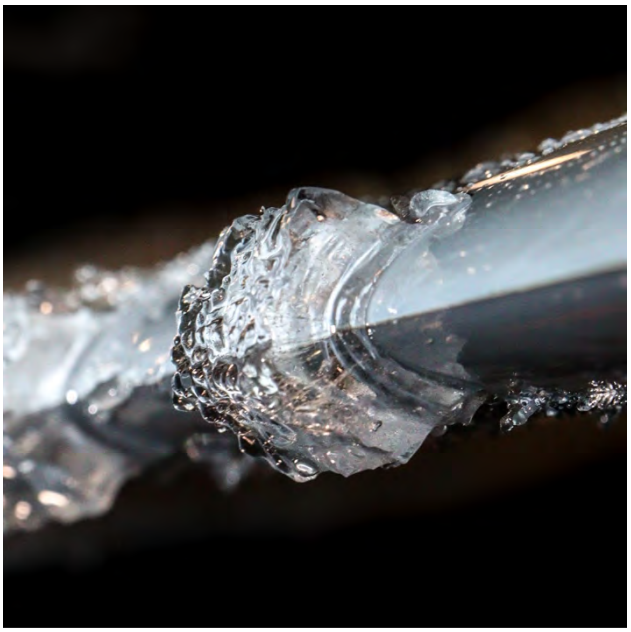

Fig. 1.3.: Glaze ice side-view. Photo from Hann (2020) [24].

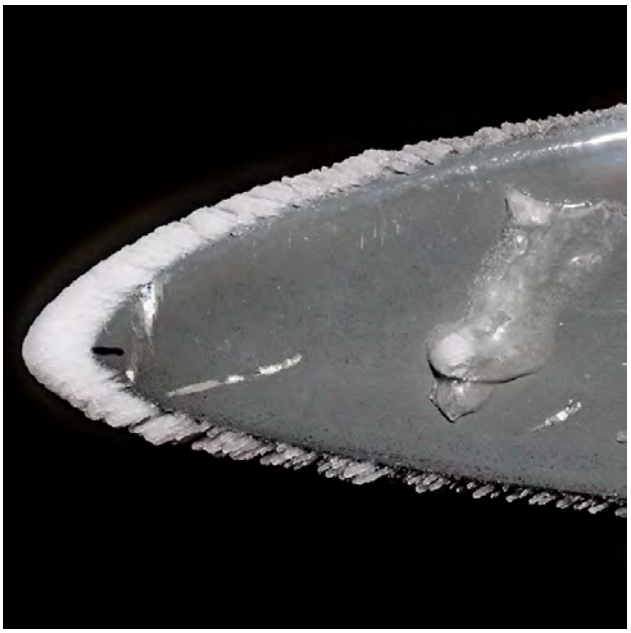

Fig. 1.4.: Profile of rime ice on an airfoil. Photo from Hann (2020) [24].

Fig. 1.5.: Profile of mixed ice on an airfoil. Photo from Hann (2020) [24].

One of the first analytical studies on in-flight icing of UAVs and the influence of the Reynolds number on the ice accretion process was performed by Szilder and McIlwain in 2011 [48]. They derived an analytical analysis allowing the identification of glaze and rime ice formation regimes. Their analysis is based on simplified energy and mass conservation equations as well as the air temperature and the liquid water content. Additionally, two dimensional computational fluid dynamic (CFD) calculations revealed that the aerodynamic penalties from icing could be greater at low Reynolds numbers (Re=5x10^4) compared to high Reynolds numbers (Re=5x10^6) [48].

To contribute more insight to the effect of icing on small UAVs at low Reynolds numbers, Williams et al. [53] conducted ice accretion and aerodynamic performance experiments on a RG-15 airfoil in 2017. They used four different artificial ice shapes for their performance tests, one generated with atmospheric icing conditions typically found in strati-form clouds and three with atmospheric icing conditions typically found in cumuli-form clouds. Williams et al. concluded, that the penalties on the lift coefficient caused by the ice-accretion are almost negligible, whereas the effect on the pitching moment presents itself in a relaxation of the airfoil stability. In contrast to that, the drag levels increased significantly for all tested ice shapes [53]. In the same year Szilder and Yuan [49] published results on numerical ice accretion CFD simulations at low Reynolds numbers. One of their considered UAV airfoil, whose also been aerodynamically analysed, was the HQ309. Szilder an Yuan observed greater aerodynamic penalties from rime ice compared to glaze ice at AoA greater than 9° and identified the surface roughness of the rime ice to be the major contributor to this phenomena [49].

One of the main objectives of Hann [26] was to extend the previously mentioned research of Szilder and McIlwains by independently analysing the effects of chord length and airspeed, because neither Williams et al. nor Szilder and Yuan considered these effects in their performance degradation works on iced UAV airfoils. Hann found out, that the airspeed variation for glaze ice case had a small effect on the resulting aerodynamic penalties. Compared to the clean S826 airfoil, a reduction of -2° was observed for the stall angles. Although the rime ice case induced the least severe aerodynamic penalties with variating the airspeed, the onset of stall occurred up to 3° earlier for the lowest airspeed of $v = 13\frac{m}{s}$ compared to the highest airspeed of $v = 100\frac{m}{s}$ [24]. This was correlated by Hann to the streamwise ice shape. He further identified the mixed ice case as the most severe for the aerodynamic performance degradations since large horn-ice features occurred in the transition phase from rime to glaze ice. Besides these penalties resulting from airspeed variation, changing the chord length showed for all icing cases a severe degradation of the airfoils aerodynamic performance [24].

A worth mentioning key feature of low Reynolds number airfoil flow-fields are the laminar separation bubbles (LSB) [54]. They form when the initial laminar boundary layer is exposed to a large adverse pressure gradient, which causes flow separation. After destabilization of the laminar shear layer further downstream, the flow transitions to a fully turbulent state. The condition for the shear layer to reattach is reached by a high enough momentum transport normal to the airfoil surface and the termination of the reverse near-wall flow by the turbulent mixing [9]. Investigating the LSB occurrence at a Reynolds number of 100,000 on a clean RG-15 airfoil compared to induced LSB-like phenomena by horn and streams-wise ice shapes was the objective of Oo in 2020 [35]. Pressure frequency oscillations within the separation region and a higher standard deviation of the pressure coefficient fluctuations led Oo conclude, that the ice induced LSBs have the same behaviour as normal LSBs: the formation of a shear layer having a transition region before reaching reattachment again [35].

Numerical studies on icing performance penalties of an RG-15 airfoil at low Reynolds numbers of 800,000 were performed by Fajt in 2019 [21]. In his study he took 16 different meteorological conditions into account and performed a severity assessment. The severity assessment was based on a normalized aerodynamic coefficient index comparing the ice induced deteriorations to the clean RG-15 at three different AoA. He concluded, that the most critical atmospheric icing-condition for the RG-15 aerodynamic performance is present at temperatures of -2℃ and a droplet's median volume diameter (MVD) of $20\mu m$ [21].

In summary, the growing commercial drone market is motivated by new arising opportunities for UAV applications. The category of mid-sized fixed-wing UAVs with typically long-endurance and long-range missions profiles requires an all weather capability. This is why the atmospheric in-flight icing has been identified as a key limitation to the operational envelope of this UAV type. The development of UAV ice protection technologies depends on experimentally validated numerical simulation tools, since resent papers showed a strong Reynolds number dependency of the ice accretion process. Consequently, the existing numerical tools for manned aircraft can not directly be applied for the one order of magnitude lower Reynolds number regime of UAV applications. The existing numerical codes and programs covering the in-flight icing topic have been developed for the manned aviation and must firstly be validated for UAV applications. Even though several studies have been conducted numerically on the topic of atmospheric in-flight ice accretion and the resulting aerodynamic penalties, only few have been conducted experimentally on a wide Reynolds number range.

The major goal of this thesis is to provide experimental data on aerodynamic penalties induced by typical ice shapes on a medium-sized fixed-wing UAV airfoil at a wider Reynolds number range from 200,000 to 750,000. Furthermore, this thesis aims to also contribute to the ongoing validation of the manned aviation numerical tools for UAV applications. This is why the conducted experiments with a RG-15 airfoil and artificial three-dimensional (3D) printed glaze, rime, and mixed ice shapes were compared to numerical simulations with the ANSYS FENSAP module. The experimental study was initially set out to test angular sweeps of all three 3D-printed artificial ice shapes, but ultimately only an angular sweep for the glaze ice shape at the Reynolds numbers regimes of 200,000 and 400,000 was performed. Nevertheless, each ice shape was tested at all three Reynolds number regimes at an AoA=-1.3°. The experiments were conducted at the von Karman Institute for Fluid Dynamics (VKI) in Rhode-Saint-Genèse, Belgium and scientifically accompanied by its Environmental and Applied Fluid Dynamics Department, as well as by the Department of Engineering Cybernetics of the Norwegian University of Science and Technology (NTNU) in Trondheim, Norway, and by the Institute of Aerodynamics and Gas Dynamics (IAG) of the University of Stuttgart in Vaihingen, Germany.

After already summarizing the current literature state of the art, this thesis is furthermore structured as follows: In the methodology chapter, the wind tunnel facility L1-B at the VKI and the used testing equipment is described in detail with mentioning their measuring principal, calibration technique, instalment, and uncertainties. Besides the experimental methodology, the numerical simulation set-up is presented after briefly introducing the utilized software. Following on, the next chapter is dedicated to the results of the experimental campaign and the CFD simulations with the ANSYS FENSAP module. A discussion and comparison of the results to literature is content of the fourth chapter. On this occasion, also the problems during the testing campaign are addressed and the error chain and deviations of the experimental data to the CFD simulations are critically evaluated. After providing a summary of the findings, the thesis is closing out with a proposal of future research topics.

2. Methodology

This chapter aims to provide crucial information on the techniques used to conduct this thesis. Firstly, the wind tunnel facility at the VKI is briefly presented. Afterwards, the mounting of the RG-15 airfoil inside the wind tunnel test section is illustrated in detail. Following on with the description of the three artificial ice shapes, the parametric study approach of the conducted experiments is explained. This section is followed by the description of the applied measurement equipment, the uncertainty analysis and the necessary wind tunnel flow corrections. The chapter concludes with a description of the used software and CFD specific modelling details, like the applied boundary conditions and grid parameters.

2.1. Wind tunnel facility L1-B

The wind tunnel facility L1-B has the ability to conduct open and closed test section experiments by laterally exchanging the whole test section (see Figure 2.1). For this thesis the rectangular closed test section configuration is chosen with the geometrical dimensions of 2m height, 3m width, and 20m length. The section contains two test beds, one in the front part with a six component platform balance and one in the rear part with a 2.6m diameter turntable. Since aerodynamic measurements were conducted throughout this thesis, the six component platform balance test bed was used. The tunnel is powered with a 580kW direct current motor driving two contra-rotating fans providing wind speed ranging from $2\frac{m}{s}$ up to $50\frac{m}{s}$ [17]. The motor is shared with a second wind tunnel facility and the maximum achievable wind speed for the testing campaign was $25\frac{m}{s}$. Therefore, the maximum Mach number of 0.07 yields incompressible flow conditions inside the wind tunnel and the Reynolds number was the major similarity parameter. Within the closed test section, the typical turbulence intensity level at $20\frac{m}{s}$ was estimated by previous VKI internal studies to be around 0,8% [52].

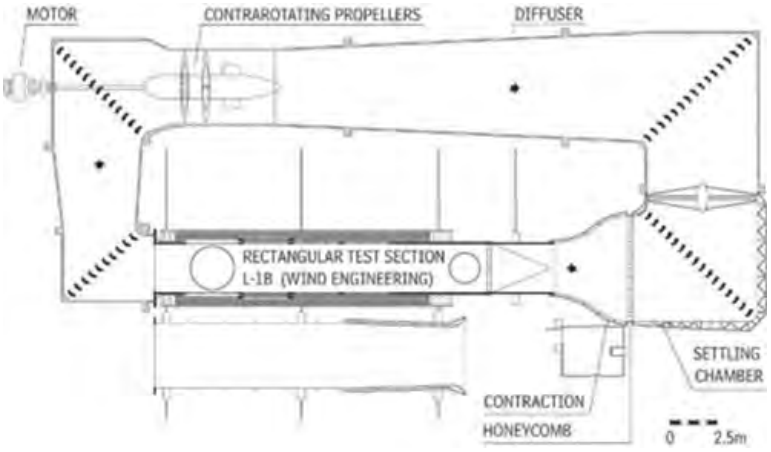

Fig. 2.1.: Top down view of the L1-B testing facility at VKI. From Coudou (2016) [17]

.

2.2. RG-15 Airfoil model

When it comes to research concerning UAV in-flight icing, the most commonly used airfoil type is the RG-15, which was designed for high lift to drag (L/D) ratios at low Reynolds numbers by Rolf Girsberger [46]. It is a standard airfoil for radio controlled model sailplanes flying in the F3B class competitions and has a relative thickness of 8.92% and a chamber of 1.76%. The F3B competition carried out by the World Air Sports Federation FAI consists of three different tasks: duration, distance, and speed [50]. The RG-15's advantage for this competitions lays in its L/D performance, which suits it best for distance and speed tasks. According to Selig et al. [46], the RG-15 is even preferred by sailplane pilots in thermal duration competitions, where windy and strong thermal conditions are given by the geographical regions. In general it is not surprising that this airfoil is also used for small to mid-sized fixed-wing UAVs designed for long range and long endurance missions, whose operational envelope requires an all-weather capability. Therefore, the risk of atmospheric in-flight icing becomes a key limitation for these UAVs and it is of great interest to determine the aerodynamic performance penalties from ice accretion.

Geometric description and manufacturing The coordinate data of the RG-15 was retrieved from [45]. The wing with a span-width of $b = 650$mm, a chord length of $c = 450$mm and a trailing edge height of 2.4mm was manufactured by Smart Solutions KP from Poland. It basically consists of a resin and glass fibre composite with a smooth grey surface finish. As rotation axis served two aluminium rods. The aluminium rods and the wing were joined by friction force similar to a common dowel working principle. To enable pressure measurements along the wing's surface in chord direction, the upper wing side was equipped with 36, the lower with 34 pressure holes. They were distributed inclined by 10° to the chord axis with a constant spacing of 10mm. This design decision was made to prevent the more farther downstream positioned holes from being affected by the flow interactions caused by the pressure holes ahead of them. The pressure tubes were guided out of the wing box alongside of the aluminium rods (see Figure 2.2). For the numerical studies and applied wind tunnel corrections, it was necessary to determine the geometrical deviations of the manufactured wing model from the ideal RG-15 profile. The profile coordinates of the wind tunnel wing model were

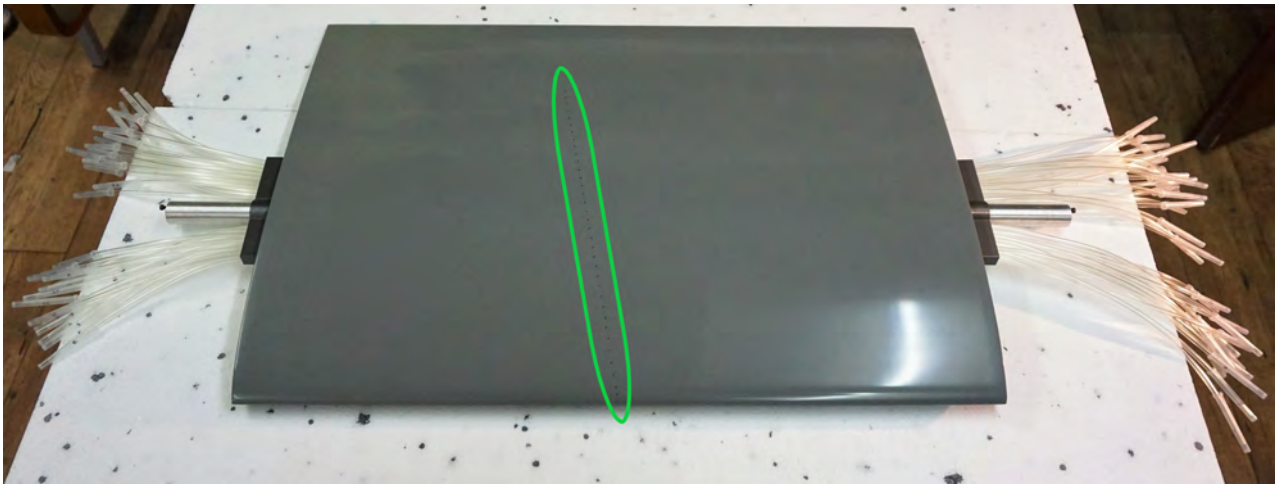

Fig. 2.2.: RG-15 wind tunnel model unmounted. The pressure tubes are coming out of the wing guided by a rectangular 3D-printed plastic insert next to the aluminium rods acting as the wings mounting axes. The green oval indicates the pressure tap location.

determined with the aid of the digital image correlation software ImageJ [27] and a traced contour plot of the wing profile on millimetre paper (see Appendix A.4). The resulting coordinate point distribution was not steady. Consequently, a further called RG-15C profile was generated on the basis of the ideal RG-15 airfoil with the software XFLR5 version 6.48 [55] to digitally resemble the wind tunnel wing model. The applied change to the RG-15 contour was an open/blunt trailing edge with a height of 0,44%/2mm chord, whose blending distance from the trailing edge was 80% chord. In Figure 2.3, the ideal RG-15 airfoil, the normalized RG-15C airfoil and the normalized measured wind tunnel wing model contour are displayed. The RG-15C covers the general proportionality of the measured wing within 2mm deviations in y-direction. An analysis of each airfoils aerodynamic coefficients with the aid of viscous XFOIL simulations revealed no significant deviations between the airfoils. Therefore, the geometric deviations of the RG-15C to the measured wing were assumed to be of secondary order. This is why the RG-15C was used as the reference airfoil within this thesis, since it captured the contour of the wind tunnel wing model to a great extend and had a steady curvature, which was advantageous for the convergence of the numerical calculations. The position and magnitudes of the profiles' chamber and relative thickness are tabulated in Table 2.1.

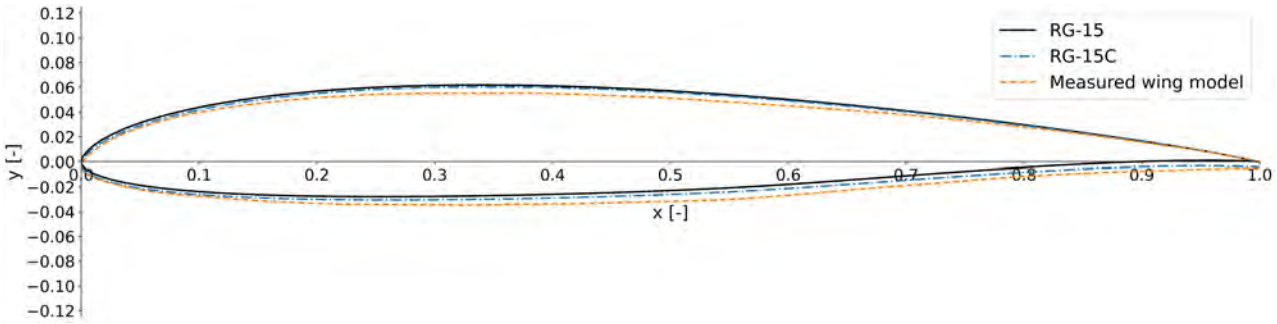

Fig. 2.3.: Comparison of the RG-15 profile (black) to the measured profile contour (orange) of the tested wing in normalized coordinates. The normalized RG-15C (blue) with an open trailing edge of 0.44% chord was achieved based on the RG-15 with a blending distance from the trailing edge of 80% chord.

Tab. 2.1.: Changes of the RG-15 chamber and relative thickness to fit the measured contour of the wind tunnel wing.

Profile	Thickness	Maximum thickness position	Maximum chamber	Maximum chamber position
RG-15	8.93%	31.33%	1.76%	39.74%
RG-15C	9.04%	32.33%	1.54%	39.44%

Wind tunnel mounting The mounting of the wing inside the large L1-B wind tunnel was conducted by the experienced technicians of the VKI. Two Bosch-profiles were rigidly connected to the balance's top plate. The balance cut-out in the wind tunnel floor was then covered by a thick plexiglass plate with defined cut-outs for the Bosch-profiles. The plexiglass had no connection to the balance and shielded the balance from the flow inside the wind tunnel. Furthermore, the plexiglass provided a plane transition between the wind tunnel floor and the balance cut-out. All additional holes from previous test set-ups were covered by duct tape. Afterwards, the wing was placed on top of the Bosch-profiles, which had an axe fixation break system out of brass. The pressure tubes were guided along the Bosch-profiles through the plexiglass and connected to the pressure box underneath the wind tunnel. To achieve a purely two dimensional flow, wooden side panels ranging from bottom to

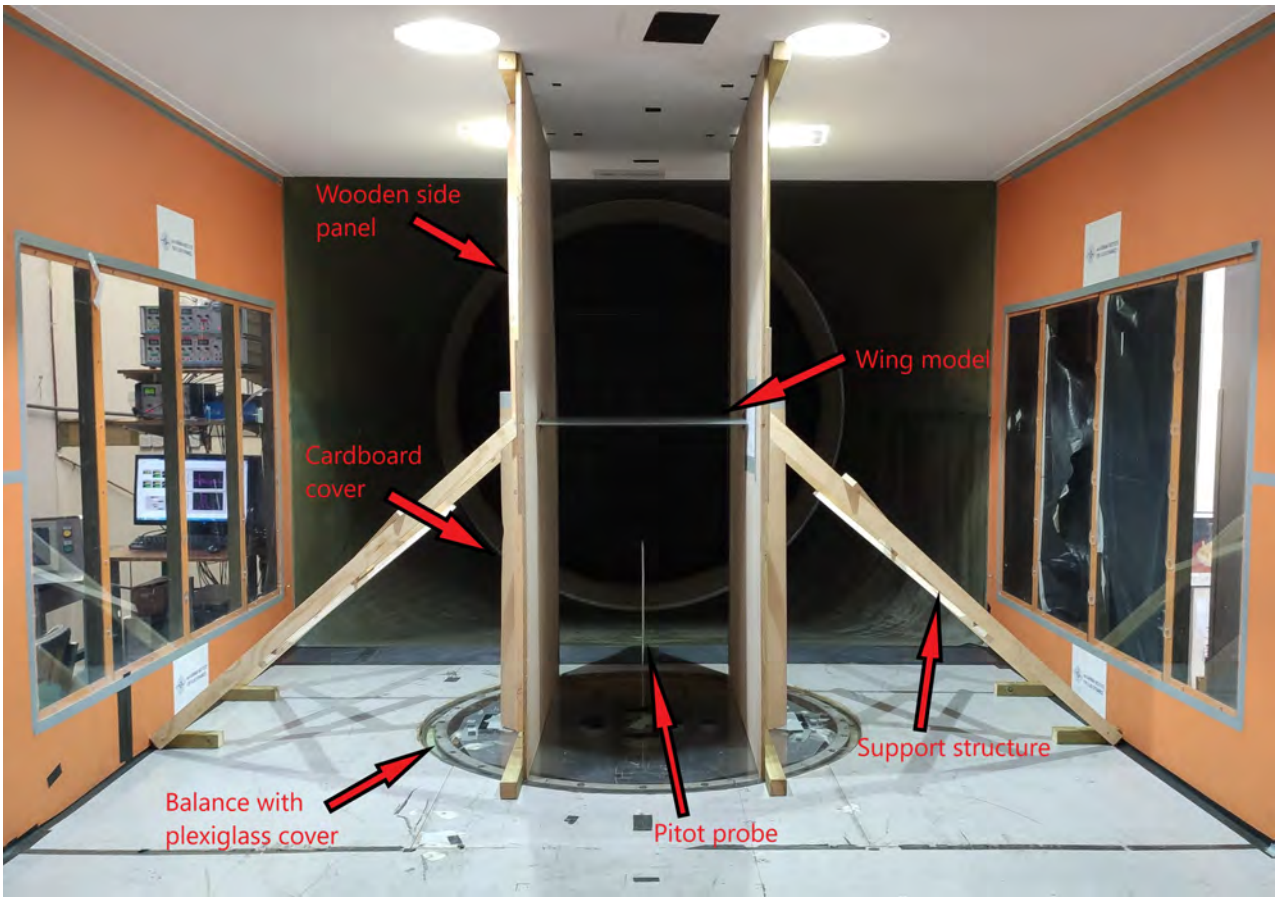

Fig. 2.4.: In-flow view of the installed wing inside the L1-B wind tunnel. The wooden side panels enables a 2D flow measurement inside a the larger test chamber. The wooden side structure is acting as an additional stiffness element to prevent high vibration amplitudes and resonance occurrences.

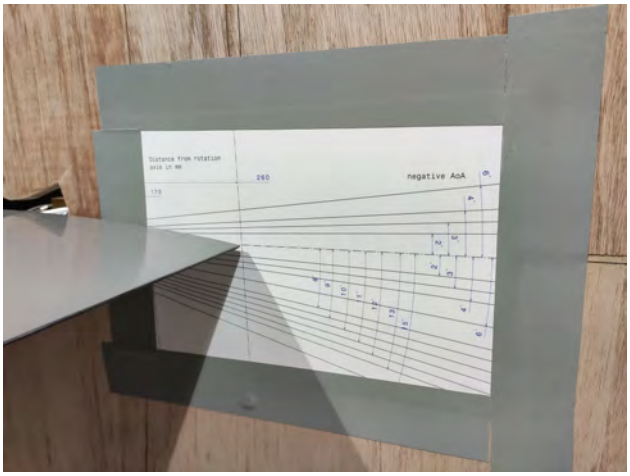

Fig. 2.5.: Alignment paper for the AoA taped to one of the two wooden side panels. The trailing edge of the wing was set to the angle indication lines to adjust the AoA.

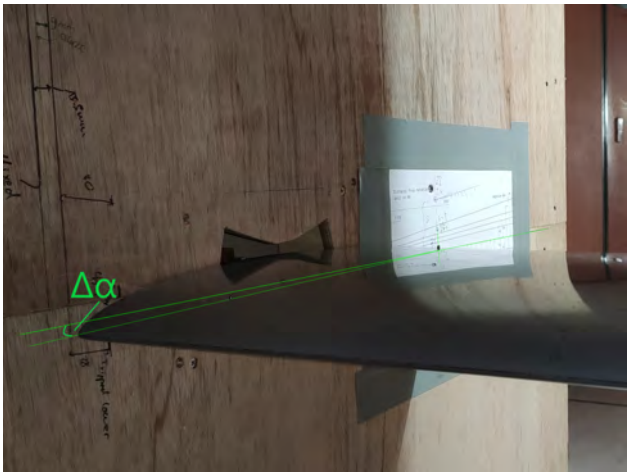

Fig. 2.6.: Visualized -1.25° AoA offset as a result of the off-centred wing rotation axis to the wings' chord line and the placement of the AoA alignment paper.

the top of the tunnel where placed in the space between wing and Bosch-profiles (see Figure 2.4). This reduced the effective wind tunnel cross section from 6m^2 down to 1.32m^2 in between the wooden side panels. The resulting cut-out in the wooden side panels for the wing's axis had to be covered on the inner side by duct tape for each AoA individually to avoid side airflow influences on the balance. To further shield the Bosch-profiles from the airflow, half cylinders out of stiff cardboard were installed around them. The wooden side panels were structurally reinforced by cross beams to the side walls of the wind tunnel to prevent them from being stimulated to resonance by the airflow and minimize their vibration amplitudes at the same time (see Figure 2.4). In addition to that, a small gap of 3mm between the wooden side panels and the wing guaranteed the physical decoupling of both elements. Furthermore, the front edges of the wooden side panels were rounded to reduce instabilities and decrease the boundary layer height. The alignment of the AoA was done by a paper taped to one of the two wooden side panels, which had the respective angles printed on as seen in Figure 2.5. These angles had their centre in the wing's rotation axis and the AoA=0° indication was aligned horizontally at the rotation axis height. It was discovered during the data analysis, that the axe centre line of the aluminium rods was not matching the wing's chord. This caused a constant offset of the real AoA to the one indicated by the paper of -1.25° (see Figure 2.6). In the following, the corrected AoA of the wind tunnel experiments will be mentioned as AoAc.

2.3. Artificial 3D-printed ice shapes

Three different artificial 3D-printed ice shapes were tested during the experimental campaign to gain more insight on the aerodynamic penalties resulting from atmospheric in-flight icing of mid-sized fixed-wing UAVs. The ice topologies were obtained by the NTNU during previous ice accretion experiments on a RG-15 airfoil inside a VTT [28] icing wind tunnel [24]. Details on the utilized liquid water content (LWC), median droplet volume diameter (MVD), accretion temperature T_{acc} and accretion time t_{acc} are provided in Table 2.2. The ice shapes were simplified to a two dimensional cut of the individual accreted ice shape and extruded to the full span-width of the wing. The contours of the utilized ice shapes are displayed in Figure 2.7. With the aid of duct tape, the ice shapes were fixed in place at the leading edge of the wing (see Figure 2.8). The added roughness length by the duct tape was considered to not influence the desired measurements to a great extend, since the original ice shapes had also ice roughness features farther downstream. These ice roughness features were too small in height to cover them by the 2D approximation and the 3D-printing process.

Tab. 2.2.: Icing conditions inside the VTT icing wind tunnel at the NTNU.

condition	AoA [°]	v $\left[\frac{m}{s}\right]$	T_{acc} [℃]	t_{acc} $[min]$	LWC $\left[\frac{g}{m^3}\right]$	MVD $[\mu m]$
Glaze	0	25	-2	20	0.44	26
Mixed	0	25	-5	20	0.44	26
Rime	0	25	-10	20	0.44	26

2.4. Parametric study approach

Since the experiments inside the L1-B were conducted in incompressible flow regimes, the Reynolds number is a major similarity parameter. The maximum achievable Reynolds number with the ambient conditions inside the L1-B and $v_\infty = 25\frac{m}{s}$ was around 750,000 for a chord length of c =450mm. This

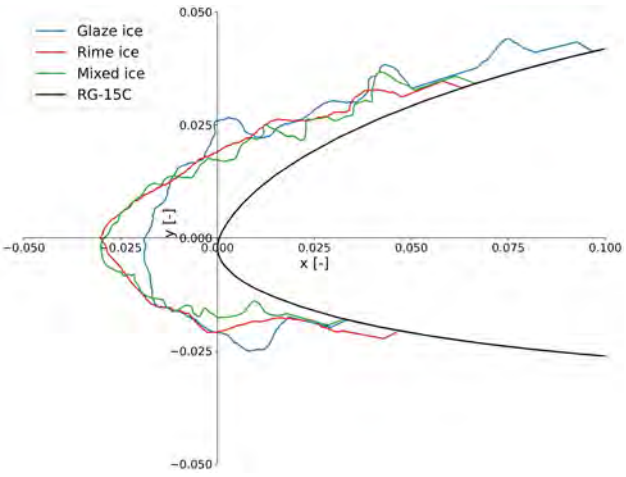

Fig. 2.7.: Contour plot of the utilized artificial glaze (blue), rime (red), and mixed (green) ice shapes.

Fig. 2.8.: Artificial 3D-printed ice shape mounted at the leading edge of the wing with the aid of duct tape and spared out pressure holes in the middle of the wing.

was the highest tested Reynolds number regime, which is similar to present Reynolds numbers at cruise conditions of e.g. the AAI Shadow RQ-7B V2 and Boeing Insitu ScanEagle [25].

The lowest Reynolds number was set to 200,000 to enable the comparison and validation to other conducted RG-15 airfoil wind tunnel tests from literature. The second lower Reynolds number was chosen to be 400,000, which equals half the available maximum wind tunnel speed. Inside the L1-B, these Reynolds numbers equals free stream velocities of $v_\infty = 6.5\frac{m}{s}$ for 200,000 and $v_\infty = 13.1\frac{m}{s}$ for 400,000 respectively. To ensure a stable measurement configuration and no wing movement throughout the acquisition, the velocity sequence per AoA started with an initial full blow of the desired velocity maximum, before acquiring the first zero at $v_\infty = 0\frac{m}{s}$. Afterwards the velocity was stepwise increased to the desired velocities of $6.5\frac{m}{s}$, then $13.1\frac{m}{s}$ and finally $25\frac{m}{s}$ before a second time $25\frac{m}{s}$, $13.1\frac{m}{s}$, $6.5\frac{m}{s}$ and a second zero was acquired. To cover the effect of the measurement equipment hysteresis, the two zero velocity measurements were used to correct the ascending and descending velocity tests.

Due to a limited testing time, the angular resolution was set to 3°, ranging from a AoA=-6° up to 15° (AoAc =-7.8° until 13.2° respectively) with a 1° resolution near the stall region. The highest velocity was only conducted for the clean RG-15 airfoil and the AoA=0° condition of the ice shape tests. Solely the glaze ice shape was tested up to 10° at the two lower Reynolds numbers of 200,000 and 400,000. To have a fully turbulent boundary layer comparison case for the CFD analysis, a tripped airfoil case was tested at AoA=0° and 10°. The tripping of the boundary layer was achieved by applying a zig-zag tape with a height of 0.5mm and an opening angle of 60° across the whole wing span at 10% chord length on the upper airfoil side and at 5% chord length on the lower airfoil side. The resulting conducted test matrix is given in the Appendix A.1 by Table A.1 for the Reynolds number of 750,000 and by Table A.2 for the lower Reynolds numbers of 200,000 and 400,000. Herein, the AoAc as discussed in section 2.2 is also provided.

2.5. Measurement equipment

This section introduces the used measurement equipment to conduct the experiments inside the L1-B. The forces and moments were measured with the aid of a six component platform balance, installed in the frontal test bed of the L1-B (Figure 2.9). Furthermore, the airfoil was equipped with 46 pressure tabs connected to a pressure box with 48 digital pressure sensors underneath the wind tunnel. The two spare pressure channels of the box were used for measuring the total pressure and the differential connected dynamic pressure of the Pitot-static probe ahead of the wing.

2.5.1. Six component balance

The platform balance was initially developed for surface vehicle measurements, but the later upgrade of the strain gauges sensors provides sufficient precision for aviation measurements. Figures A.4 and A.5 in the Appendix A.5 are displaying the internal layout of the balance. It consists out of two parallel plates of which the lower one is attached via flexure suspensions to a steel frame providing a rigid connection to the wind tunnel. The balance's lateral motion is prevented by the three force measuring cells responsible for the drag force, side force, and yawing moment determination. Via four vertical force measuring cells, the upper plate is joined with the lower plate. The fourth sensor is redundant, providing information regarding ill posed conditions of the lift distribution over the four sensors. Therefore, to eliminate this uncertainty, the four load measuring cells are interconnected and the combined signals are recorded by the data acquisition system [52]. To retrieve the single lift force, pitch and roll moment out of the combined signals, the load combinations are given in Equations 2.5.1, 2.5.2, and 2.5.3. The amplification gain of the data acquisition system was set to 2000 times the raw signal and the low pass filter was configured to a 200Hz cut-off frequency, since no higher frequencies were expected for the measurements. The sampling frequency was set to 2000Hz, which results in 90,000 samples throughout the acquisition time of 45s.

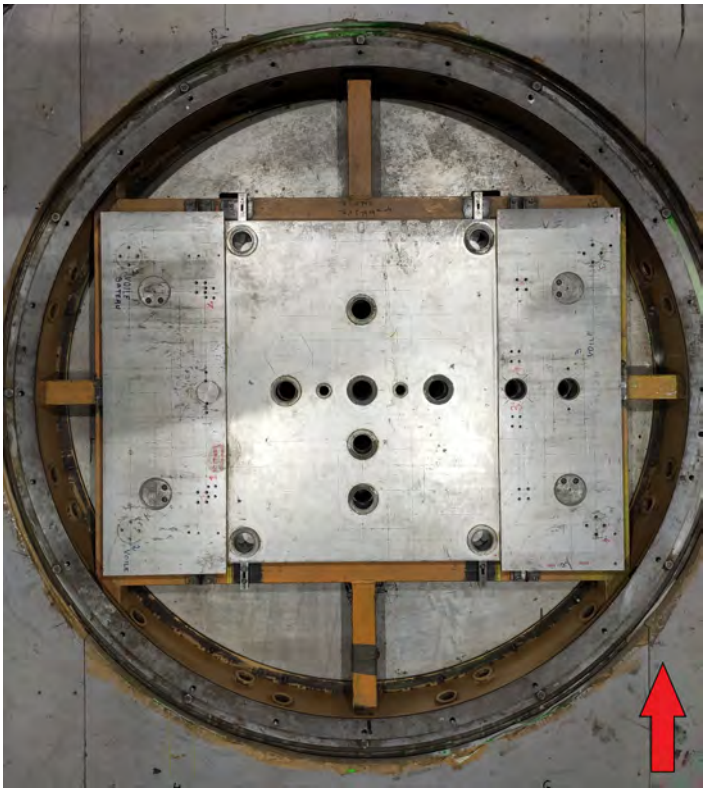

Fig. 2.9.: Top-down view of the platform balance inside the L1-B without cover plates, the red arrow indicates the flow direction.

$$L = F_{Lift,front} + F_{Lift,rear} \tag{2.5.1}$$

$$M_{Roll} = F_{Lift,rear} - F_{Lift,front} \tag{2.5.2}$$

$$M_{Pitch} = 2F_{Lift,right} - F_{Lift,front} - F_{Lift,rear} \tag{2.5.3}$$

Calibration One major problem of this type of balance is its resolving centre not being in the resolving centre of the wing. For its original purpose of naval and automotive experiments, this offset is relatively small and therefore has not been a large issue [52]. To compensate the issue of the resolving centre, special care must be taken when calibrating the balance. In this case, the reference point was set as close to the airfoil mounting axis as possible with the aid of a 1m high calibration head. A cube shaped rigid calibration rig was mounted around the balance, which was mainly constructed with Bosch profiles and thus allowing a simplified alignment of the pulleys for imposing the loads to the calibration head and the balance underneath (see Figure 2.10). The mentioned calibration rig has a support structure out of Bosch profiles to rigidly join it to the balance upper plate right above the balance's geometrical centre. The head itself is a precise machined aluminium block with cube shaped extensions at its edges and a diagonal of 0.4m. The extensions have cut-out features to allow a self centring of the hooked load cables, which were connected via the pulleys to the weights for imposing the forces onto the head. With the aid of a laser, the hooked cables perpendicularity or parallelism to the plane of the calibration head was carefully aligned. To ensure, that pure moments were imposed to the calibration head, two counter-orientated forces were applied to the moment respective opposing cube shaped extensions. Time restrictions inside the wind tunnel

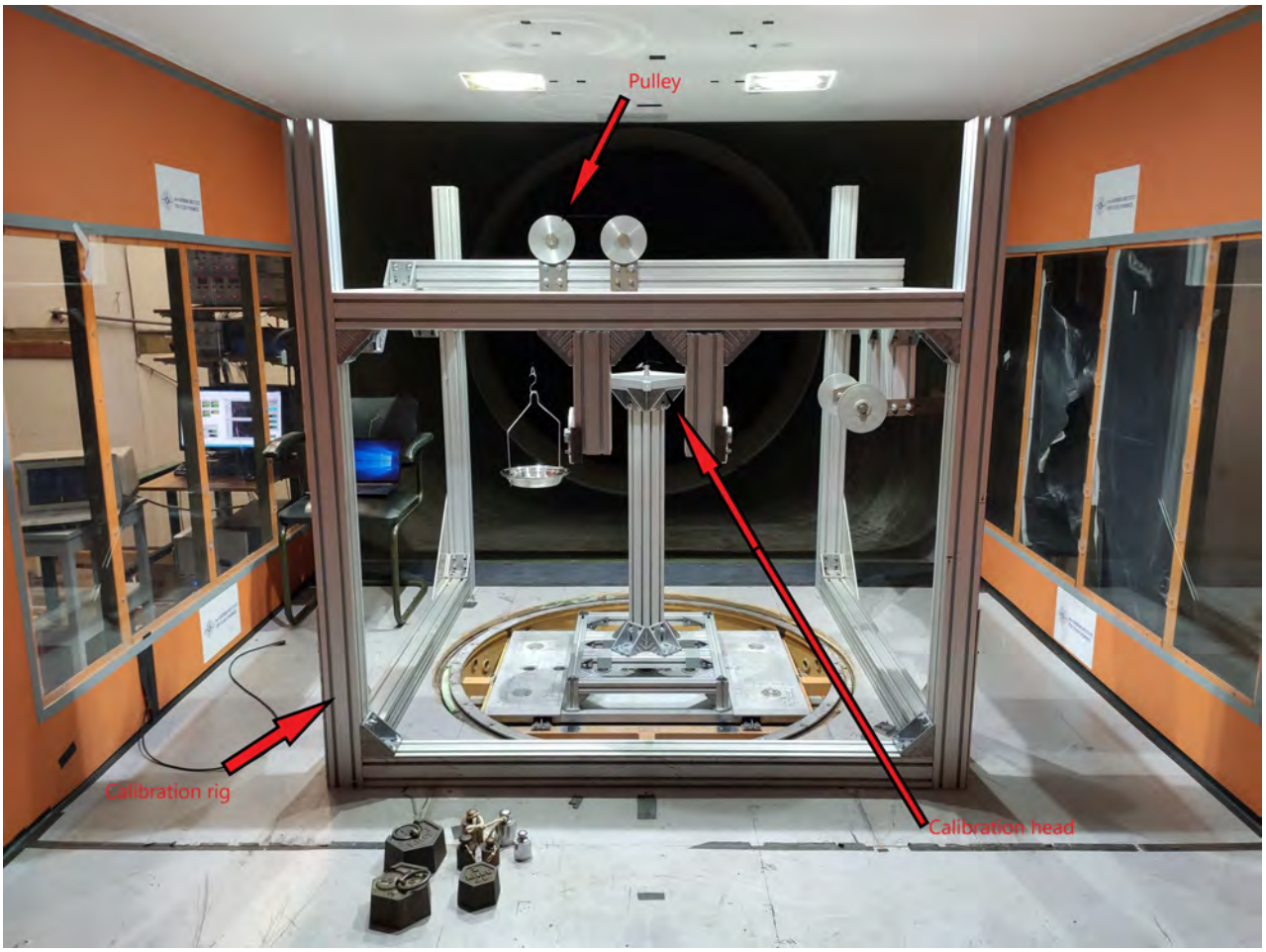

Fig. 2.10.: In flow direction view of the calibration rig mounted around the calibration head. The current setup represents the positive lift force imposing configuration with one pulley orientated with its edge directly above the centre of the calibration head, ensuring the hooked cable to be normal to the head's virtual plane.

due to the availability of technicians made it necessary, to first run the test campaign and calibrate the throughout powered balance afterwards. The chosen load ranges shown in Table 2.3 are based on pre-calculations of the to be expected forces and moments with the software tool XFOIL. To retrieve the load measuring cells' voltage corresponding forces and moments, the computation of a six times six matrix **A** was part of the balance calibration process (see Equation 2.5.7). The vis versa operations: voltages to loads and loads to voltages, are given by the following equations:

$$\vec{U}_{cells} = \mathbf{A} \cdot \vec{F}_{loads} \tag{2.5.4}$$

$$\vec{F}_{loads} = \mathbf{A}^{-1} \cdot \vec{U}_{cells} \tag{2.5.5}$$

with:

$$\vec{U}_{cells} = \begin{bmatrix} U_{Lift,(V)} \\ U_{Roll,(V)} \\ U_{Pitch,(V)} \\ U_{Yaw,(V)} \\ U_{Drag,(V)} \\ U_{Side,(V)} \end{bmatrix} \qquad \vec{F}_{loads} = \begin{bmatrix} F_{Lift,(N)} \\ F_{Roll,(Nm)} \\ F_{Pitch,(Nm)} \\ F_{Yaw,(Nm)} \\ F_{Drag,(N)} \\ F_{Side,(N)} \end{bmatrix} \tag{2.5.6}$$

Where $\vec{U}_{cells}$ is the voltage readout of the balances' data acquisition system in vectorial form and $\vec{F}_{loads}$ contains the respective forces and moments also in a vectorial form. The order of the vectors' elements is with respect to their units of [V] for the voltage vector and [N] or [Nm] for the load vector as displayed: lift force, rolling, pitching, and yawing moment, as well as drag and side force.

$$\mathbf{A} = \begin{bmatrix} -0.045681 & 0.002307 & -0.007291 & 0.000806 & -0.007727 & 0.002415 \\ -0.000934 & 0.110611 & 0.00278 & -0.000108 & 0.003132 & 0.117927 \\ 0.002098 & 0.002318 & 0.212071 & -0.004262 & 0.225399 & 0.005165 \\ -0.000710 & -0.000784 & 0.000682 & 0.147199 & 0.003699 & -0.000071 \\ -0.000893 & -0.002253 & 0.000788 & -0.000228 & -0.000625 & 0.064986 \\ 0.000133 & 0.001961 & -0.001661 & -0.003604 & -0.054833 & 0.002834 \end{bmatrix} \tag{2.5.7}$$

The calibration matrix **A** consists of first order fits generated from the full range voltage responses of each load measuring cell, when applying e.g. pure lift forces to the calibration head. This is possible, because during the design process of the balance, special care was taken to ensure good linearity of the load measuring cells over their full range. Nevertheless, a slight hysteresis effect was observable after reaching the applied load maximum and returning back to zero. For the drag voltages, non-linearity was observed for its imposed loads in the wing's negative drag direction. Therefore, the decision was made to only take the positive drag direction loads into account to derive the slope for the pure drag imposed load matrix coefficients. The resulting effect was a reduction of the absolute drag error to the applied calibration loads $F_{applied}$ by 50%. In terms of absolute errors, Barlow et al. [8] states for external balance calibrations, with the goal to measures aerodynamic loads, a permissible error of less than 0.1% of the applied calibration load. This was only achieved to some extend for the computed lift forces. The other load components exceeded this limit by one order of magnitude (see Figure 2.11). With the data from the calibration, it was possible to estimate the relative precision $\triangle\eta_i$ of the balance's force and moment measurements $F_{computed}$ as the standard deviation of the absolute values of the absolute error divided by the mean of the absolute values of the absolute error $\bar{x}$ (see Equation 2.5.9). Furthermore, the balance's accuracy $\triangle\varsigma_i$ is estimated by the mean of the absolute values of the relative error of each calibration given in percent (see Equation 2.5.10). Both

values are tabulated for each load component in Table 2.3.

$$\bar{x} = \frac{\sum_{n=1}^{n} |F_{computed,n} - F_{applied,n}|}{n} \qquad n = \text{number of calibration run 1, 2, 3, ... , n} \tag{2.5.8}$$

$$\Delta\eta_i = \frac{\sqrt{\frac{\sum_{n=1}^{n}(|F_{computed,n} - F_{applied,n}| - \bar{x})^2}{n}}}{\bar{x}} \tag{2.5.9}$$

$$\Delta\varsigma_i = \frac{\sum_{n=1}^{n} \frac{|F_{computed,n} - F_{applied,n}|}{|F_{applied,n}|}}{n} \tag{2.5.10}$$

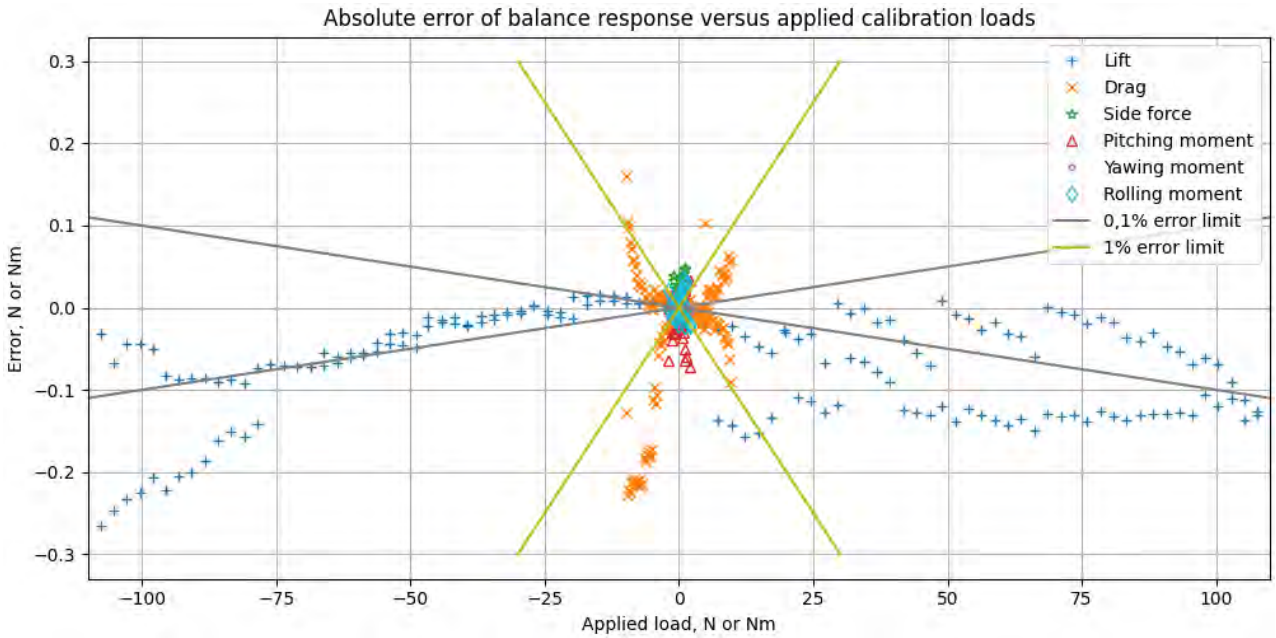

Fig. 2.11.: Permissible error analysis of platform balances' calibration matrix. Displayed is the absolute error of the balances' response to the applied loads during its calibration versus the applied calibration loads. The grey line indicates the permissible limit of 0.1%, whereas the olive one indicates the limit of 1%.

Tab. 2.3.: Imposed ranges, precision and accuracy of the balance calibration for each force and moment component.

Channel	Imposed range	Precision $\Delta\eta$	Accuracy $\Delta\varsigma$
Lift force	±107.75 N	0.88%	0.16%
Drag force	±9.55 N	1.37%	0.89%
Side force	±1.08 N	0.85%	3.23%
Roll moment	±1.96 Nm	0.07%	4.09%
Pitch moment	±1.96 Nm	0.76%	4.13%
Yaw moment	±1.96 Nm	0.61%	1.12%

2.5.2. Pressure acquisition

All the pressure measurements were conducted with sensors of the AMS5812 series. They are manufactured by Analog Microelectronics and have the ability to be assembled on printed circuit boards. Once assembled, they are fully operational, since their electrical power supply is provided by their dual in-line package solder pins and their two vertical metal tubes serves as the pressure connection ports (see Figure 2.12). The pressures are measured via a piezo-resistive silicon measuring cell, which converts the pressures into an almost pressure proportional differential voltage signal. This signal is then fully digital corrected and conditioned by a complementary metal-oxide-semiconductor (CMOS) application-specific integrated circuit (ASIC) placed on a ceramic substrate [3]. A total number of 48 sensors were integrated inside a custom pressure box, every eight assembled on one of the six printed circuit boards (see Figure 2.13). This allowed to connect 23 out of the available 36 wing pressure tubes per wing side with 46 pressure sensors. The first five pressure holes of each wing side were left out, because they would be covered during the artificial 3D-printed ice shape tests by the ice shapes. Also, the distribution of the connected pressure holes farther downstream was less dense due to less expected pressure gradients in that region. The sampling frequency was set to 200Hz, which yields a total number of 9000 samples per 45s of each test's acquisition time.

The wind speeds inside the wind tunnel were determined by a Pitot-static probe placed ahead of the wing installation structure. The L-shaped probe consists out of two tubes, of which one is building the shorter L-beam and pointing directly into the flow. The other one is ending in a hole father downstream of the shorter L-beam, which is aligned perpendicular to the flow. The arising stagnation point at the tip of the probe enables the measurement of the airflow's total pressure, while the perpendicular hole provides the measurement of the airflow's static pressure. To directly measure the airflow's dynamic pressure, the two tubes of the Pitot-static probe are connected to the two ports of a single directional pressure sensor. Therefore, the measured pressure difference of the static and total pressure equals the airflow's dynamic pressure. According to Bernoulli's incompressible flow Equation 2.6.7, this yields with a known density the airflow's free stream velocity.

Calibration The pressure sensors with ranges lower than 4000Pa were calibrated with the aid of a water manometer by carefully imposing pressures with syringes to the water manometer and the pressure sensor at the same time. The resulting plot of the pressure sensor readout against the water manometer column height was used to derive a linear fitting curve as the calibration factor for the sensor (see Appendix A.2). Hence the water column height was limited to 500mm, the higher pressure range sensors were calibrated by a DPI 610 pneumatic calibrator pump (see Figure 2.14). Following the same principle as with the water manometer, the simultaneously imposed pressures to the sensor and the calibrator pump were plotted against each other to derive a linear fitting curve as the sensor's calibration factor (see Figure A.1 in the Appendix A.2). The sensor types and ranges used for this thesis, as well as their individual manufacturing accuracy $\Delta\xi_{AMS5812}$ and induced error by the calibration devices $\Delta\xi_{calibration}$, are given in Table 2.4.

2.6. Uncertainty analysis and applied corrections

The error of a measurement can be expressed by two types of error source terms, the bias or systematic error ξ_{bias} and the random error ξ_{random}. The bias error covers all errors related to the measurement equipment, e.g. the accuracies of the utilized sensors or the calibration device, whereas the random error is related to the distribution of the measured data points. The total error $\Delta\xi$ of the measurement

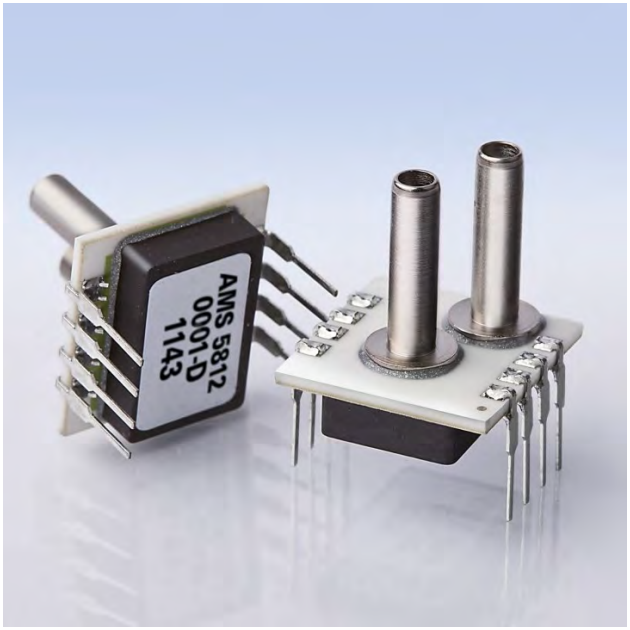

Fig. 2.12.: Close up of the ams5812 pressure sensor series, Picture: 2020 AMSYS GmbH & Co. KG, amsys.de, accessed: 2021-02-25.

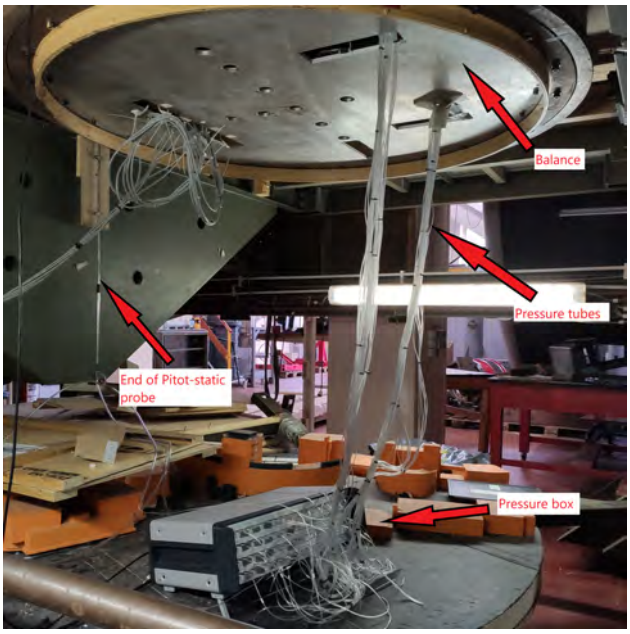

Fig. 2.13.: Custom 48-channel pressure box underneath the wind tunnel test section.

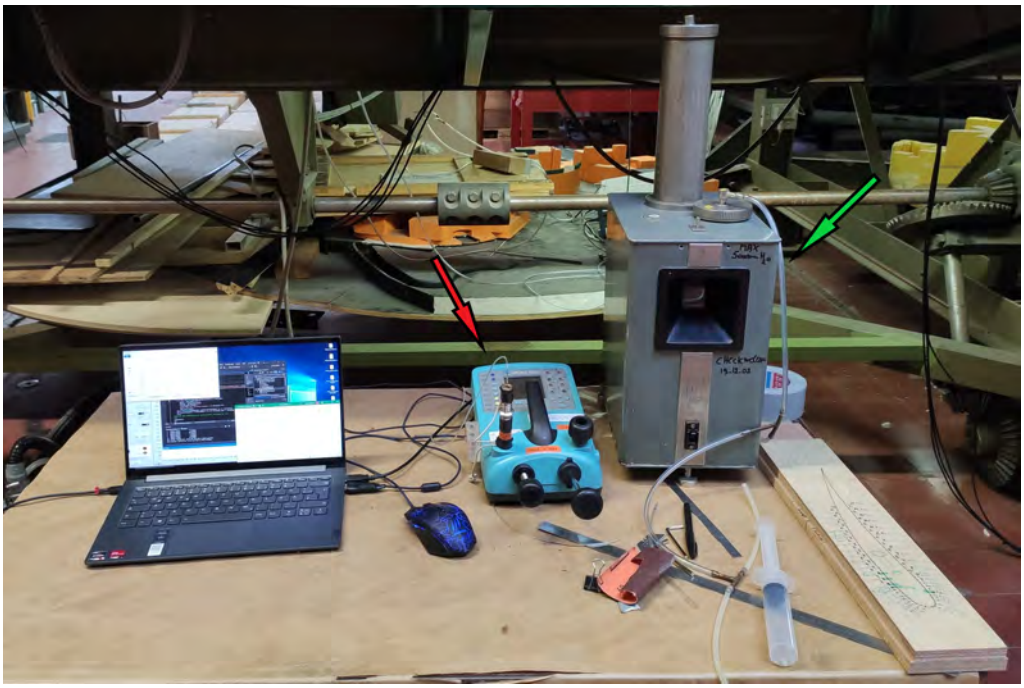

Fig. 2.14.: Pressure calibration setup with the water manometer (green arrow) and the DPI 610 pneumatic calibrator pump (red arrow).

Tab. 2.4.: Calculated accuracies of the utilized ams5812 pressure sensors and their calibration device. The sensors below a range of 4000 Pa were calibrated with a water manometer. For ranges greater 4000 Pa, a DPI 610 pneumatic calibrator pump was used for calibration, which has an accuracy of 0.025% of their different pressure sensor ranges.

Regime	Type	Range [Pa]	$\Delta\xi_{AMS5812}$ [Pa]	$\Delta\xi_{calibration}$ [Pa]
Ultra low	0000-D	0...517	±3.88	±0.98
pressures	0000-D-B	±517	±7.76	±0.98
	0001-D-B	±1,034	±15.51	±0.98
Low	0003-D	0...2,068	±10.34	±0.98
pressures	0015-D	0...10,342	±51.71	±5.00
	0008-D-B	±5,516	±55.16	±3.50
Standard	0030-D	0...20,684	±51.71	±8.75
pressures	0050-D	0...34,474	±86.18	±8.75
	0150-A	0...103,421	±452.46	±3.50
	0300-A	0...206,843	±904.93	±87.50

chain is then depicted by summing up the bias and random errors according to the Pythagoras' law:

$$\Delta\xi = \sqrt{\xi_{bias}^2 + \xi_{random}^2} \tag{2.6.1}$$

If a Gaussian distribution of the measurements is assumed, the random error of the measured variable mean value can be written as the fraction of the measurements standard deviation σ over the square root of the total number of measured samples N, multiplied by 1.96 to imply a 95% confidence interval:

$$\xi_{random} = \pm 1.96 \frac{\sigma}{\sqrt{N}} \tag{2.6.2}$$

The uncertainty of a function, which consists out of multiple measured variables, is determined by extending the Pythagoras' law to cover each variables error contribution. These are calculated as the squared derivatives with respect to the single variable multiplied by the squared total error or uncertainty of the same variable. Building the square root out of the summed up products defines the uncertainty of the initial function [33].

2.6.1. Total errors of the measurement variables

Total error of the pressures The bias errors of the pressure measurements are given by the error related to the utilized calibration device $\Delta\xi_{calibration}$ for each pressure sensor and the error of the sensor $\Delta\xi_{AMS5812}$ itself, provided by the data sheet of the manufacturer (see Appendix A.3). These values are tabulated for each pressure sensor type in Table 2.4. According to Equation 2.6.2, the pressure measurements' random error is calculated by the standard deviation of the sensor's pressure measurement σ_{p_i} divided by the square root of the measurements' total sample number $N_p = 9,000$. This yields for the total error of the pressure measurements:

$$\Delta p_i = \pm \sqrt{\left(1.96 \frac{\sigma_{p_i}}{\sqrt{N_p}}\right)^2 + \left(\Delta\xi_{calibration}\right)^2 + \left(\Delta\xi_{ams5812}\right)^2} \tag{2.6.3}$$

Total error of the force and moment measurements Similar to the random error of the pressure sensors, the one of the force and moment measurements is determined by their standard deviation divided by the balance acquisition's total sample number $N_b = 90,000$. The bias errors are given by the balance's relative calibration accuracies $\Delta\varsigma$ multiplied with the mean value of the respective force or moment measurement. In Equation 2.6.4 the total error of the lift force measurement ΔL is displayed exemplary, where $\bar{L}$ is the mean value of the lift force measurement, σ_L its standard deviation, and $\Delta\varsigma_L$ the balance's lift force calibration accuracy, as tabulated in Table 2.3.

$$\Delta L = \pm 1.96 \sqrt{\left(\frac{\sigma_L}{\sqrt{N_b}}\right)^2 + \left(\Delta\varsigma_L \bar{L}\right)^2} \tag{2.6.4}$$

2.6.2. Uncertainty of the density

With respect to the perfect gas law, the density can be calculated as the fraction of the ambient pressure p_{amb} and the specific gas constant for dry air $R = 287.053763 \frac{J}{kgK}$ multiplied with the ambient temperature T_{amb}:

$$\rho = \frac{p_{amb}}{RT_{amb}} \tag{2.6.5}$$

Assuming an uncertainty of the ambient pressure measurement at the VKI of $\delta p_{amb} = 10Pa$ and an ambient temperature uncertainty inside the wind tunnel facility of $\delta T_{amb} = 1K$, the uncertainty of the density calculation can be written as:

$$\delta\rho = \sqrt{\left(\frac{1}{RT_{amb}}\right)^2 (\delta p_{amb})^2 + \left(-\frac{p_{amb}}{RT_{amb}^2}\right)^2 (\delta T_{amb})^2} \tag{2.6.6}$$

The uncertainty values of the density per testing day are noted in Table 2.5.

Tab. 2.5.: Calculated density uncertainties for each testing day with the atmospheric pressures from the VKI and an averaged ambient temperature of 20℃.

Date	$\delta\rho \left[\frac{kg}{m^3}\right]$	p_{amb} [Pa]	T_{amb} [K]
08.12.2020	0.004008	98881.6	293.15
09.12.2020	0.004038	99446.9	293.15
11.12.2020	0.003968	97728.5	293.15
14.12.2020	0.004025	99132.8	293.15

2.6.3. Uncertainty of the local pressure coefficient

The local pressure coefficient c_p is defined as the subtraction of the free stream static pressure p_s from the local static pressure p at the airfoil surface divided by the dynamic pressure q (see Equation 2.6.8). In incompressible flow regimes, a local pressure coefficient of $c_p = 0$ corresponds to an equality of the local and the free stream static pressure, while a local pressure coefficient of $c_p = 1$ can indicate a stagnation point. With the aid of Bernoulli's incompressible flow Equation 2.6.7, where $g = 9.8066 \frac{m}{s^2}$ is the acceleration due to gravity and h the elevation of the considered fluid element, the dynamic pressure can also be expressed as the total pressure p_0 minus the free stream static pressure or the multiplication of the halved flow density ρ with the squared free stream velocity v_∞. To compensate

the pressure difference between the ambient pressure at the VKI as the sensors' counter pressure and the actual static pressure inside the wind tunnel, the static pressure of the Pitot-static probe needs to be added to each measured airfoil pressure. In Equation 2.6.8, this static pressure is again subtracted from the measured airfoil pressures, which naturally yields the direct use of the original measured airfoil pressures p_i instead. This is especially useful for the uncertainty calculation of the pressure coefficient, since the influence of the static pressure term is then negligible.

$$\frac{v_\infty^2}{2} + gh + \frac{p}{\rho} = constant \tag{2.6.7}$$

$$c_p = \frac{p - p_s}{q} = \frac{p - p_s}{p_0 - p_s} = \frac{p - p_s}{\frac{1}{2}\rho v_\infty} = \frac{p_i}{q} \tag{2.6.8}$$

Furthermore, the pressure coefficient is also calculated with the directly measured dynamic pressure. This is possible, because the used directional sensors ports are connected to the p_s and p_0 of the Pitot-static probe, which allows also the utilization of an AMS5812 ultra low pressure sensor with an high accuracy of $\Delta\xi_{ams5812} = \pm 3.88\text{Pa}$. The uncertainty of the coefficient is determined as follows:

$$\delta c_p = \sqrt{\left(-\frac{p_i}{q^2}\right)^2 (\delta q) + \left(\frac{1}{q}\right)^2 (\Delta p_i)^2} \tag{2.6.9}$$

Where $\Delta p_{dynamic} = \delta q$ is the total error of the dynamic pressure measurement, and Δp_i is the total error of the respective airfoil pressure measurement, both calculated according to Equation 2.6.3.

2.6.4. Uncertainty of the velocity

As mentioned before, the free stream velocity v_∞ can be derived from the dynamic pressure measurement according to Equation 2.6.10. Its uncertainty δv_∞ is given by Equation 2.6.11.

$$v_\infty = \sqrt{\frac{2q}{\rho}} \tag{2.6.10}$$

$$\delta v_\infty = \sqrt{\left(\frac{1}{2}\sqrt{\frac{2}{\rho q}}\right)^2 (\delta q)^2 + \left(-\frac{1}{2}\frac{\sqrt{2q}}{\sqrt[3]{\rho}}\right)^2 (\delta \rho)^2} \tag{2.6.11}$$

2.6.5. Uncertainty of the lift and drag coefficient

The lift coefficient c_l is defined as the lift force L divided by the dynamic pressure times a reference area S. For a rectangular wing section, S is defined as the product of the wing's chord c and its span-width b. The drag coefficient c_d is equally calculated with the drag force instead of the lift force in the counter (see Equation 2.6.12 and 2.6.13)

$$c_l = \frac{L}{\frac{1}{2}\rho v_\infty^2 S} = \frac{L}{qS} \tag{2.6.12}$$

$$c_d = \frac{D}{\frac{1}{2}\rho v_\infty^2 S} = \frac{D}{qS} \tag{2.6.13}$$

$$L/D = \frac{c_l}{c_d} \tag{2.6.14}$$

Following on, the uncertainty of the lift and drag coefficient consists of multiple terms, taking the influences of the balance's force measurement ΔL and ΔD (see Equation 2.6.4), the dynamic pressure measurement $\Delta p_{dynamic} = \delta q$ (see Equation 2.6.3) and the geometric uncertainty of the wings reference area δS into account. The wing is determined to be manufactured to a 2mm precision of its chord and span-width lengths, which yields for $\delta S = 0.000004m^2$. Therefore, the uncertainties δc_l and δc_d of the lift and drag coefficient are calculated as follows:

$$\delta c_l = \sqrt{\left(\frac{1}{qS}\right)(\Delta L)^2 + \left(-\frac{L}{q^2 S}\right)^2 (\delta q)^2 + \left(-\frac{L}{qS^2}\right)^2 (\delta S)^2} \tag{2.6.15}$$

$$\delta c_d = \sqrt{\left(\frac{1}{qS}\right)(\Delta D)^2 + \left(-\frac{D}{q^2 S}\right)^2 (\delta q)^2 + \left(-\frac{D}{qS^2}\right)^2 (\delta S)^2} \tag{2.6.16}$$

As the L/D ratio is calculated according to Equation 2.6.14, the uncertainty of the L/D ratio $\delta L/D$ is consequently:

$$\delta L/D = \sqrt{\left(\frac{1}{c_d}\right)(\delta c_l)^2 + \left(-\frac{c_l}{{c_d}^2}\right)^2 (\delta c_d)^2} \tag{2.6.17}$$

2.6.6. Uncertainty of the moment coefficient

The difference of the moment coefficient c_m in comparison to the drag or lift coefficient is its additional chord multiplication in the denominator to gain again non-dimensionality:

$$c_m = \frac{M}{\frac{1}{2}\rho v_\infty^2 Sc} = \frac{M}{qSc} \tag{2.6.18}$$

Therefore, a term must be added in the moment coefficient uncertainty δc_m to cover the influence of the chord length manufacturing error $\delta c = 0.002m$ (see Equation 2.6.19). Herein, the balance's pitching moment measurement error ΔM is derived according to Equation 2.6.4.

$$\delta c_m = \sqrt{\left(\frac{1}{qSc}\right)(\Delta M)^2 + \left(-\frac{M}{q^2 Sc}\right)^2 (\delta q)^2 + \left(-\frac{M}{qS^2 c}\right)^2 (\delta S)^2 + \left(-\frac{M}{qSc^2}\right)^2 (\delta c)^2} \tag{2.6.19}$$

2.6.7. Pitching moment corrections

Due to the fact, that the wing model's rotation axis is not aligned with the quarter point of its chord, the measured pitching moment ${M_{pitch}}'$ must be corrected. In general, this correction is conducted by transforming vectorial the moments' resolve centre resulting from the balance calibration to the aerodynamic centre of the wing. Because in this case, the calibration resolve centre is the same as the wing's rotation axis centre, this transformation simplifies to

$$M_{pitch_{\frac{1}{4}}} = {M_{pitch}}' + L' l \sin(\alpha) + D' l \cos(\alpha) \tag{2.6.20}$$

where l is the distance between the axis centre and the wing's quarter point, α is the AoAc, L' and D' are the measured lift and drag forces and $M_{pitch_{\frac{1}{4}}}$ is the corrected pitching moment. The distance was measured to $l = 0.0782m$.

2.6.8. 2D wind tunnel wall flow interference compensations

As stated in section 2.2 , the investigated and horizontally placed wing was a constant section of the RG-15 airfoil. The wooden side panels ranged from the floor to the ceiling of the L1-B test section, which formed a smaller 2D-flow wind tunnel section inside the bigger L1-B section. Therefore, the wing was spanning the whole tunnel from wooden side wall to wooden side wall leading to aerodynamic effects, which are considerably influencing the measurements according to Barlow et al. [8]. In a closed test section the airflow's natural free air curvature is restrained by its floor and ceiling, thus confining the flow around the wing and leading to a velocity increase by continuity and Bernoulli's equation [8]. This effect is called solid blockage and results in the wing model to act like an additional cambered one [2]. For an airfoil with a finite thickness and camber, Allen and Vincenti [2] derived theoretical tunnel-wall corrections to compensate the effects of the compressibility of the fluid and the wake of the airfoil. These corrections are valid for small chord c to tunnel height h ratios, which is the case for the conducted experiments $\frac{c}{h} = \frac{0.45m}{2m} = 0.225$. To derive the tunnel walls influence upon the flow-field at the airfoil, Allen and Vincenti introduced two airfoil geometry driven factors σ and Λ. They act as an increase of the incompressible airflow's axial velocity at the base profile, which is induced by the tunnel walls. σ takes the airfoil's relative size to the tunnel into account, whereas Λ depends upon the base profile's shape. A base profile is a profile without camber. The respective equations are given by Equation 2.6.21 and 2.6.22, where y_t is the base profile's ordinate at the chord-wise location x, $\frac{dy_t}{dx}$ is the base profile's surface slope at x and $c_{p_{inc.}}$ is the pressure coefficient of the base profile at x in an incompressible fluid. Values for Λ for the RG-15C at different AoAc are provided by Table 2.6.

$$\sigma = \frac{\pi^2}{48}\left(\frac{c}{h}\right)^2 = 0.01041 \tag{2.6.21}$$

$$\Lambda = \frac{16}{\pi}\int_0^1 \frac{y_t}{c}\sqrt{[1 - c_{p_{inc.}}]\left[1 + \left(\frac{dy_t}{dx}\right)^2\right]}\, d\left(\frac{x}{c}\right) \tag{2.6.22}$$

With the factor τ defined as:

$$\tau = \frac{1}{4}\left(\frac{c}{h}\right) = 0.05625 \tag{2.6.23}$$

Tab. 2.6.: Calculated values of the factor Λ for the base profile of the RG-15 at different AoAc.

AoAc:	-7.25°	-4.25°	-1.25°	1.75°	4.75°	7.75°	8.75°	9.75°	10.75°	11.75°	13.75°
Λ:	0.1358	0.1493	0.1627	0.1759	0.1887	0.2009	0.2049	0.2088	0.2126	0.2164	0.2237

Allen and Vincenti [2] found for the final correction of the measured drag coefficient $c_d{}'$ depended on the measured Mach number Ma'

$$c_d = c_d{}'\left\{1 - \frac{2 - (Ma')^2}{\left[1 - (Ma')^2\right]^{\frac{3}{2}}}\Lambda\sigma - \frac{1 + 0.4\,(Ma')^2}{\left[1 - (Ma')^2\right]^{\frac{3}{2}}}\Lambda\sigma - \frac{\left[2 - (Ma')^2\right]\left[1 + 0.4\,(Ma')^2\right]}{1 - (Ma')^2}\tau c_d{}'\right\} \tag{2.6.24}$$

which yields for incompressible flow conditions:

$$c_d = c_d{}'\left(1 - 3\Lambda\sigma - 2\tau c_d{}'\right) \tag{2.6.25}$$

In Equation 2.6.24, the first $\Lambda\sigma$ term is associated with the dynamic pressure change caused by the interference between the walls and the airfoil. The effect on the pressure gradient induced by the interference between the wake and the walls is represented by the second $\Lambda\sigma$ term. The second dynamic pressure change resulting from a wall-wake interference is accounted for by the $\tau {c_d}'$ term [2]. Following on, for incompressible fluid conditions, the corrections of the measured to the free-air condition lift coefficient ${c_l}'$, moment coefficient ${c_m}'$, velocity ${v_\infty}'$, AoAc α' and Reynolds number Re' are stated in Equation 2.6.26 until Equation 2.6.30.

$$c_l = {c_l}' \left(1 - \sigma - 2\Lambda\sigma - 2\tau {c_d}'\right) \tag{2.6.26}$$

$$c_m = {c_m}' \left(1 - 2\Lambda\sigma - 2\tau {c_d}'\right) \tag{2.6.27}$$

$$v_\infty = {v_\infty}' \left(1 + \Lambda\sigma + \tau {c_d}'\right) \tag{2.6.28}$$

$$\alpha = \alpha' + \frac{57.3\sigma}{2\pi} \left({c_l}' + 4{c_m}'\right) \tag{2.6.29}$$

$$Re = Re' \left(1 + \Lambda\sigma + \tau {c_d}'\right) \tag{2.6.30}$$

2.7. Software

The aim of this section is to briefly introduce the utilized software and their purpose throughout this thesis. The section's first part is dedicated to the software needed to conduct the experiments inside the L1-B. The second part presents the utility software and the scripting language python. In the third and last part, the preprocessing software Pointwise V18.4R3 and the CFD simulation software ANSYS FENSAP-ICE 2021 R1 are described.

Laboratory software *LabVIEW v2020* from National Instruments Corp. [16] is commonly used throughout diverse laboratories. As stated in section 2.5.2, a custom pressure box was designed, which required also the development of a custom data acquisition software. This was done by the electronics laboratory of the VKI with LabVIEW v2020 and contained a graphical interface for the experimentalist to communicate with the pressure box acquisition system.

Utility software To prepare and analyse the results of the experimental campaign, multiple utility software were necessary. *Microsoft Visual Studio 2019* served as the integrated development environment [29] for the programming language *Python 3.7*. Python is next to MATLAB one of the most utilized programming languages throughout the science community [36]. The language has the ability to add a large amount of developer community written packages, which are containing the functionalities and libraries to solve specific tasks like importing or converting data files. This is why all the experimental data analysis tools necessary for this thesis were developed and written with Python.

The software *XFLR5 v6.48* is released under the GNU Gemeral Puplic License [55] and was used to blend the RG-15 airfoil to the RG-15C airfoil.

The Java based experimental image processing and analysis tool *ImageJ v1.58i* was originally developed by an employee of the Federal Government at the National Institutes of Health [27]. Within this thesis, ImageJ was used to efficiently measure distances and angles as well as to determine the profile coordinates of the wind tunnel wing model.

Simulation software Multiple types of numerical simulations were conducted during this thesis. The under the GNU General Public License released software *XFOIL v6.99* [19] was indispensable for predicting pressure, lift, drag, and moment levels of the wing model and therefore having a basis on which to choose the correct sensor ranges. For the viscous analysis of the subsonic isolated airfoils, the standard value of the XFOIL's envelope e^n transition criterion [18] was altered from $n = 9$ to $n = 3.15$ to take the present turbulence intensity levels inside the L1-B of 0.8% [52] into account. XFOIL also served as the analysis tool to calculate the pressure coefficient distribution along the base profile of the RG-15C. As mentioned earlier, a base profile is a profile without a chamber. This distribution was necessary for determining the geometry parameter Λ of the 2D wind tunnel wall flow interference compensations (see section 2.6).

Pointwise V18.4R3 [37] was selected as the CFD mesh generation software. Herein, the T-Rex meshing algorithm allows to rapidly generate hybrid meshes, which consists out of quad cell elements near walls to resolve the boundary layer and triangle cells elsewhere to discretize the pressure far-field. Additionally, the same meshing software and airfoil geometry of this thesis was used by Fajt [20]. This allowed the usage of his already with a grid dependency study validated meshing parameters. His taken over parameter set and meshing methodology for the clean airfoil and the iced-airfoil are presented in the subsequent section.

One of the goals of this thesis is to compare the experimental data on performance penalties on a typical UAV airfoil for low Reynolds numbers introduced by artificial 3D-printed ice shapes to numerical simulations. The FENSAP module of *ANSYS FENSAP-ICE 2021 R1* was used to conduct the CFD simulations. ANSYS FENSAP-ICE's key features are situated in the phenomena study of in-flight icing, like ice accretion calculations and the aerodynamic performance penalty analysis of the adverse effects resulting from ice accretion [5]. The boundary conditions and simulation settings are also explained in the section below.

2.8. Numerical analysis methods

The following section on the applied numerical analysis methods starts with the description of the clean and iced RG-15C performance grid generation. Here, the grid dependency study by Fajt [20] is outlined and its referencing for this thesis is explained. Afterwards, the physical and numerical modelling inside the FENSAP steady-state CFD simulations are pointed out and the section concludes with a surface roughness estimation of the artificial 3D printed ice shapes.

2.8.1. Grid generation and dependency study

The grid generation was done according to the proposed grid parameters set by Fajt [20]. Fajt investigated both, the numerical ice accretion with FENSAP-ICE and the aerodynamic performance penalties introduced by the numerically generated ice shapes. He conducted his analysis on a RG-15 airfoil with a blunt trailing edge of 1mm height and a chord length of 450mm. The performance grid for his flow analysis of the clean and the iced RG-15 was also generated with the aid of Pointwise and its meshing algorithm T-Rex.

Grid dependency study Fajt performed a grid dependency study on his performance grid and chose the grid resolution as the dependency parameter. The study was conducted for the clean airfoil at a constant AoA of 4° and a Reynolds number of 200,000. The result of the dependency study showed

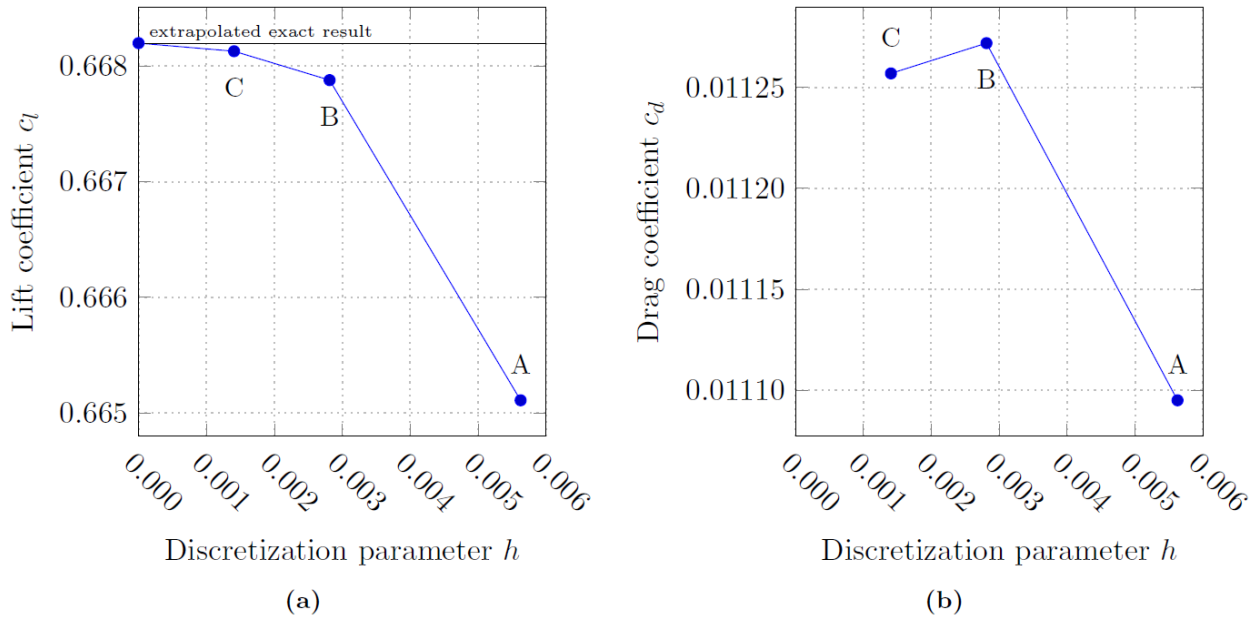

Fig. 2.15.: Grid dependency study simulation results of Fajt [20] with grid resolutions of A=80 points, B=160 points, and C=320 points for his RG-15 airfoil performance grid. Grid A is within 0.5% of the exact lift coefficient and grid A to C are within 0.1% of the predicted drag coefficient. From Fajt (2019) [20].

a distribution of n=160 points to be the most computation time-efficient with negligible lift and drag deviations from the exact result (see Figure 2.15 [20]). The conclusion of Fajt regarding the selected turbulence model was, that the Spalart-Allmaras model is reasonably capable of predicting the experimental lift and drag coefficient data from Selig et al. [46], when the flow transition locations from laminar to turbulent flow, as computed by XFOIL, are specified separately. Consequently, since the Reynolds number regimes, the ice shapes, and the airfoil geometry of Fajt are similar to the ones' used in this thesis, his validated grid parameters were adapted without performing another own grid dependency study.

RG-15C airfoil performance grid In Table 2.7 the grid parameters of the RG-15C hybrid O-grid are summarized. A hybrid O-grid combines a structured quad cell grid near the airfoil to resolve its boundary layer and an unstructured triangle cell grid for the discretization of the far field. A weighted tanh-distribution applied a 0.1mm spacing towards the leading edge and a 0.3mm spacing towards the trailing edge to the discretization of the airfoil sides. A constant spacing of 0.3mm was set for the blunt trailing edge. According to Schwarze [44, p. 155], the usage of a low Reynolds turbulence model requires a dimensionless wall distance of the nearest wall grid point of $y+ \leq 1$. This is required to adequately resolve the viscous sub- and transient layers of the boundary layer. To achieve this dimensionless wall distance also for the highest tested and simulated Reynolds number of 750,000, the initial wall spacing of the structured grid near the airfoil was set to $\Delta s = 1.0 \cdot 10^{-6} m$. The growth rate was chosen to be 1.1, which is 0.1 smaller than the preferably suggested growth rate of the gridding guidelines by Mavriplis et al. [31]. According to Mavriplis et al. [31] the resulting hybrid O-grid is settled in the medium resolution region. Figure 2.16 to Figure 2.18 are visualizing the discretised RG-15C. The hybrid O-grid needed to be extruded by one step in span-wise direction to retrieve a 2D performance mesh suitable for the FENSAP steady-state CFD calculations.

Tab. 2.7.: RG-15C performance grid parameters.

Parameter	Setting
Dimension	2D
Airfoil discretization	160 points for lower and upper airfoil side, tanh-distributed, 8 points for trailing edge equally distributed
Chord length	$c = 0.45m$
Initial cell height	$\Delta s = 1.0 \cdot 10^{-6}$
Boundary layer discretization	Minimum of 1 full structured layer
Growth rate of structured layers	1.1
Circular far field discretization	140 points equally distributed and unstructured triangular cells
Circular far field diameter	$66.7c = 30m$
Grid decay	0.9
Number of cells	$\approx 80,000$

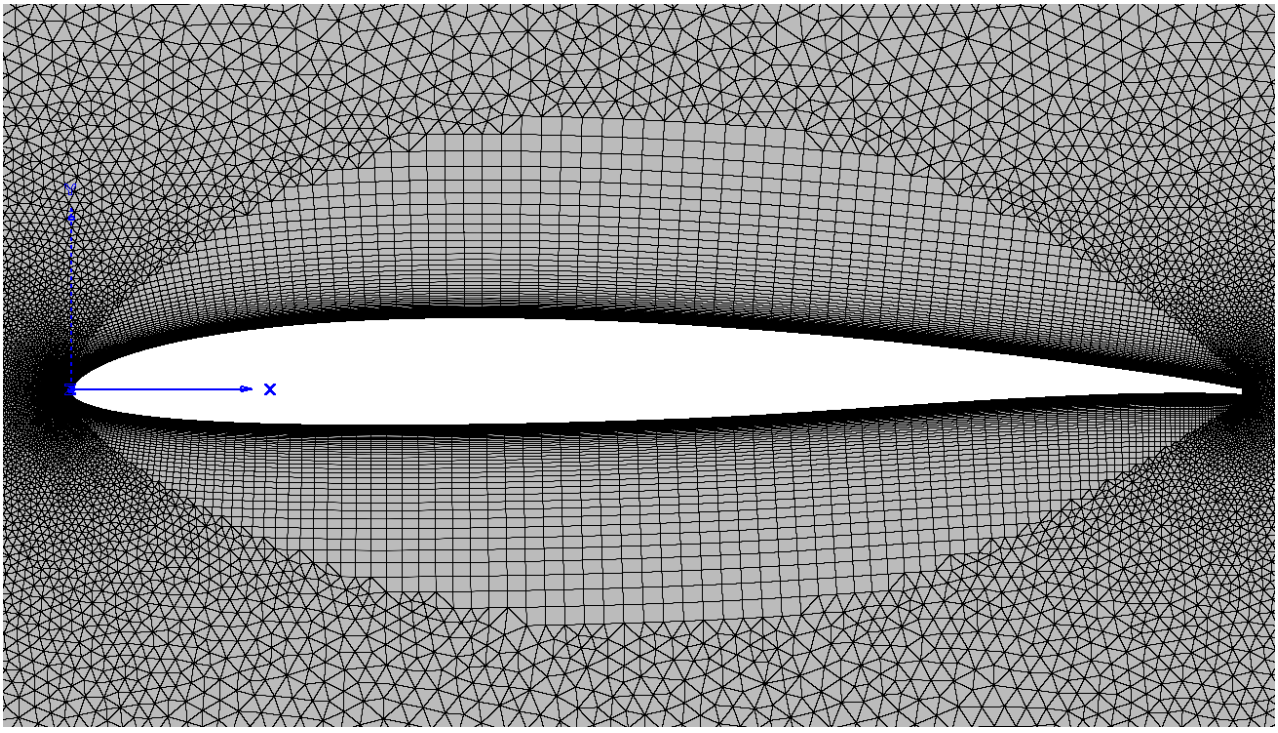

Fig. 2.16.: Hybrid O-grid of the RG-15C with a structured boundary layer and a unstructured far field discretization.

Ice shape grids Hence, the tested 3D-printed artificial ice shapes were predefined, only a few adaptations had to be conducted for the performance ice shape hybrid O-grid. They were discretised with a constant spacing of 0.1mm, which more than doubled their grid's number of cells compared to the clean RG-15C performance grid (see Table 2.8). Inside the wind tunnel, the 3D-printed artificial ice shapes were applied on the wing with duct tape (see Figure 2.8). In order to take this smoothing into account, the transition of the ice shape ends to the airfoil surfaces was approximated by an inclined straight line. The uncovered upper and lower airfoil surfaces were again discretised by 160

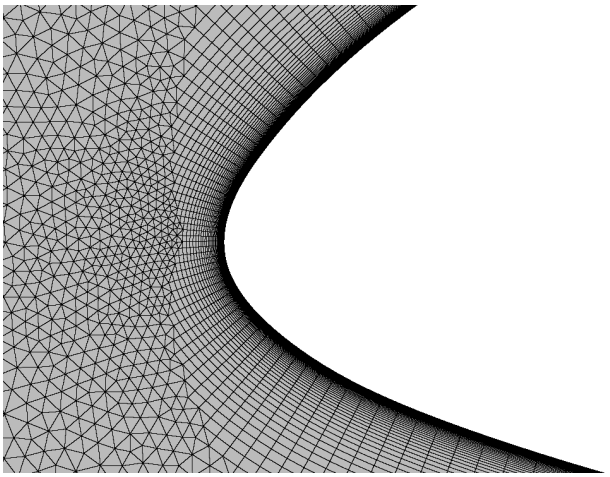

Fig. 2.17.: Close up of the leading edge RG-15C performance hybrid O-grid.

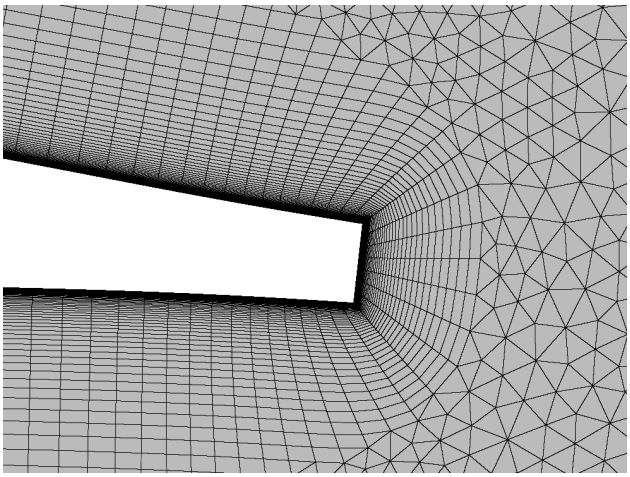

Fig. 2.18.: Close up of the trailing edge RG-15C performance hybrid O-grid.

tanh-distributed points. A close-up of the leading edge region with the glaze, rime, and mixed ice shape is provided by Figure 2.19.

Tab. 2.8.: Total cell number of the different ice shape performance grids.

Ice shape	Number of points	Number of cells
Glaze	980	191,164
Rime	794	176,728
Mixed	822	167,775

2.8.2. Physical modelling of the ANSYS FENSAP module

The ANSYS FENSAP module utilizes Reynolds-averaged Navier-Stokes equation (RANS) fluid simulations combined with the one-equation Spalart-Allmaras turbulence model, which is of first-order closure. The ANSYS FENSAP module CFD simulation settings are provided in Table 2.9.

Tab. 2.9.: ANSYS FENSAP module CFD simulation settings.

Parameter	Setting
Turbulence model	Spalart-Allmaras
Transition clean RG-15C	Fixed transition locations
Transition iced RG-15C	No transition / fully turbulent boundary layer
Artificial viscosity	$1 \cdot 10^{-7}$
CFL number	900
Number of time steps	5000

The governing equations With governing equations, the three basic principles of mass, momentum and energy conservation inside a flow field are expressed. The notation is done in the compact and

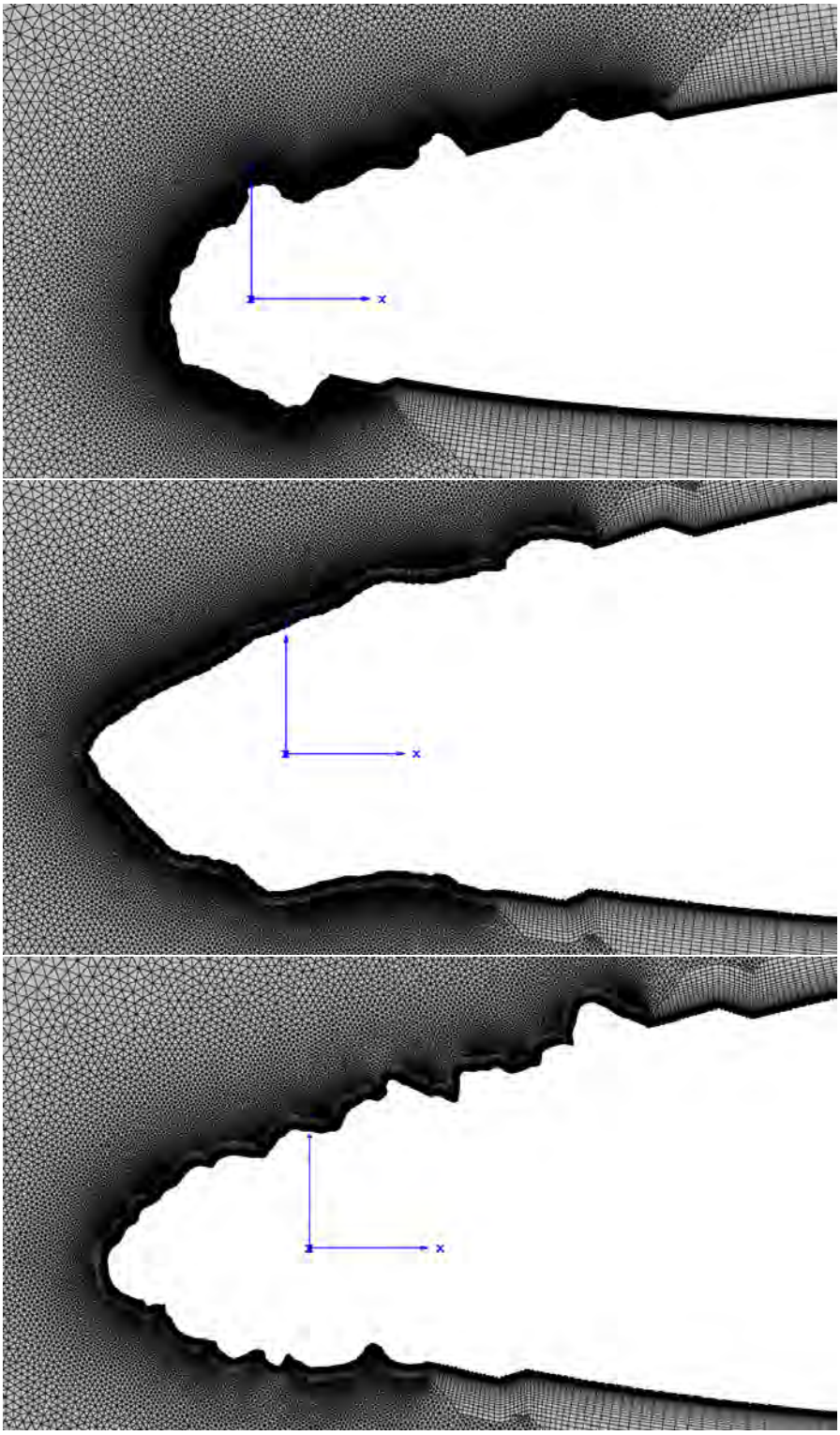

Fig. 2.19.: Close-up of the glaze (top), rime (middle), and mixed (bottom) ice shape performance grids.

clear differential form as provided by Blazek [12]. The conservation of mass, momentum and energy is given for a Newtonian fluid by the differential Navier-Stokes equations in Cartesian coordinates:

$$\begin{aligned} \frac{\partial \rho}{\partial t} + \frac{\partial}{\partial x_i}\left(\rho v_i\right) &= 0 \\ \frac{\partial}{\partial t}\left(\rho v_i\right) + \frac{\partial}{\partial x_j}\left(\rho v_i v_j\right) &= -\frac{\partial p}{\partial x_i} + \frac{\partial \tau_{ij}}{\partial x_j} \\ \frac{\partial}{\partial t}\left(\rho E\right) + \frac{\partial}{\partial x_j}\left(\rho v_j H\right) &= \frac{\partial}{\partial x_j}\left(v_j \tau_{ij}\right) + \frac{\partial}{\partial x_j}\left(k \frac{\partial T}{\partial x_j}\right) \end{aligned} \tag{2.8.1}$$

$$\tau_{ij} = 2\mu S_{ij} + \lambda \frac{\partial v_k}{\partial x_k}\delta_{ij} = 2\mu S_{ij} - \left(\frac{2\mu}{3}\right)\frac{\partial v_k}{\partial x_k}\delta_{ij} \tag{2.8.2}$$

$$S_{ij} = \frac{1}{2}\left(\frac{\partial v_i}{\partial x_j} + \frac{\partial v_j}{\partial x_i}\right) \tag{2.8.3}$$

Herein, the source terms were left out, v_i is a velocity component in the coordinate direction x_i of the velocity vector $\vec{v} = [v_1, v_2, v_3]^T$, k is the thermal conductivity coefficient, T is the absolute static temperature, E is the total energy and H is the total enthalpy. The equations contains the so called viscous stress tensor τ_{ij}, which is defined according to Equation 2.8.2 with the aid of Stokes's hypothesis, also known as the bulk viscosity:

$$\lambda + \frac{2}{3}\mu = 0 \tag{2.8.4}$$

Where λ denotes the second viscosity coefficient and μ the dynamic viscosity coefficient. Inside Equation 2.8.2, the strain-rate tensor S_{ij} (see Equation 2.8.3) and the term $\frac{\partial v_k}{\partial x_k}$ are related to the velocity divergence of the compressible flows. Besides the symmetric part of the velocity gradient represented by S_{ij}, the antisymmetric part is covered by the rotation-rate tensor:

$$\Omega_{ij} = \frac{1}{2}\left(\partial v_i \partial x_j - \frac{\partial v_j}{\partial x_i}\right) \tag{2.8.5}$$

In Equation 2.8.1, the total energy and enthalpy per unit mass are obtained from Equation 2.8.6 and Equation 2.8.7, where the fluids internal energy per unit mass e or mass specific enthalpy h is added to its kinetic energy per unit mass $\frac{1}{2}v_i v_i$ respectively.

$$E = e + \frac{1}{2}v_i v_i \tag{2.8.6}$$

$$H = h + \frac{1}{2}v_i v_i \tag{2.8.7}$$

Reynolds averaging methodologically separates the flow variables into a fluctuating and a mean part as exemplary shown for the velocity component v_i in Equation 2.8.9. Additionally, the mean part of the velocity component $\overline{v}_i$ is time averaged:

$$\overline{v}_i = \lim_{T\to\infty}\frac{1}{T}\int_t^{t+T} v_i \mathrm{d}t \tag{2.8.8}$$

$$v_i = \overline{v}_i + v_i' \tag{2.8.9}$$

Therefore, when applying Equation 2.8.8 onto Equation 2.8.1, the resulting Equations 2.8.10 are already the searched RANS equations. The difference between the Navier-Stokes equations and the

RANS equations is the additional Reynolds-stress tensor ${\tau_{ij}}^R$, which takes the momentum transfer caused by turbulent fluctuations into account (see Equation 2.8.11).

$$\begin{aligned} \frac{\partial \overline{v}_i}{\partial x_i} &= 0 \\ \rho \frac{\partial \overline{v}_i}{\partial t} + \rho \overline{v}_j \frac{\partial \overline{v}_i}{\partial x_j} &= -\frac{\partial \overline{p}}{\partial x_i} + \frac{\partial}{\partial x_j} \left(\overline{\tau}_{ij} - {\tau_{ij}}^R \right) \end{aligned} \tag{2.8.10}$$

$${\tau_{ij}}^R = -\rho \overline{v_i' v_j'} = -\rho \left(\overline{v_i v_j} - \overline{v}_i \overline{v}_j \right) \tag{2.8.11}$$

The tensor $\overline{\tau}_{ij}$ in Equation 2.8.10 represents the Reynolds-averaged evaluation of the laminar viscous stresses as noted in Equation 2.8.2 and 2.8.3:

$$\overline{\tau}_{ij} = 2\mu \overline{S}_{ij} = \mu \left(\frac{\partial \overline{v}_i}{\partial x_j} + \frac{\partial \overline{v}_j}{\partial x_i} \right) \tag{2.8.12}$$

Turbulent flow model The turbulence modelling is done by approximating the Reynolds stresses in the RANS with first-order closure models. The Eddy-viscosity hypothesis builds the foundation of these models, which assumes a linear dependency of the turbulent shear stress on the mean strain rate, as it is the case in a laminar flow. For an Reynolds-averaged incompressible flow, this hypothesis can be expressed as

$${\tau_{ij}}^R = -\rho \overline{v_i' v_j'} = 2\mu_T \overline{S}_{ij} - \frac{2}{3} \rho K \delta_{ij} \tag{2.8.13}$$

where μ_T is the eddy viscosity as the proportionality factor, K is the turbulent kinetic energy, and $\overline{S}_{ij}$ is the Reynolds-averaged strain-rate tensor. The goal of the first-order closure turbulent models is to calculate the eddy viscosity μ_T. For this thesis, the one-equation *Spalart-Allmaras Model* was selected as the turbulence model for its ability to allow continuous transitions from laminar to turbulent flows at locations indicated by the user. According to Blazek [12, p. 225], the adverse pressure gradients of turbulent flows are reasonably predicted by the Spalart-Allmaras Model and it is numerically advantageous in its robustness, fast steady-state convergence and only moderate near-wall gird resolution requirement. The Spalart-Allmaras Model uses a transport equation of a modified eddy viscosity $\tilde{\nu}$ to derive the eddy viscosity μ_T in the form:

$$\mu_T = f_{v1} \rho \tilde{\nu} \tag{2.8.14}$$

The transport equation of $\tilde{\nu}$ is given by:

$$\begin{aligned} \frac{\partial \tilde{\nu}}{\partial t} + \frac{\partial}{\partial x_j} \left(\tilde{\nu} v_j \right) =& C_{b1} \left(1 - f_{t2} \right) \tilde{S} \tilde{\nu} \\ &+ \frac{1}{\sigma} \left\{ \frac{\partial}{\partial x_j} \left[\left(\nu_L + \tilde{\nu} \right) \frac{\partial \tilde{\nu}}{\partial x_j} \right] + C_{b2} \frac{\partial \tilde{\nu}}{\partial x_j} \frac{\partial \tilde{\nu}}{\partial x_j} \right\} \\ &- \left[C_{w1} f_w - \frac{C_{b1}}{\kappa^2} f_{t2} \right] \left(\frac{\tilde{\nu}}{d} \right)^2 + f_{t1} \| \Delta \vec{v} \|_2^2 \end{aligned} \tag{2.8.15}$$

where d is the nearest distance to the wall, ν_L is the laminar kinematic viscosity, $\tilde{S}$ and f_{v1} are production terms, and f_w is the controlling destruction term of the eddy viscosity. The transition from laminar to turbulent flow is modelled by the functions f_{t1}, f_{t2}, and $\| \Delta \vec{v} \|_2^2$. The constants are $C_{b1} = 0,1355$, $C_{b2} = 0,622$, $\sigma = 2/3$, $\kappa = 0,41$, and $C_{w1} = 3,23907$. The detailed definition of the production and destruction terms are provided by the ANSYS FENSAP-ICE user manual [4] or by Blazek [12] in his book on computational fluid dynamics from where the notation of the in this section presented equations was adopted from.

2.8.3. Artificial 3D-printed ice-shape roughness estimation

The turbulence modelling of the ice-shape performance grids was also conducted with the Spalart-Allmaras turbulence model, as according to Chung and Addy [15] it is recommended for icing simulations in manned aircraft. On this occasion, it was assumed that no transition of laminar to turbulent flow occurs, since the ice shape surface roughness (SR) and topology causes the boundary layer to instantaneously trip. The SR of the artificial 3D-printed ice shapes was estimated with the aid of the work from Arnold et al. [6], who performed parameter dependant surface quality measurements on 3D-printed models. As the ice shapes were printed with a resolution of 0.1mm, the average value of Arnold et al.'s roughness measurements at 0.1mm resolution was taken as a reference value (see Figure 2.20). This yielded a roughness of $Ra = 3.25\mu m$ for the ice shapes. Furthermore, since FENSAP uses an equivalent sand-grain roughness model for imposing roughness to a wall boundary condition, the proposed relation between equivalent sand-grain roughness ε and SR Ra by Adams et al. [1] was used as transformation:

$$\varepsilon = 5.863Ra = 19.1\mu m \tag{2.8.16}$$

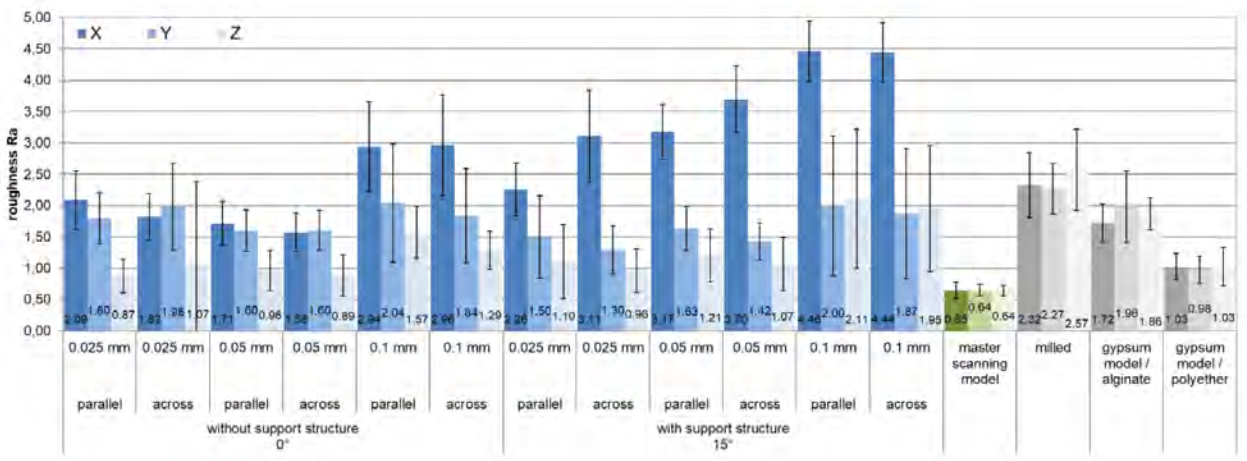

Fig. 2.20.: Averaged surface roughness of 3D-printed models as function of printing resolution and measurement technique. From Arnold et al. (2019) [6].

3. Results

One major goal of this thesis is the contribution to the numerical validation of the ANSYS FENSAP module on aerodynamic penalties induced by typical icing conditions at low Reynolds numbers. This is why an experimental campaign and numerical simulations at similar reference conditions were conducted on the typical mid-sized fixed-wing UAV airfoil RG-15. The investigated test cases were performed for the clean airfoil and the iced airfoil with artificial 3D-printed glaze, rime, and mixed ice shapes at the Reynolds number regimes of 200,000, 400,000, and 750,000. The results of the experimental and numerical campaign regarding the ice induced aerodynamic penalties on the clean RG-15 airfoil are presented in the following. At the end of each section, a short summary of the results is provided and the chapter is closing with a section on the occurrence of LSBs and ice-induced separation bubbles correlated to velocity contour plots and pressure distributions.

3.1. Experimental results

The experimental aerodynamic penalties were evaluated with the aid of a penalty parameter set. The aerodynamic penalties of the specific ice shape onto the clean airfoil were defined by the following chosen parameters:

- Lift coefficient penalty at AoA=-1.3° $\Delta c_{l,-1.3} = \frac{c_{l,-1.3_{ice}} - c_{l,-1.3_{clean}}}{c_{l,-1.3_{clean}}}$ in [%]
- Drag coefficient penalty at AoA=-1.3° $\Delta c_{d,-1.3} = \frac{c_{d,-1.3_{ice}} - c_{d,-1.3_{clean}}}{c_{d,-1.3_{clean}}}$ in [%]
- Moment coefficient penalty at AoA=-1.3° $\Delta c_{m,-1.3} = \frac{c_{m,-1.3_{ice}} - c_{m,-1.3_{clean}}}{c_{m,-1.3_{clean}}}$ in [%]
- L/D ratio penalty at AoA=-1.3° $\Delta L/D_{-1.3} = \frac{L/D_{-1.3_{ice}} - L/D_{-1.3_{clean}}}{L/D_{-1.3_{clean}}}$ in [%]

Furthermore, sufficient data points for the glaze ice case allowed the definition of the following additional penalty parameters:

- AoA penalty of the maximum L/D ratio $\Delta\alpha_{L/D} = \alpha_{L/D_{ice}} - \alpha_{L/D_{clean}}$ in [°]
- Maximum L/D ratio penalty $\Delta L/D = \frac{L/D_{ice} - L/D_{clean}}{L/D_{clean}}$ in [%]
- Slope of the moment coefficient penalty in between -4° and +4° $\Delta\partial c_m = \frac{\partial c_m}{\partial \alpha}$ in [1/rad]

The subsequent analysed aerodynamic plots are containing the experimental data of the clean airfoil case in black, the glaze ice case in blue, the rime ice case in red, and the mixed ice case in green. The uncertainties of the experimental determined aerodynamic coefficients are indicated per data point with error bars in the same colour as the test case. As mentioned in section 2.4, a second run was performed for each velocity to cover the hysteresis effect of the measurement equipment. The results of the second runs are provided in the Appendix A.6.

3.1.1. Experimental aerodynamic penalties at Re 200,000

As displayed in Figure 3.1 (left), the lift coefficient of the clean airfoil is not affected to a great extend by the glaze ice. The lift penalties are within -4% for AoA>2.8°. As the absolute lift coefficient values reach their minimum, the relative lift coefficient penalty peaks for the glaze ice at $\Delta c_{l,-1.3}$=-36%. Glaze ice shows a significant influence on the drag levels at AoA other than -1.3° (see Figure 3.1 (centre)). At the AoA=-1.3°, the relative drag penalties range from +31% to +44% with mixed ice as the lowest and glaze ice as the highest $\Delta c_{d,-1.3}$ (see Table 3.1). A similar order of the most severe penalties is observable for the L/D ratios penalties at AoA=-1.3° with $\Delta L/D_{-1.3}$=-15% for mixed ice as the least and -55% for glaze ice as the most severe ice shape. Furthermore, glaze ice achieves its greatest $\Delta L/D$ penalty at 4.8° with up to -59% compared to the clean airfoil (see Figure 3.2 (right)). With respect to the moment coefficient, glaze ice imposes an unstable "nose-down" moment to the airfoil in the order of $+0.380\frac{1}{\text{rad}}$ (see Figure 3.1 (right)).

Tab. 3.1.: Experimental aerodynamic penalties for Re 200,000.

Case	$\Delta c_{l,-1.3}$	$\Delta c_{d,-1.3}$	$\Delta c_{m,-1.3}$	$\Delta L/D_{-1.3}$	$\Delta\alpha_{L/D}$	$\Delta L/D$	$\Delta\partial c_m$
Glaze ice	-36%	+44%	-16%	-55%	0°	-59%	$0.380\frac{1}{\text{rad}}$
Rime ice	-25%	+41%	+14%	-47%	n.a.	n.a.	n.a.
Mixed ice	+11%	+31%	-7%	-15%	n.a.	n.a.	n.a.

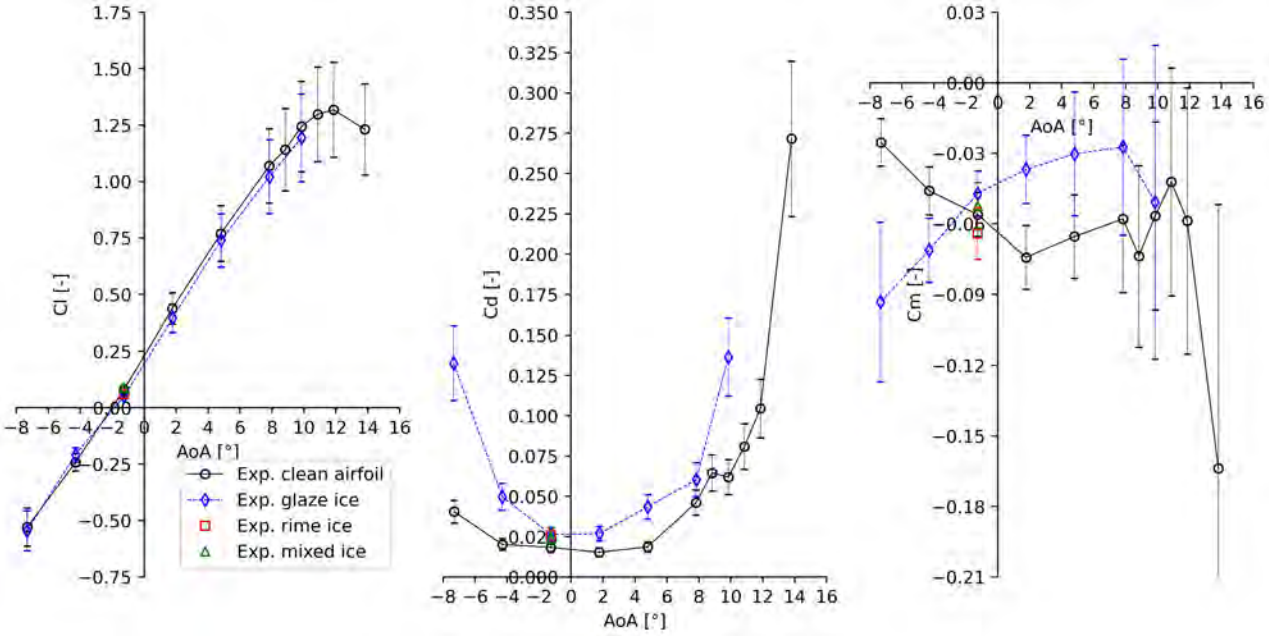

Fig. 3.1.: Plot of c_l over AoA (left), c_d over AoA (centre), c_m over AoA (right) of the experimental campaign at Re 200,000.

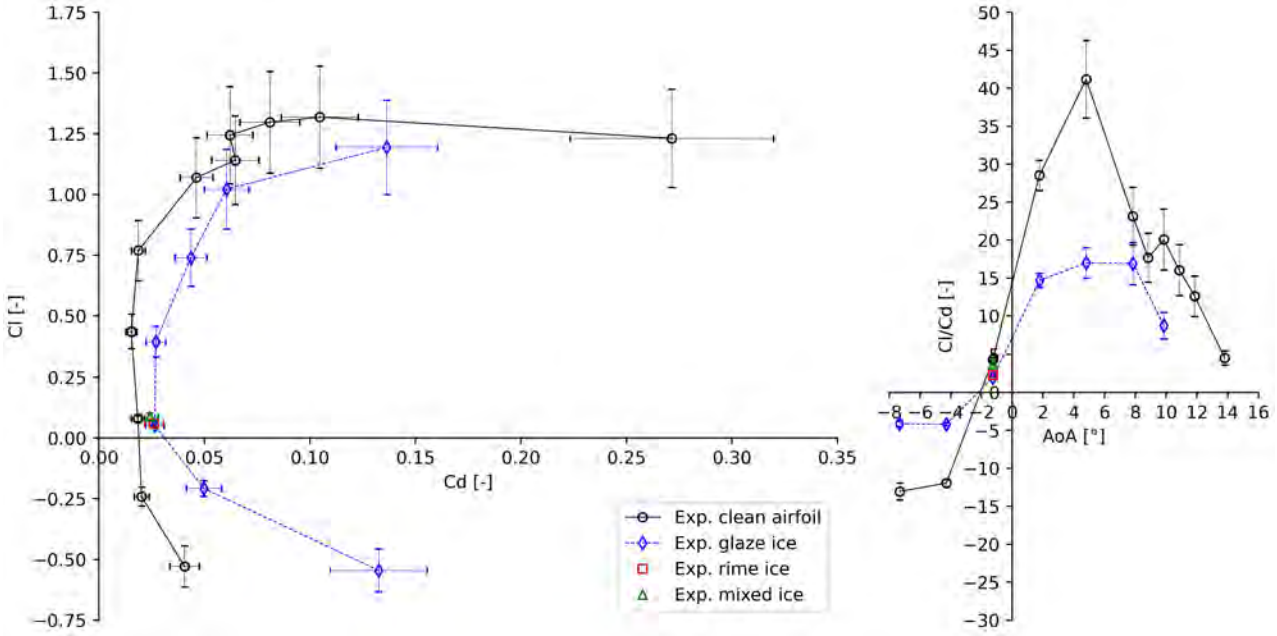

Fig. 3.2.: Plot of the drag polar (left) and the L/D ratio over AoA (right) of the experimental campaign at Re 200,000.

3.1.2. Experimental aerodynamic penalties at Re 400,000

At the Reynolds number regime of 400,000, the uncertainties of the determined aerodynamic coefficients are the lowest between -4.3°<AoA<4.8°. For AoA>4.8° the moment coefficient uncertainties δc_m are significantly increased (see Figure 3.3 (right)). At the same AoA, the onset of a non-continuous drag increase is observable for the clean airfoil in Figure 3.3 (centre). This behaviour was also seen for the tested Reynolds number of 200,000 (see Figure 3.1 (centre) and Figure 3.2 (left)). The performed angular sweep with the glaze ice shape enables the estimation of the glaze ice induced L/D ratio penalty $\Delta L/D$=-51%. The maximum L/D ratio of the glaze ice is present at the same angle as measured for the clean airfoil (see Figure 3.3 (right)). Furthermore, glaze ice induces an unstable "nose-down" moment to the RG-15 airfoil of $\Delta\partial c_m = 0.276\frac{1}{\text{rad}}$ (see Figure 3.3 (right)). While the lift coefficient of the clean airfoil is marginally affected by the glaze ice, the drag levels are overall increased (see Figure 3.4 (left)). At the AoA=-1.3° the highest drag coefficient penalty is present for the mixed ice with $\Delta c_{d,-1.3}$=+108% and the lowest for rime ice with $\Delta c_{d,-1.3}$=+70% (see Table 3.2). In contrast to that, the lowest lift and moment coefficient penalties are present for the mixed ice and the highest for glaze ice with $\Delta c_{l,-1.3}$=-54% and $\Delta c_{m,-1.3}$=-21%.

Tab. 3.2.: Experimental aerodynamic penalties for Re 400,000.

Case	$\Delta c_{l,-1.3}$	$\Delta c_{d,-1.3}$	$\Delta c_{m,-1.3}$	$\Delta L/D_{-1.3}$	$\Delta\alpha_{L/D}$	$\Delta L/D$	$\Delta\partial c_m$
Glaze ice	-54%	+91%	-21%	-76%	0°	-51%	$0.276\frac{1}{\text{rad}}$
Rime ice	-50%	+70%	-6%	-70%	n.a.	n.a.	n.a.
Mixed ice	-21%	+108%	+4%	-62%	n.a.	n.a.	n.a.

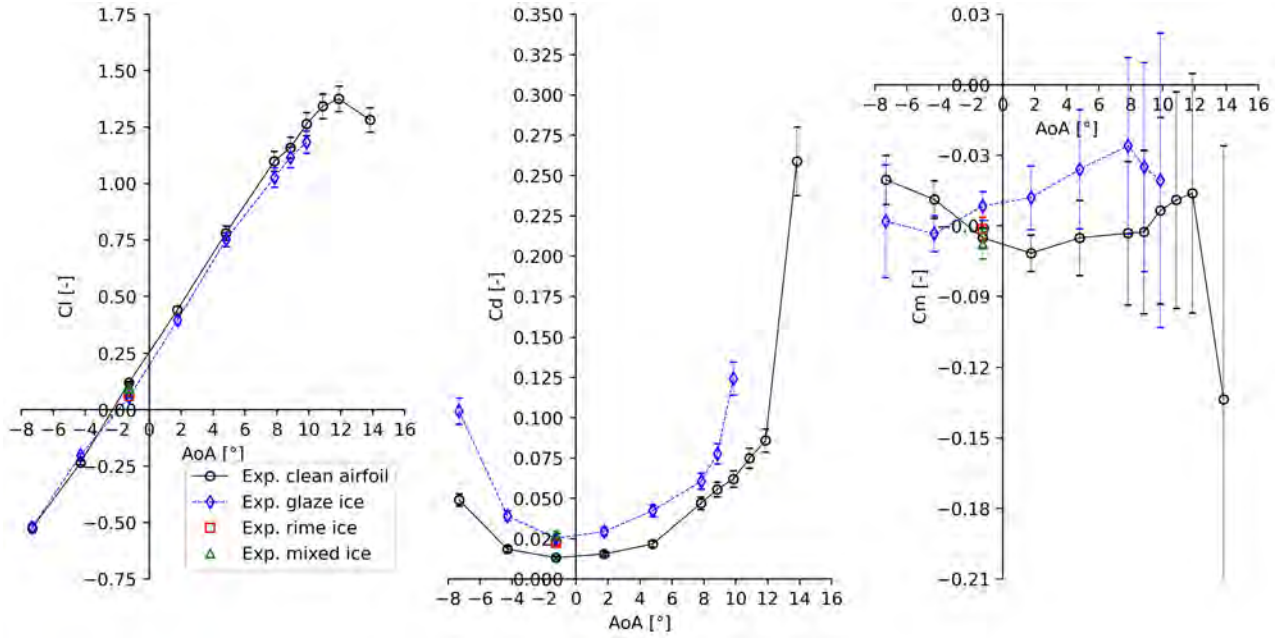

Fig. 3.3.: Plot of c_l over AoA (centre) and c_d over AoA (right) of the experimental campaign at Re 400,000.

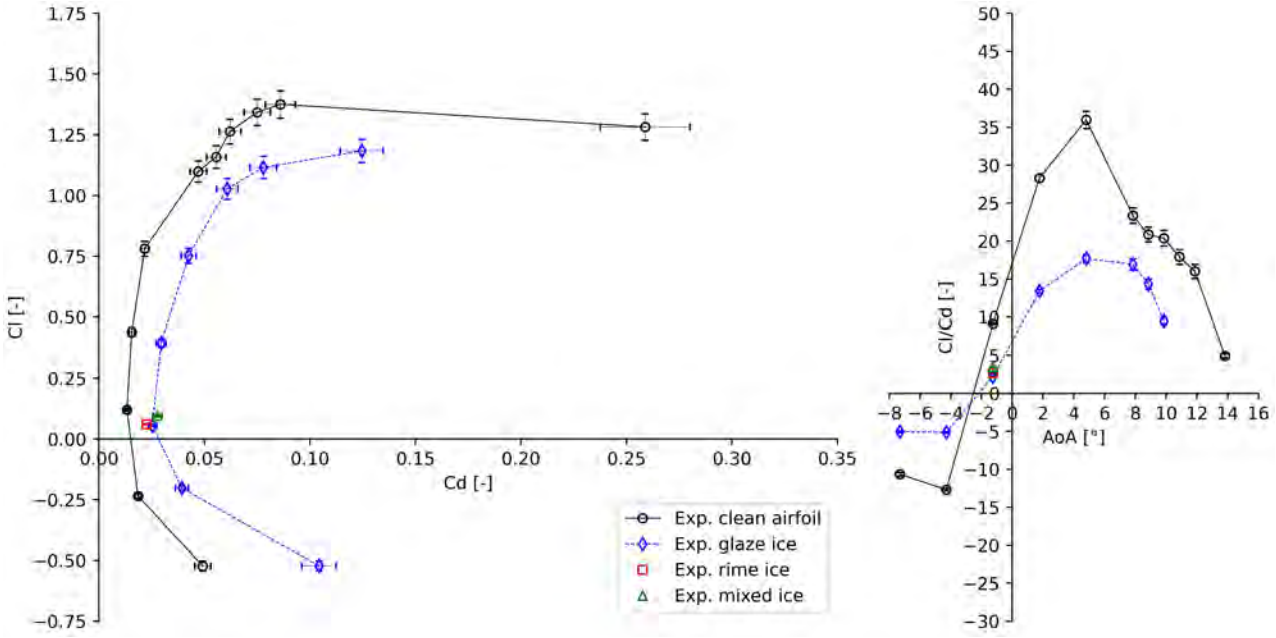

Fig. 3.4.: Plot of the drag polar (left) and the L/D ratio over AoA (right) of the experimental campaign at Re 400,000.

3.1.3. Experimental aerodynamic penalties at Re 750,000

The highest tested Reynolds number regime of 750,000 exhibits severe uncertainties at the moment coefficients of the clean airfoil for AoA>4.8° (see Figure 3.5). Starting from an AoA>9.8°, unphysical behaviour is observable in the coefficient plots (see Figure 3.5 and Figure 3.6). The non-continuous drag increase of the clean airfoil experiments for AoA>4.8°, which is present at each tested Reynolds number regime, and the unphysical behaviour at the higher AoA at $Re \approx 750,000$ are explicitly

addressed in section 4.2. Nevertheless, in between -7.25°<AoA<4.8° the low uncertainty levels permitted an analysis of the experimental data also for the Reynolds number regime of 750,000. Herein, an AoA sweep was performed for the clean airfoil and the ice shapes were only tested at an AoA=-1.3°. The at this AoA ice shape induced aerodynamic penalties are summarized in Table 3.3. The rime and glaze ice are similarly reducing the achieved clean airfoil lift coefficient by -49%, which equals a c_l=-0.05. The corresponding uncertainty of the lift coefficient determination is one order of magnitude lower with δc_l=±0.001. The highest drag penalty is noted for the glaze ice with $\Delta c_{d,-1.3}$=+130% and the lowest for rime ice with $\Delta c_{d,-1.3}$=+92%. This equals +147 drag counts for the glaze ice. In terms of the moment coefficient, only the glaze ice induces a penalty of $\Delta c_{m,-1.3}$=-11% to the clean airfoil. Consequently, the artificial glaze ice turns out as the most severe ice shape regarding the induced aerodynamic penalties onto the clean airfoil at an AoA=-1.3° and Reynolds number regime of 750,000.

Tab. 3.3.: Experimental aerodynamic penalties for Re 750,000.

Case	$\Delta c_{l,-1.3}$	$\Delta c_{d,-1.3}$	$\Delta c_{m,-1.3}$	$\Delta L/D_{-1.3}$
Glaze ice	-48%	+130%	-11%	-77%
Rime ice	-49%	+92%	-1%	-73%
Mixed ice	-31%	+117%	+1%	-68%

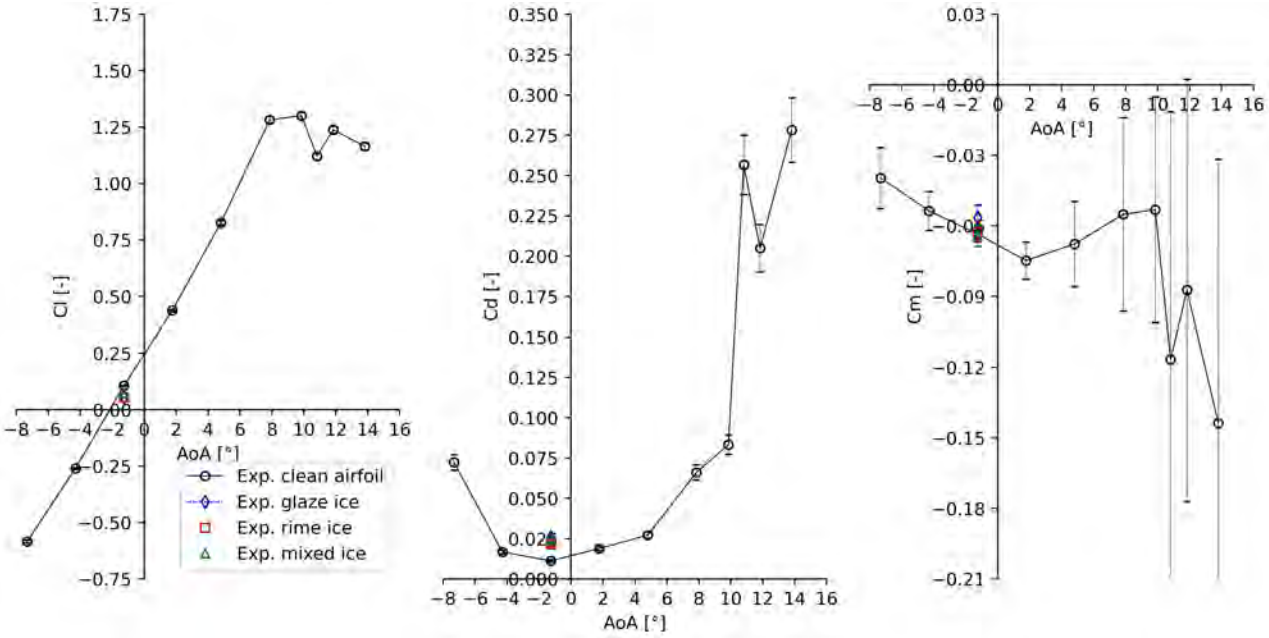

Fig. 3.5.: Plot of c_l over AoA (left), c_d over AoA (centre), c_m over AoA (right) of the experimental campaign at Re 750,000.

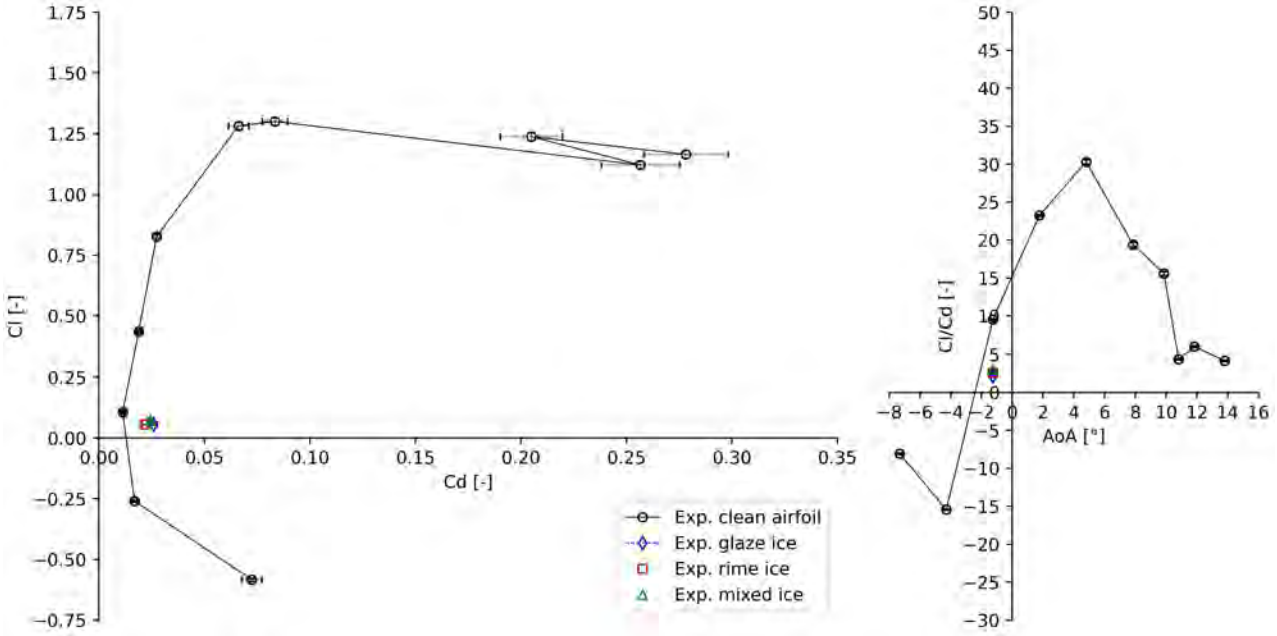

Fig. 3.6.: Plot of the drag polar (left) and the L/D ratio over AoA (right) of the experimental campaign at Re 750,000.

3.1.4. Experimental results summary

The glaze ice shape mounted at the leading edge of the RG-15 wind tunnel wing model induced overall the highest aerodynamic penalties to the baseline of the clean RG-15 airfoil. At the Reynolds number regimes of 200,000 and 400,000, the baseline drag coefficient was significantly increased at all tested AoA by the glaze ice shape. In both Reynolds number cases, the glaze ice caused an destabilizing "nose-down" moment. The highest aerodynamic penalties to the baseline RG-15 were induced by each ice shape at the highest tested Reynolds number regime of 750,000. E.g. the minimum drag coefficient of the RG-15 wind tunnel wing model was increased by the glaze ice shape with +130%, by the mixed ice shape with +117%, and by the rime ice shape with +92%. In comparison, at the Reynolds number regime of 200,000, the minimum drag coefficient of the RG-15 wind tunnel wing model was increased by each ice shape with ≈+40%. The reduction of the achievable lift at the minimum drag coefficient varied between -20% and -50%. The mixed ice shape turned out to induce the least severe lift reductions, while the rime and glaze ice shapes were at similar levels.

3.2. Numerical results

The ANSYS FENSAP module CFD simulations of the artificial 3D-printed ice shapes were conducted with a resolution of 1° between AoA=-8° and AoA=14°. This enabled a more refined analysis of the numerical simulation results. Consequently the following aerodynamic penalty parameters were defined:

- Onset of stall AoA penalty at the maximum lift coefficient $\Delta\alpha_{c_{l,max}} = \alpha_{c_{l,max_{ice}}} - \alpha_{c_{l,max_{clean}}}$ in [°]
- Maximum lift coefficient penalty $\Delta c_{l,max} = \frac{c_{l,max_{ice}} - c_{l,max_{clean}}}{c_{l,max_{clean}}}$ in [%]

- AoA penalty at the minimum drag coefficient $\Delta\alpha_{c_{d,min}} = \alpha_{c_{d,min_{ice}}} - \alpha_{c_{d,min_{clean}}}$ in [°]
- Minimum drag coefficient penalty $\Delta c_{d,min} = \frac{c_{d,min_{ice}} - c_{d,min_{clean}}}{c_{d,min_{clean}}}$ in [%]
- AoA penalty of the maximum L/D ratio $\Delta\alpha_{L/D} = \alpha_{L/D_{ice}} - \alpha_{L/D_{clean}}$ in [°]
- Maximum L/D ratio penalty $\Delta L/D = \frac{L/D_{ice} - L/D_{clean}}{L/D_{clean}}$ in [%]
- Slope of the moment coefficient penalty in between -4° and +4° $\Delta\partial c_m = \frac{\partial c_m}{\partial\alpha}$ in [1/rad]

Table 3.5, Table 3.7, and Table 3.9 are containing the reference conditions of the CFD simulations with the respective Reynolds number regime of 200,000, 400,000, and 750,000. The static temperature was set for each simulation to $T = 293.15K$. The Reynolds numbers were matched with the averaged Reynolds numbers of the experiments by imposing an adequate static pressure p_s. The set velocities v_∞ equal the averaged ones from the experimental campaign except for the clean airfoil. For the clean airfoil, the theoretical calculated velocities were imposed to the CFD reference conditions, but the adapted static pressure enabled a to the experiments similar Reynolds number. This was done, since a movement of the wing was suspected throughout the clean airfoil experiments at higher AoA. As the Mach number of maximum 0.07 for the highest velocity yields an incompressible flow regime, the effect was considered to be negligible.

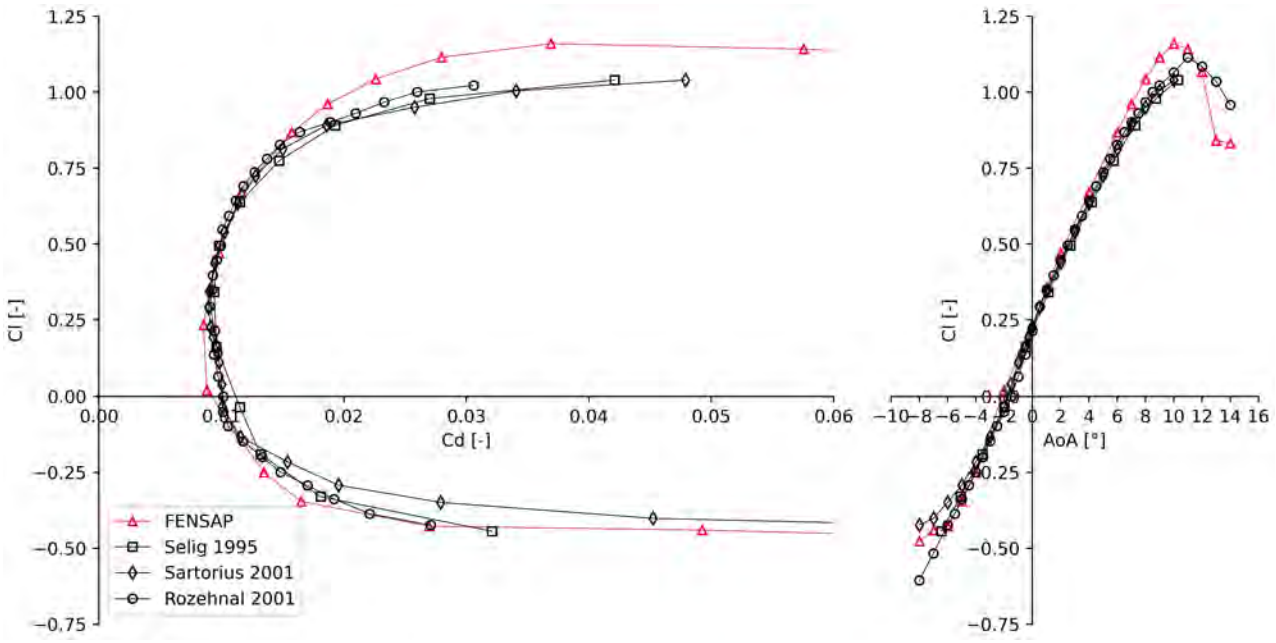

Fig. 3.7.: Drag polar (left) and c_l over AoA (right) FENSAP prediction validation with multiple experimental data for the RG-15 at Re 200,000.

Validation of the RG-15C performance grid with literature The validation of the RG-15C performance grid was conducted at a Reynolds number of 200,000 by comparing the FENSAP aerodynamic coefficient predictions with literature data from Selig et al. (1995) [46], Sartorius (2001) [42] and Rozehnal (2001), whose experiments were conducted in the course of Lutz et al. [30]. Starting with the c_l over AoA diagram from Figure 3.7, FENSAP was capable of accurately predicting the lift levels in between -8° and 6°. Above 6°, the FENSAP calculation estimated a higher $c_{l,max}$ and an earlier onset of stall in comparison to the data from Rozehnal (2001). However, the c_d levels predicted

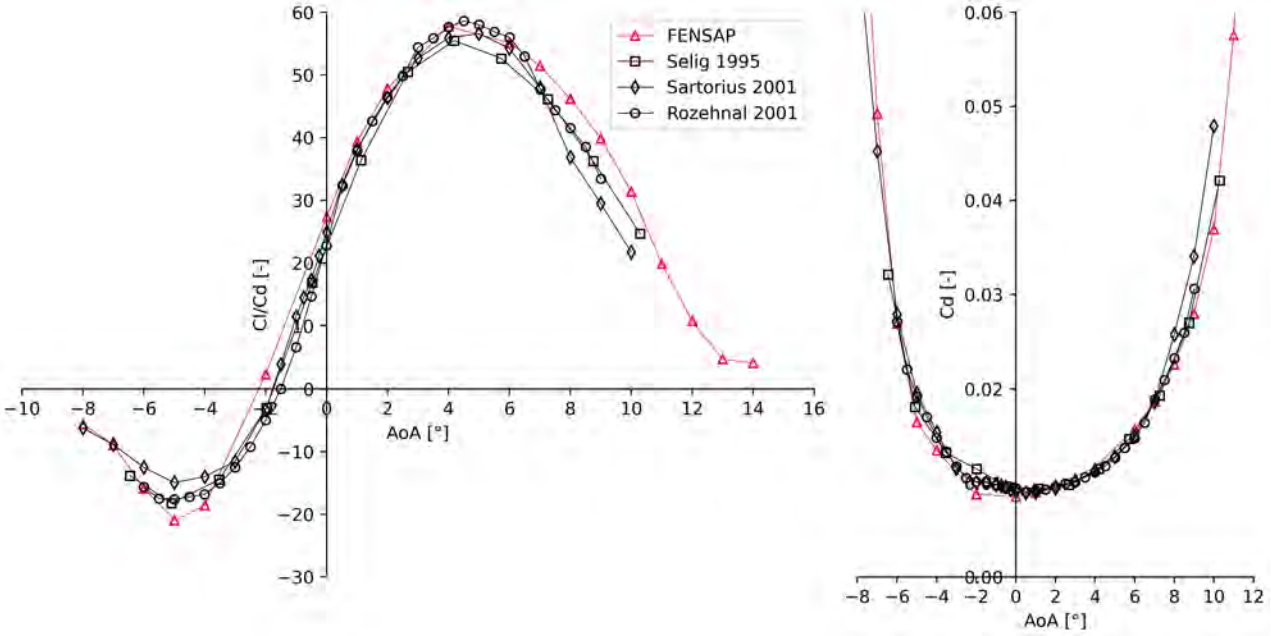

Fig. 3.8.: L/D ratio (left) and c_d over AoA (right) FENSAP prediction validation with multiple experimental data for the RG-15 at Re 200,000.

by FENSAP and the experimental c_d values were alike (see Figure 3.8). With respect to the L/D ratio over AoA, FENSAP was in congruence with the experimental data, especially in predicting the maximum and minimum L/D ratios at similar AoA (see Figure 3.8).

It was concluded that the RG-15C performance grid and the chosen Spalart-Allmaras turbulence model in combination with fixed transition locations were capable of adequately predicting the experimental clean airfoil data from literature but special care must be taken when evaluating the onset of stall.

3.2.1. Numerical aerodynamic penalties at Re 200,000

At the Reynolds number regime of 200,000, the lift coefficients of the clean and iced airfoil do not show great deviations in between -6°<AoA<+6°. The onset off stall occurs up to $\Delta\alpha_{c_{l,max}}$=-1° earlier in the iced cases. Regarding the maximum lift penalty, the lowest is present for the mixed ice with $\Delta c_{l,max}$=-6.3%, whereas rime and glaze ice are considerably higher with -17.2% and -22.1% (see Figure 3.9 (left)). All iced cases are showing in general increased drag levels compared to the clean airfoil with a $\Delta c_{d,min}$ up to +147% for the glaze ice (see Figure 3.9 (centre) and Figure 3.10 (left)). The ice shapes are causing each a similar unstable "nose down" moment with their $\Delta\partial c_m$ around $+2.2\frac{1}{\text{rad}}$ (see Figure 3.9 (right)). Motivated by the large increase in drag, the $\Delta\alpha_{L/D}$ is the greatest for the glaze ice with -60.7%, but the AoA at maximum L/D ratio remains constant at 4° (see Figure 3.10 (right)). In conclusion induced glaze ice the most severe aerodynamic penalties onto the clean airfoil at a Reynolds number regime of 200,000. The mixed ice was able to maintain especially for higher AoA lower drag and higher lift levels. Rime ice recorded the lowest $\Delta L/D$ and $\Delta c_{d,min}$ of all considered ice shapes (see Table 3.4).

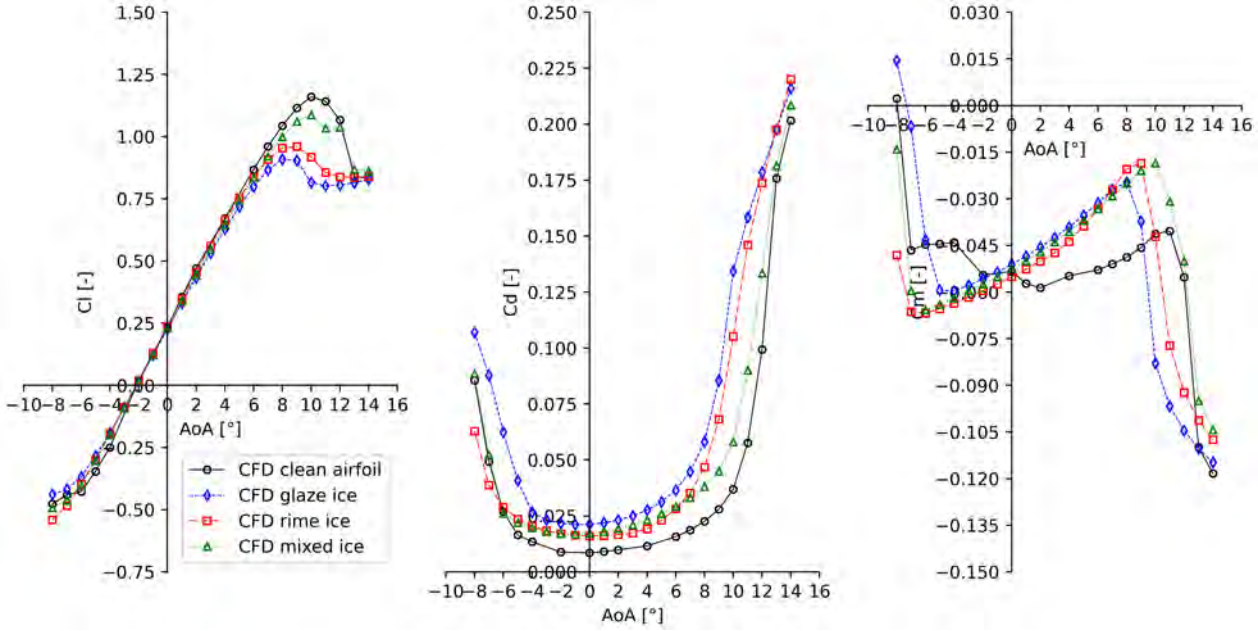

Fig. 3.9.: Plot of c_l over AoA (left), c_d over AoA (centre), c_m over AoA (right) of the FENSAP CFD simulations at Re 200,000.

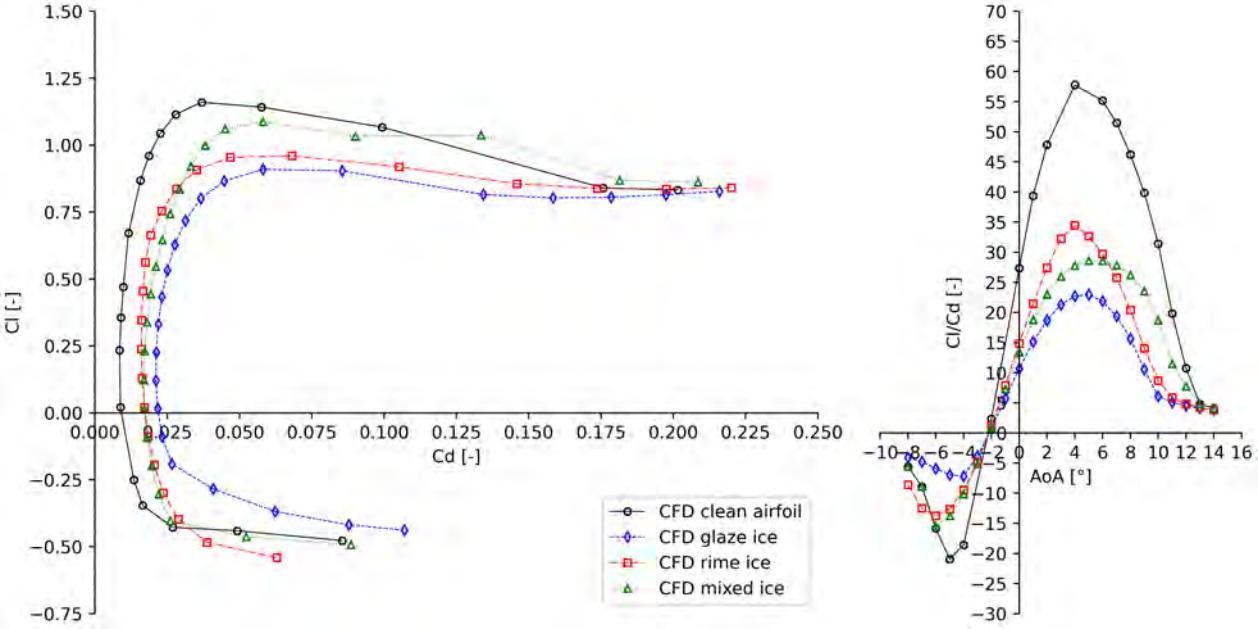

Fig. 3.10.: Plot of the drag polar (left) and the L/D ratio over AoA (right) of the FENSAP CFD simulations at Re 200,000.

Tab. 3.4.: FENSAP CFD simulation aerodynamic penalties predictions for Re 200,000.

Case	$\Delta\alpha_{c_{l,max}}$	$\Delta c_{l,max}$	$\Delta\alpha_{c_{d,min}}$	$\Delta c_{d,min}$	$\Delta\alpha_{L/D}$	$\Delta L/D$	$\Delta\partial c_m$
Glaze ice	-1°	-22.1%	-1°	+147.0%	0°	-60.7%	$+0.224\frac{1}{\text{rad}}$
Rime ice	-1°	-17.2%	0°	+88.2%	+1°	-43.4%	$+0.219\frac{1}{\text{rad}}$
Mixed ice	0°	-6.3%	-1°	+97.8%	+1°	-50.4%	$+0.230\frac{1}{\text{rad}}$

Tab. 3.5.: FENSAP CFD simulation reference conditions based on averaged experimental results for Re 200,000.

Case	Re	v_∞ $\left[\frac{m}{s}\right]$	p_s [Pa]
Clean RG-15C	197,458	6.50	103,090
Glaze ice	196,616	6.69	99,750
Rime ice	196,629	6.71	99,400
Mixed ice	201,454	6.78	100,830

3.2.2. Numerical aerodynamic penalties at Re 400,000

The FENSAP CFD simulations are predicting that mixed ice induces the lowest lift and drag penalties for AoA>7° (see Figure 3.12 (left)). The onset of stall is occurring for mixed ice 1° earlier compared to the clean RG-15C and the $\Delta c_{l,max}$=-11% (see Figure 3.11 (left)). Glaze ice shows overall the greatest aerodynamic penalties (see Figure 3.11). The minimum drag coefficient penalty reaches up to +145% and the $\Delta L/D$ penalty peaks at -63% for the glaze ice (see Table 3.6). The lowest $\Delta L/D$ and $\Delta c_{d,min}$ penalty is predicted for the rime ice. Nevertheless, the maximum L/D ratio AoA is shifted for both, glaze and rime ice, by $\Delta\alpha_{L/D}$=-2° to more negative AoA (see Figure 3.12 (right)). Each simulated ice shape induces similar unstable "nose-down" moment coefficient penalties in the order of $\Delta\partial c_m = 0.14\frac{1}{\text{rad}}$. Additionally, the glaze ice shrinks the linear coefficient moment window of the clean airfoil from -8°<AoA <12° down to -6°<AoA<8° (see Figure 3.11 (right)).

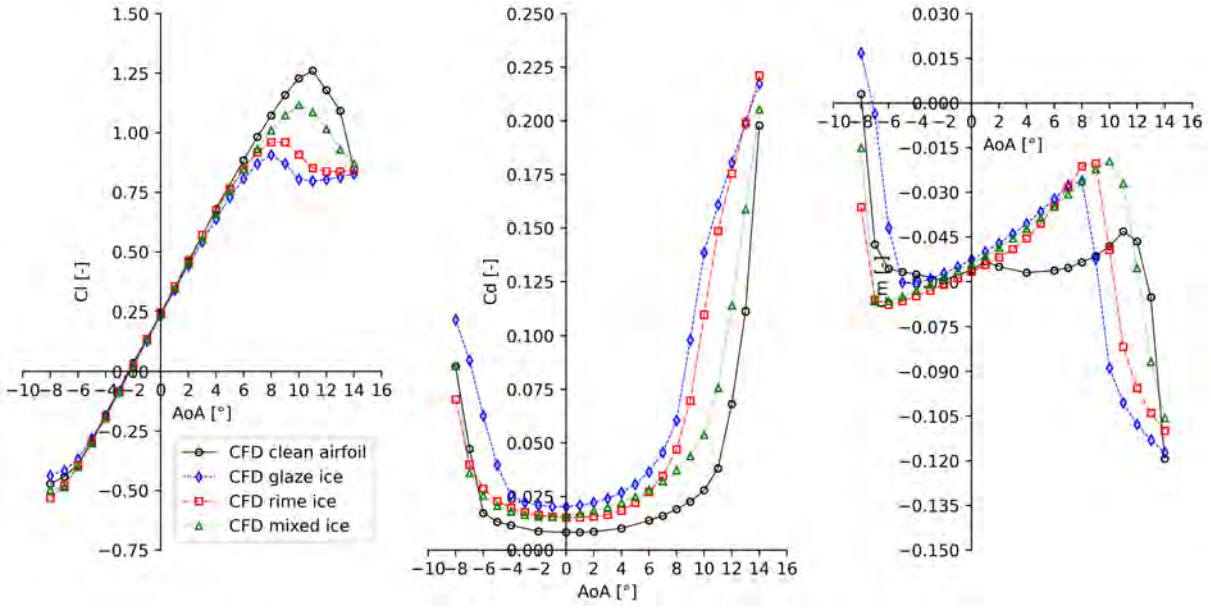

Fig. 3.11.: Plot of c_l over AoA (left), c_d over AoA (mid), c_m over AoA (right) of the FENSAP CFD simulations at Re 400,000.

Tab. 3.6.: FENSAP CFD simulation aerodynamic penalties predictions for Re 400,000.

Case	$\Delta\alpha_{c_{l,max}}$	$\Delta c_{l,max}$	$\Delta\alpha_{c_{d,min}}$	$\Delta c_{d,min}$	$\Delta\alpha_{L/D}$	$\Delta L/D$	$\Delta\partial c_m$
Glaze ice	-3°	-28.1%	0°	+144.8%	-2°	-63.0%	$+0.141\frac{1}{\text{rad}}$
Rime ice	-2°	-23.8%	0°	+83.9%	-2°	-43.0%	$+0.135\frac{1}{\text{rad}}$
Mixed ice	-1°	-11.4%	-1°	+89.1%	-1°	-52.2%	$+0.145\frac{1}{\text{rad}}$

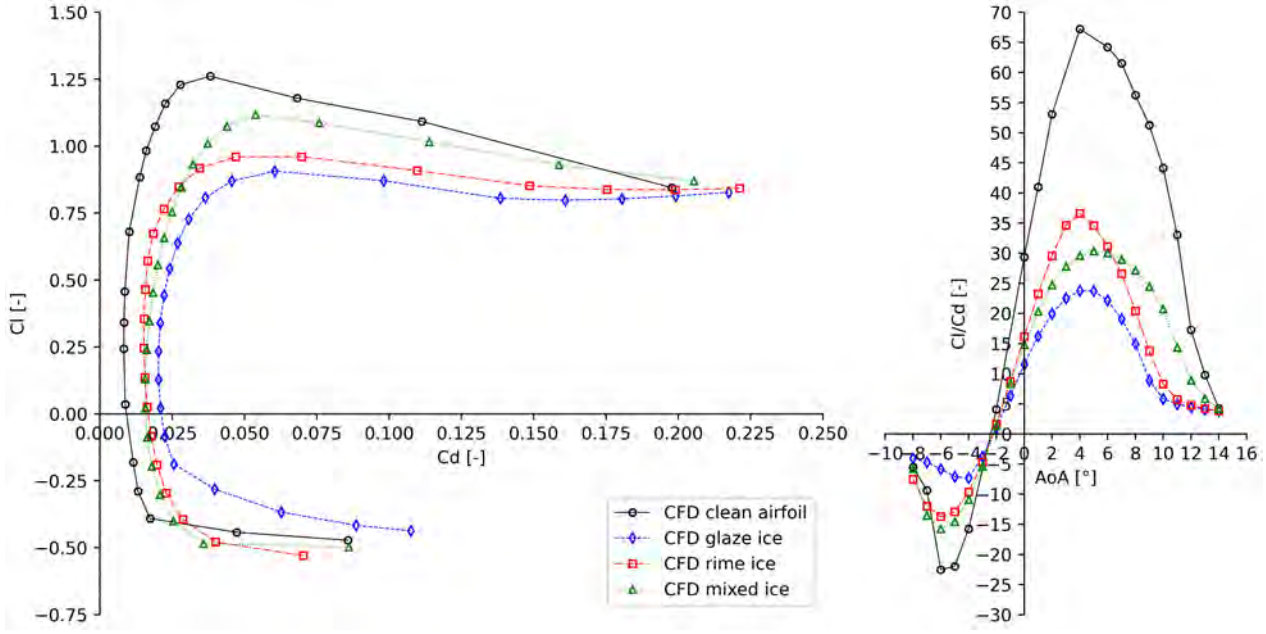

Fig. 3.12.: Plot of the drag polar (left) and the L/D ratio over AoA (right) of the FENSAP CFD simulations at Re 400,000.

Tab. 3.7.: FENSAP CFD simulation reference conditions based on averaged experimental results for Re 400,000.

Case	Re	v_∞ $\left[\frac{m}{s}\right]$	p_s [Pa]
Clean RG-15C	381,664	13.10	102,250
Glaze ice	389,686	13.26	99,756
Rime ice	389,916	13.31	99,407
Mixed ice	396,300	13.34	100,830

3.2.3. Numerical aerodynamic penalties at Re 750,000

At the Reynolds number regime of 750,000, FENSAP predicts overall the highest aerodynamic penalties from glaze ice. This is justified by the highest onset of stall AoA decrease with up to $\Delta\alpha_{c_{l,max}}$=-4°, the simultaneously $\Delta c_{l,max}$ penalty of -33%, the more than doubled minimum drag coefficient increase of $\Delta c_{d,min}$=+104% compared to rime and mixed ice, and the consequently highest $\Delta L/D$ reduction of -61% (see Table 3.8). Regarding the other ice shapes, mixed ice is able to maintain the highest lift levels and the onset off stall sets place only -1° earlier than the predicted clean airfoil (see Figure 3.13 (left)). Since mixed ice induces according to the FENSAP simulations also the lowest drag penalties at AoA>7°, it is the least severe ice shape at this AoA regime regarding the L/D ratio penalties (see Figur 3.14 (right)). On this occasion, it has to be noted that rime ice is predicted to show a similar stall behaviour as the glaze ice (see Figure 3.13 (left)) but has the lowest $\Delta L/D$ penalty with -37% (see Figure 3.14 (right)). All ice shape simulations are imposing an unstable "nose-down" moment coefficient propagation to the clean airfoil in the order of $\Delta\partial c_m$=+0.16$\frac{1}{\text{rad}}$...+0.17$\frac{1}{\text{rad}}$. Additionally, the glaze ice reduces the linear moment coefficient region of the clean airfoil from -8°<AoA <12° down to -5°<AoA<8° (see Figure 3.13 (right)).

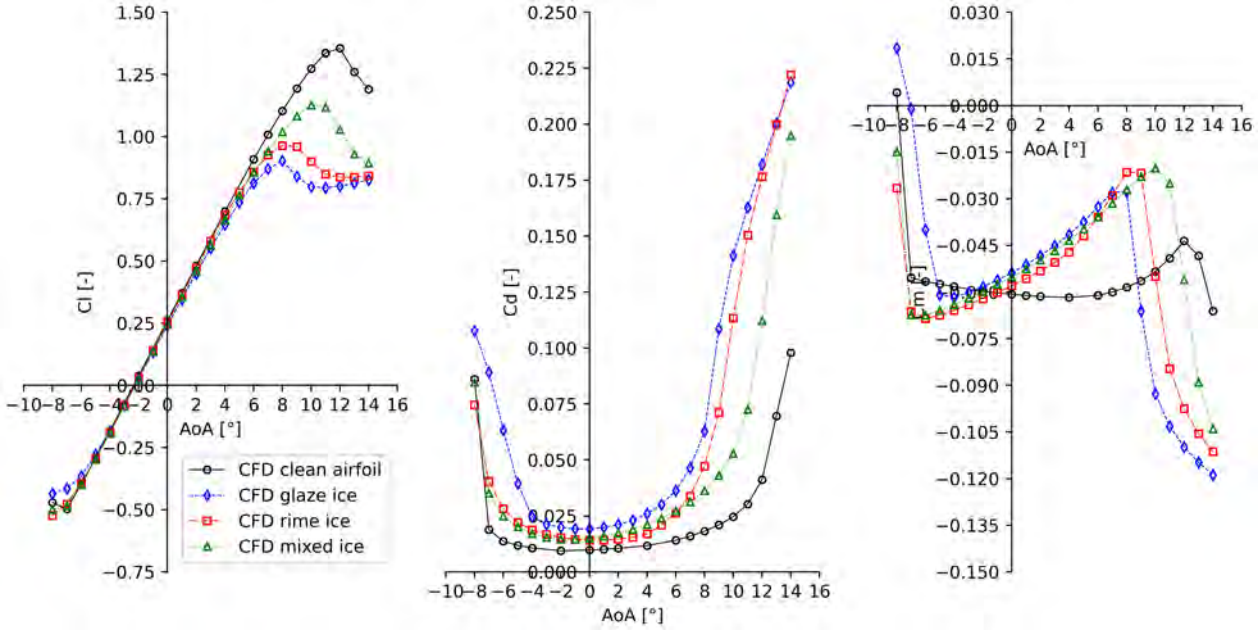

Fig. 3.13.: Plot of c_l over AoA (left), c_d over AoA (mid), c_m over AoA (right) of the FENSAP CFD simulations at Re 750,000.

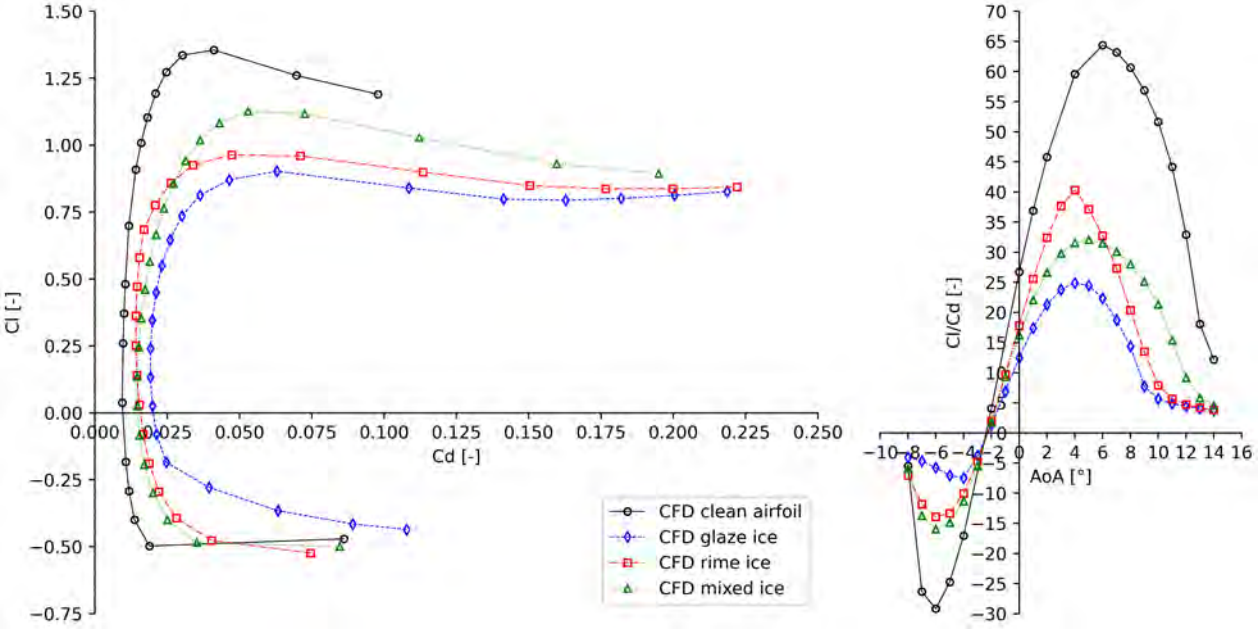

Fig. 3.14.: Plot of the drag polar (left) and the L/D ratio over AoA (right) of the FENSAP CFD simulations at Re 750,000.

Tab. 3.8.: FENSAP CFD simulation aerodynamic penalties predictions for Re 750,000

Case	$\Delta\alpha_{c_{l,max}}$	$\Delta c_{l,max}$	$\Delta\alpha_{c_{d,min}}$	$\Delta c_{d,min}$	$\Delta\alpha_{L/D}$	$\Delta L/D$	$\Delta\partial c_m$
Glaze ice	-4°	-33.4%	+2°	+103.9%	-2°	-61.4%	$+0.170\frac{1}{\text{rad}}$
Rime ice	-4°	-28.9%	+2°	+50.0%	-2°	-37.4%	$+0.159\frac{1}{\text{rad}}$
Mixed ice	-1°	-16.8%	+1°	+54.9%	-1°	-50.2%	$+0.173\frac{1}{\text{rad}}$

Tab. 3.9.: FENSAP CFD simulation reference conditions based on averaged experimental results for Re 750,000.

Case	Re	$v_\infty \left[\frac{m}{s}\right]$	p_s [Pa]
Clean RG-15C	746,450	25.00	101,325
Glaze ice	737,402	25.17	99,405
Rime ice	736,860	25.16	99,407
Mixed ice	752,125	25.32	100,821

3.2.4. Numerical results summary

All ice shapes increased significantly the drag coefficient of the baseline RG-15C at all AoA. However, the lowest minimum drag penalty were induced at a Reynolds number regime of 750,000 and the highest at 200,000 by the simulated artificial ice shapes. On this occasion, glaze ice turned out to be the most severe with increasing the minimum drag coefficient of the baseline RG-15C by +147% at a Reynolds number regime of 200,000 and by +104% at 750,000. Rime ice was the least severe ice shape with inducing a minimum drag penalty of +88% at 200,000 and +50% at 750,000 to the baseline RG-15C airfoil. This seems to stand in contradiction to the experimental campaign, where the analogy was observed that by increasing the Reynolds number regime, the ice-induced minimum drag penalties were also increasing. The FENSAP CFD simulations predicted that glaze and rime ice showed similar stall behaviour and reduced the maximum lift AoA by -4° at the Reynolds number regime of 750,000 and by -1° at 200,000. Mixed ice seemed to less affect the stall behaviour of the RG-15C since it barely reduced the maximum lift AoA by -1° and reduced the $c_{l,max}$ by maximum -12% at the highest Reynolds number regime of 750,000. The maximum L/D ratio remained constant for each ice shape throughout the simulated Reynolds number regimes and was reduced the greatest by the glaze ice shape with around -61% and the least by the rime ice shape with around -40%.

3.3. Pressure coefficients and velocity flow field results

In the following, the pressure coefficient plots of the experimental and numerical campaign are presented alongside with the velocity contour plots of the ANSYS FENSAP module simulations. According to Bragg et al. [13, p. 356], the Reynolds number has a large influence on the flow separation of clean airfoils. This influence is effectively reduced by the dominating ice induced boundary-layer separations [13, p. 356]. This is why, the FENSAP-predicted occurrence of the LSBs and trailing edge separation bubbles at the clean RG-15C as well as the ice-induced boundary-layer flow separation bubbles are displayed for exemplarily AoA in the subsequent subsections.

3.3.1. LSB and trailing edge separation at the clean RG-15C

Characteristics of LSBs on an airfoil at low Reynolds numbers were experimentally investigated by O'Meara and Mueller in 1987 [34]. According to them, the airfoil's performance is likely to be deteriorated by the LSBs. They state furthermore, that pressure plateaus are one indicator for the onset of a LSB. The observed behaviour of LSBs was linked to the in- and decrease of the Reynolds number and AoA: The LSBs were contracted in length by an increase in the Reynolds number and were moving upstream by reaching higher AoA. While the size of the LSB was dependant on the Reynolds number, the LSB remained constant in length when purely the AoA was increased [34].

O'Meara and Mueller correlated this behaviour to the more adverse pressure gradients at higher incidences.

Figure 3.15 shows the CFD simulation results of the velocity flow fields at multiple AoA for the RG-15C at a Reynolds number regime of 200,000. The contour plots for the two higher Reynolds numbers are provided in the Appendix A.7. In the plots, the LSBs and the trailing edge separation bubbles are indicated by green arrows. Both flow separation phenomena occurrences for positive AoA are summarized for the investigated Reynolds number regimes in Table 3.10. The simulation showed similar characteristics of the LSBs as experimentally observed by O'Meara and Mueller: They decreased in size with increasing Reynolds number and slightly moved upstream until the flow was fully separated by increasing the AoA.

The pressure distributions between -4.3°<AoA<4.8° of the CFD simulations were in good coincidence with the experimental retrieved values (see Figure 3.17). A pressure plateau with a follow-up pressure coefficient raise was observed at the AoA=-7.8° on the lower clean airfoil side (LS) at all tested Reynolds numbers (see Figure 3.16 (a)). This indicated a greater extend of the separation bubble than numerically predicted. At the other AoA, no pressure plateau indicator was observed in the experimental c_p-plots (see Figure 3.17) except for the AoA=10.8° case at a Reynolds number regime of 750,000 (see Figure 3.17 (e)). Since the next higher AoA=11.8° c_p-plot shows nothing similar (see Figure 3.17 (f)), it was concluded that the actual AoA of the AoA=10.8° experiment at a Reynolds number regime of 750,000 must have been AoA>12°. This observation is separately treated in the next subsection. It was not surprising that the other experimental c_p-plots in Figure 3.17 (a) - (d) showed no LSB indications, since also the numerically predicted onset of the LSBs was farther upstream of the first pressure tap location. Furthermore, the high uncertainties of the upper airfoil side pressure taps at especially the lower Reynolds number regimes of 200,000 and 400,000 made a statement difficult. The pressure measurement uncertainties are treated separately in section 4.3.

Tab. 3.10.: Flow separation phenomena predictions by the FENSAP CFD simulations for different considered Reynolds number regimes.

Re	Laminar separation bubble near leading edge	Onset of stall / bound separation bubble at trailing edge	Deep stall/ fully separated flow
200,000	AoA>6°; travels upstream and grows in height	AoA>9°; grows in size upstream	AoA>11°
400,000	AoA>7°; travels upstream and grows in height	AoA>10°; grows in size upstream	AoA>12°
750,000	AoA>8°; fixed between 0.004c and 0.007c	AoA>1 1°; grows in size upstream	AoA>13°

The lower airfoil side pressure taps experienced much lower uncertainties, which allowed a comparison of the experiments to the CFD results . The comparison revealed overall more positive c_p on the experimental side. The offset is similar for all positive AoA and the c_p is exceeding in the leading edge region of the lower airfoil side c_p=1. According to the definition of the pressure coefficient for incompressible flows, a c_p=1 yields that the local static pressure is equal to the stagnation pressure of the airflow (see Equation 2.6.8). Consequently, the local static pressure at the airfoil was higher than measured by the pitot probe ahead of the constructed 2D wind tunnel inside the larger L1-B wind tunnel test section. This also implied a higher free stream velocity at the airfoil position.

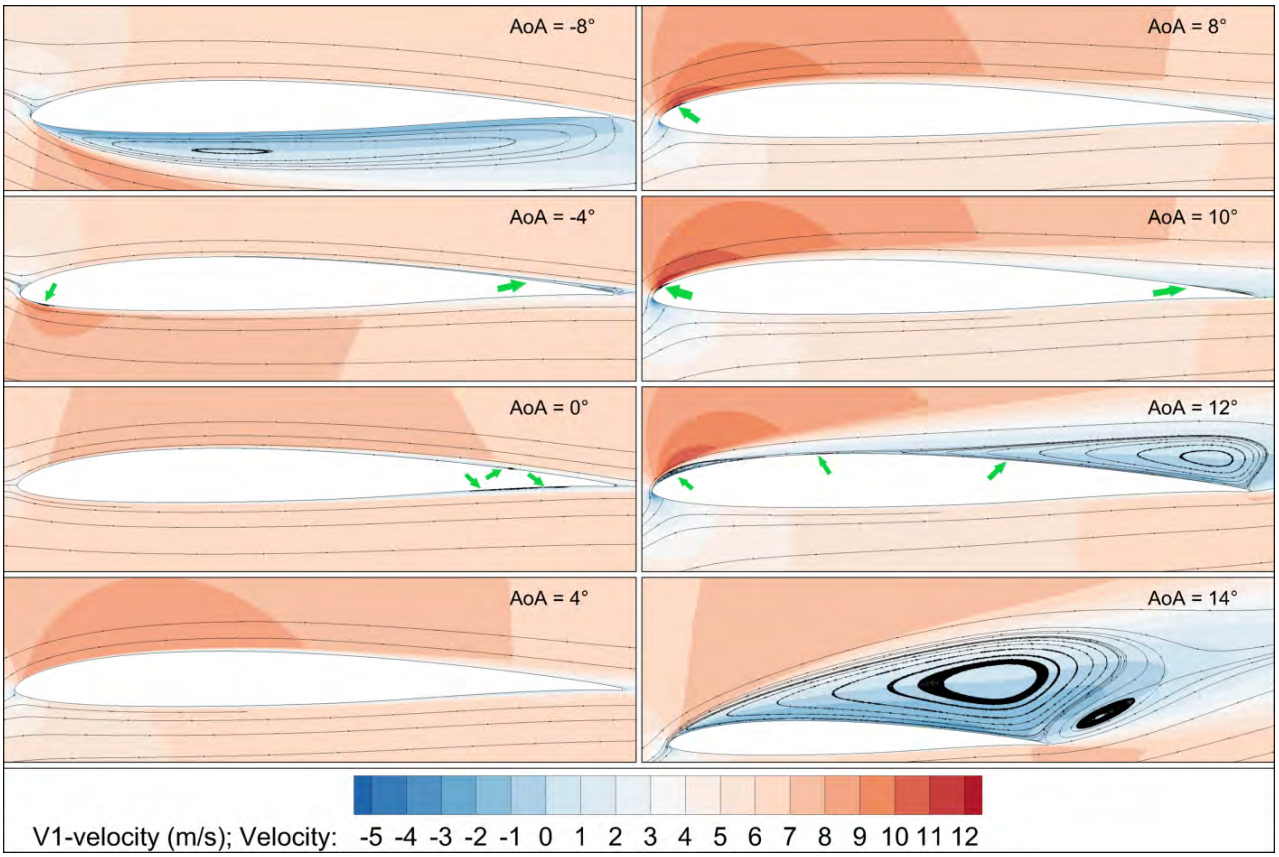

Fig. 3.15.: Velocity contour plot of the RG-15C at different AoA and a Reynolds number regime of 200,000. LSB positions and the onset of bound trailing edge separation are indicated by green arrows.

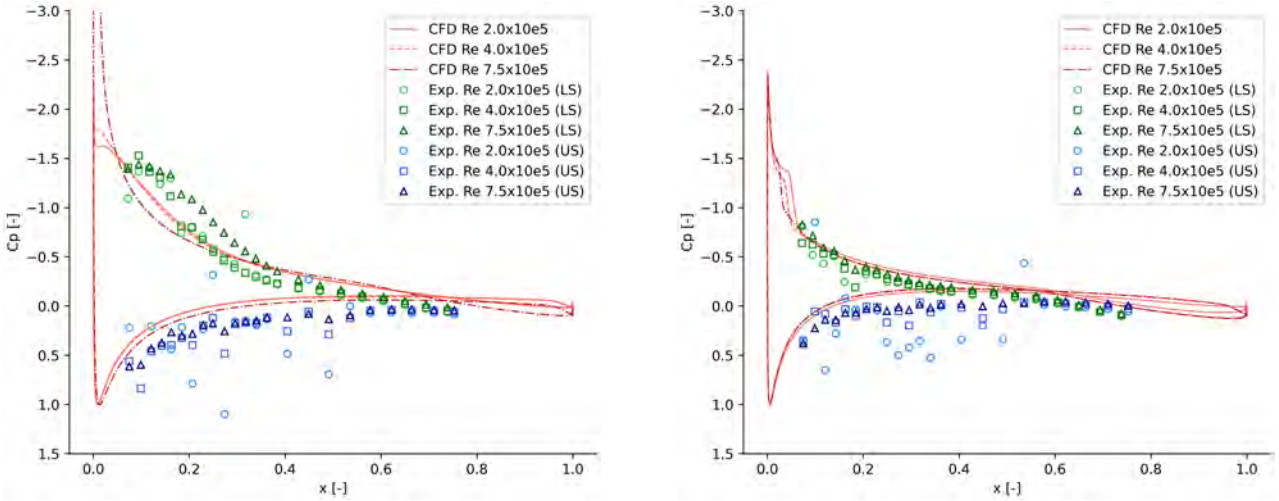

(a) AoA=-7.3° (b) AoA=-4.3°

Fig. 3.16.: Clean airfoil c_p over dimensionless chord location x at two negative AoA. Displayed are each the FENSAP clean RG-15C predictions in red, the experiments' upper airfoil c_p in blue and the experiments' lower airfoil c_p in green colours for all three Reynolds number regimes.

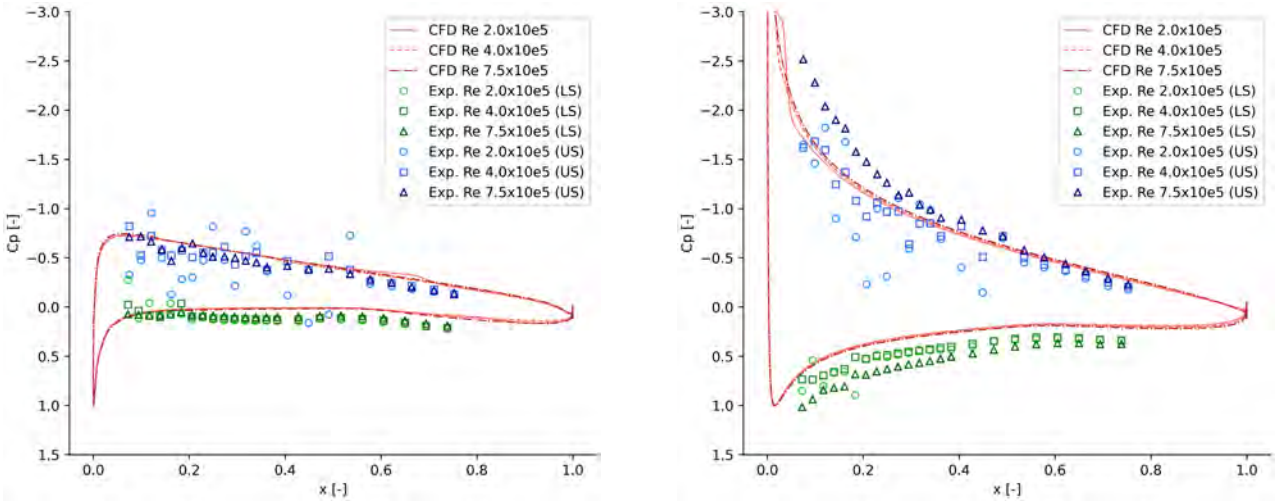

(a) AoA=1.8°

(b) AoA=7.8°

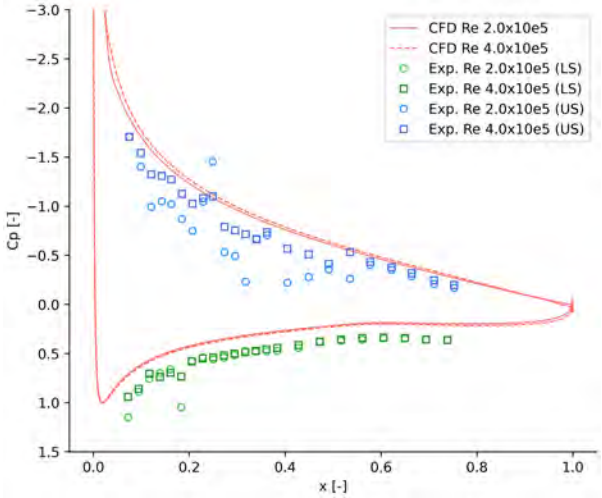

(c) AoA=8.8°

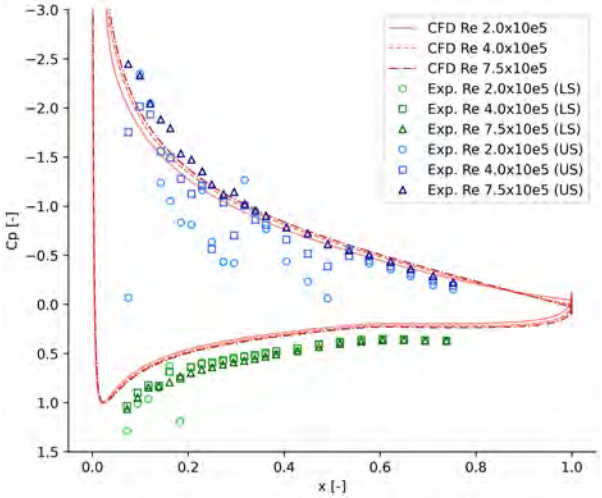

(d) AoA=9.8°

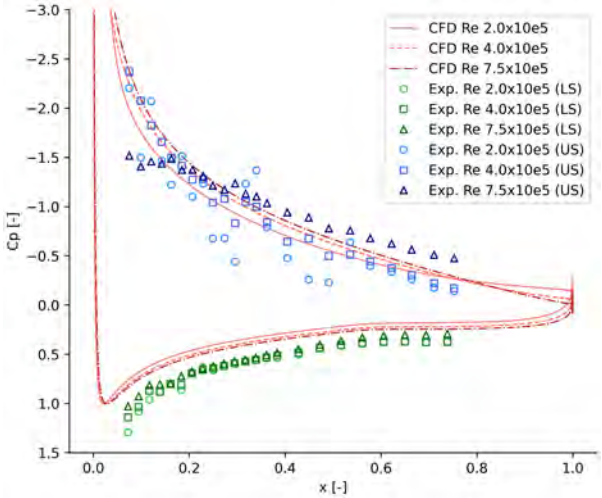

(e) AoA=10.8°

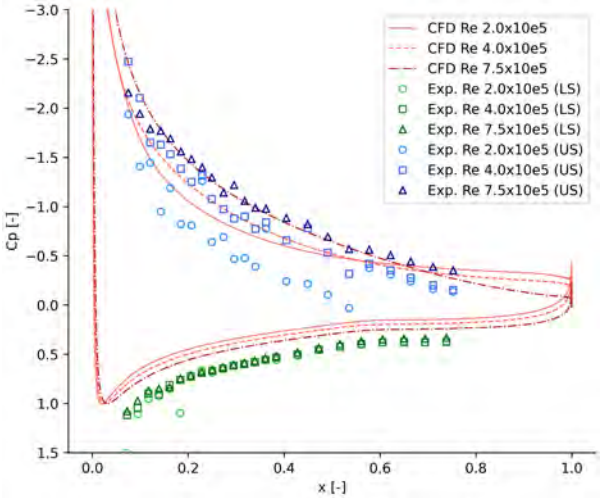

(f) AoA=11.8°

Fig. 3.17.: Clean airfoil c_p over dimensionless chord location x at multiple positive AoA. Displayed are each the FENSAP clean RG-15C predictions in red, the experiments' upper airfoil c_p in blue and the experiments' lower airfoil c_p in green colours for all three Reynolds number regimes.

3.3.2. Clean airfoil experiment AoA correction with c_p-plots at Re=750,000

The previously mentioned unphysical behaviour in the aerodynamic coefficient plots at higher AoA, which was displayed in Figure 3.5 for the clean airfoil experiments at a Reynolds number regime of 750,000, can be correlated to the pressure coefficient plots (b), (d), (e), and (f) in Figure 3.17. In plot (b) at the AoA=7.8°, the experiments shows higher suction pressure levels compared to the CFD simulations. Similar is the case for the lift coefficient at this AoA. This is why an actual higher AoA was suspected to be present in the experiments, which was not high enough for an onset of stall. Therefore the experimental AoA=7.8° case was estimated to be settled around AoA=9.6°, since the pressure plot (d) of Figure 3.17 at AoA=9.8° shows no indication for the onset of stall and similar pressure levels. In contrast, plot (e) of Figure 3.17 reaches a suction pressure plateau between the leading edge and 0.2c at c_p=-1.5. However, this stall indicating plateau is not present at the formally higher AoA plot (f) of Figure 3.17. In plot (f), the experiment and CFD simulation are alike. This encouraged the conclusion that the actual present AoA of the AoA=10.8° case in plot (e) of Figure 3.17 is AoA>12°. An adapted aerodynamic coefficient plot, which displays the corrected and uncorrected aerodynamic coefficients of the clean airfoil measurements at a Reynolds number regime of 750,000, is provided in Figure 3.18.

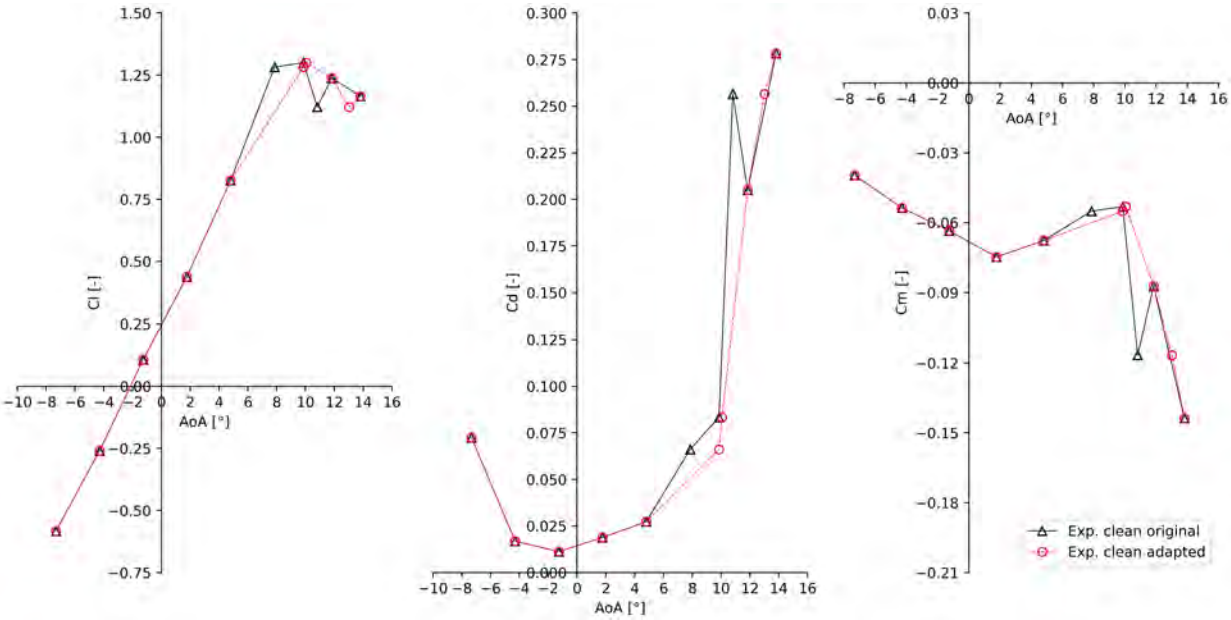

Fig. 3.18.: AoA adaptation of the clean airfoil experiments at Re=750,000. Displayed are c_l (left), c_d (centre) and c_m (right) over AoA of the original experimental results in black and the c_p-adapted experimental results in red.

3.3.3. Glaze ice leading edge flow

Similar to the clean ice experiments, the glaze ice c_p plots were exceeding more positive c_p levels at the lower airfoil side compared to the CFD simulation (see Figure 3.21). This was correlated to the presence of an higher free stream velocity at the airfoil position than measured by the pitot probe ahead of the constructed 2D-wind tunnel inside the L1-B (see Figure 3.21). To make a statement on the upper airfoil side pressure distribution was also difficult due to the high uncertainty levels of the installed *AMS5812 Standard Pressure* sensors ranges at the tested Reynolds number regimes of

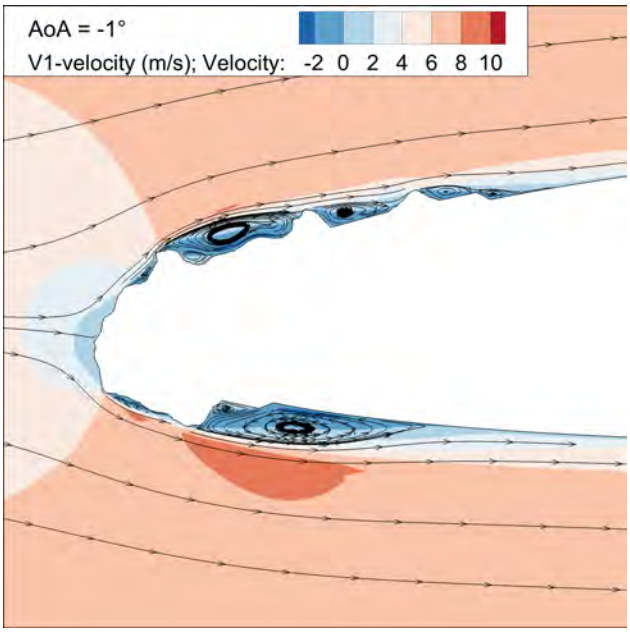

(a) Glaze ice Re=200,000

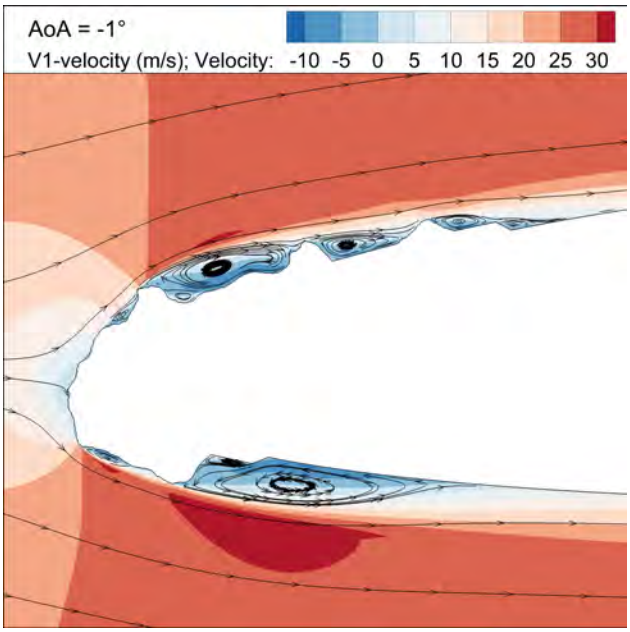

(b) Glaze ice Re=750,000

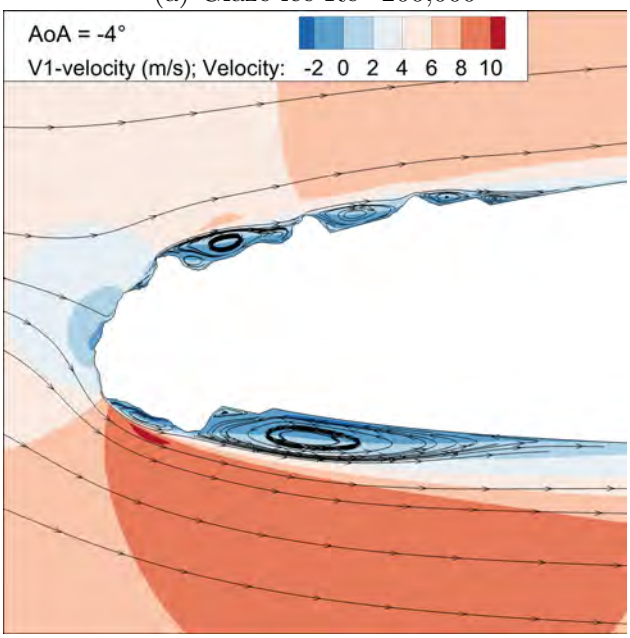

(c) Glaze ice Re=200,000

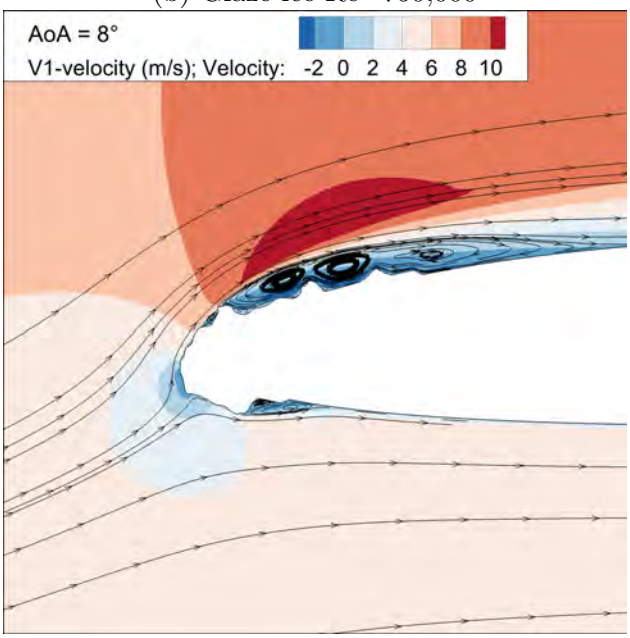

(d) Glaze ice Re=200,000

Fig. 3.19.: Leading edge close up of the glaze iced RG-15C velocity contour plot for selected AoA and Reynolds numbers.

200,000 and 400,000. The c_p distribution of the solely up to a Reynolds number of 750,000 tested AoA=-1.8° case was matched by the CFD prediction quite well (see Figure 3.21 (a)). Figure 3.19 visualizes the ice-induced flow separation bubbles by the artificial glaze ice shape. Their dimensions seemed not to be affected by the change of the Reynolds number to a great extend as the comparison of Figure 3.19 (a) and (b) indicates. Therefore it was not surprising that also the predicted aerodynamic coefficients of the glaze iced RG-15C were barely affected by the change of the Reynolds number regime. However, with increasing AoA, the before separated bubbles in between the three horn

features on the upper airfoil side were combined to one large separation zone with three eddy centres (see Figure 3.19 (d)).

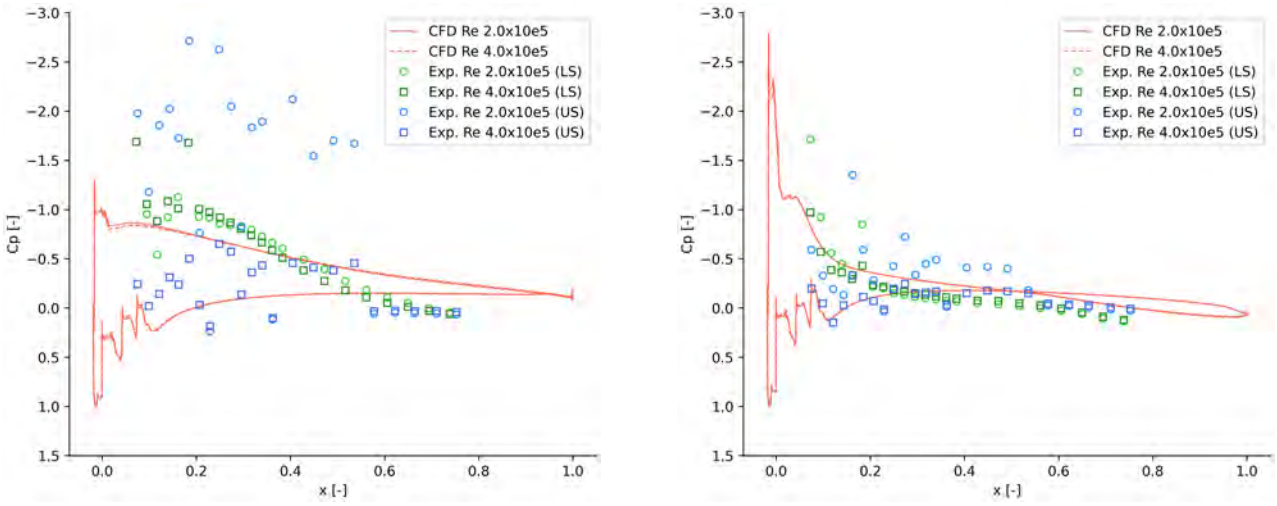

(a) AoA=-7.3° (b) AoA=-4.3°

Fig. 3.20.: Artificial glaze ice case c_p over dimensionless chord location x at two negative AoA. Displayed are each the FENSAP clean RG-15C predictions in red, the experiments' upper airfoil c_p in blue and the experiments' lower airfoil c_p in green colours at the Reynolds number regimes of 200,000 and 400,000.

3.3.4. Rime ice leading edge flow

The relatively streamwise artificial rime ice shape showed similar to the glaze ice case no strong dependency on the tested Reynolds number regimes, since the size of the ice-induced separation bubbles and the aerodynamic coefficients did not vary to a great extend between the Reynolds numbers (see Figure 3.22 (a) and (b), as well as Figure 3.9, Figure 3.11, and Figure 3.13). The tested rime ice shape tapered with 80°, which resulted according to the CFD simulations at higher AoA in a large leading edge bound separation bubble (see Figure 3.22 (c)). The size of the arising separation bubble at higher AoA is comparable to the one at the glaze ice case. This was suspected to be the reason why the onset of stall occurred at equivalent AoA for both ice shapes and the maximum lift penalties were predicted at similar levels (see Table 3.4).

3.3.5. Mixed ice leading edge flow

In contrast to the rime and glaze ice, the artificial mixed ice case was able to maintain isolated separation bubbles at the leading edge even at AoA=10° (see Figure 3.23 (c)). On this occasion, each little horn and bump of the mixed ice topology was causing a small separation bubble to from. Combined with the rounded leading edge it was suspected that this resulted in less deteriorated lift at higher AoA compared to glaze and rime ice (see Table 3.4).

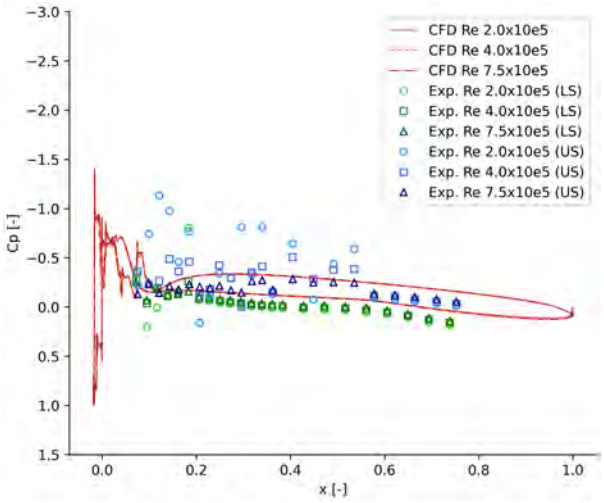

(a) AoA=-1.3°

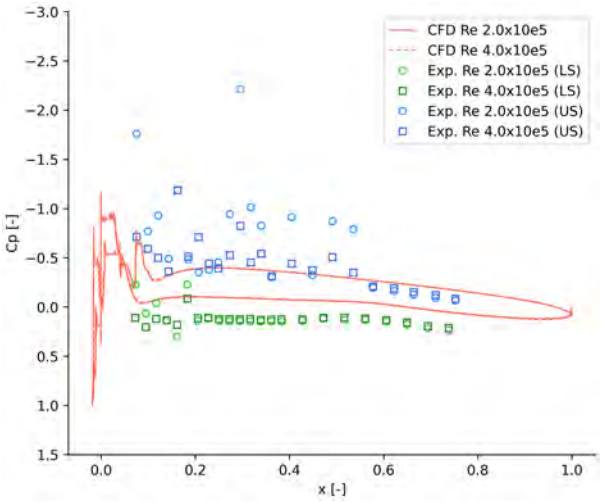

(d) AoA=1.8°

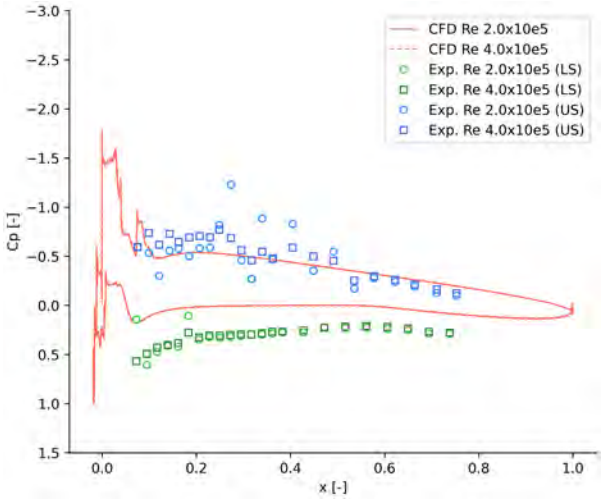

(e) AoA=4.8°

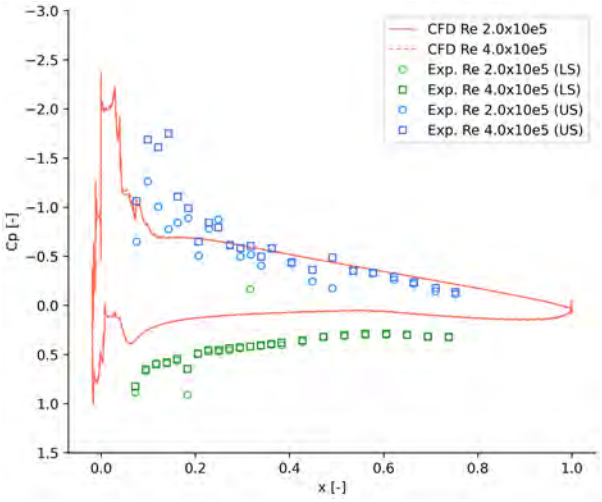

(f) AoA=7.8°

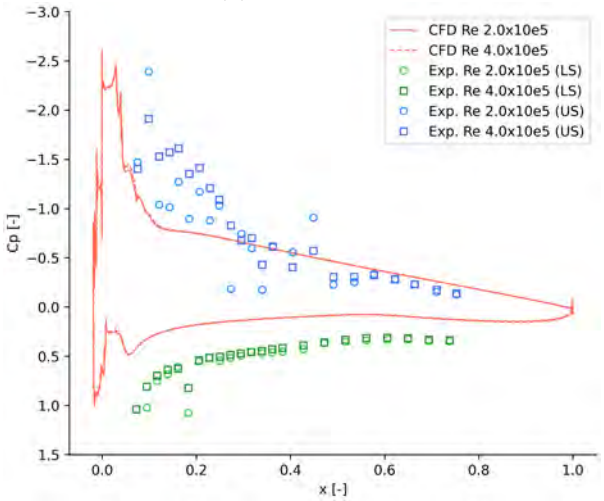

(e) AoA=8.8°

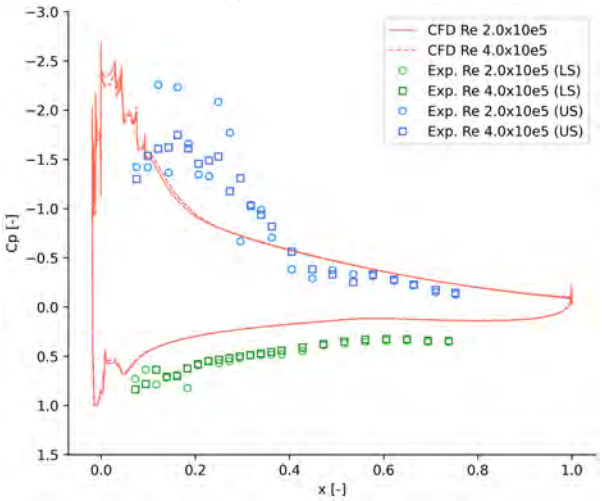

(f) AoA=9.8°

Fig. 3.21.: Artificial glaze ice case c_p over dimensionless chord location x at different AoA. Displayed are each the FENSAP clean RG-15C predictions in red, the experiments' upper airfoil c_p in blue and the experiments' lower airfoil c_p in green colours at the Reynolds number regimes of 200,000 and 400,000.

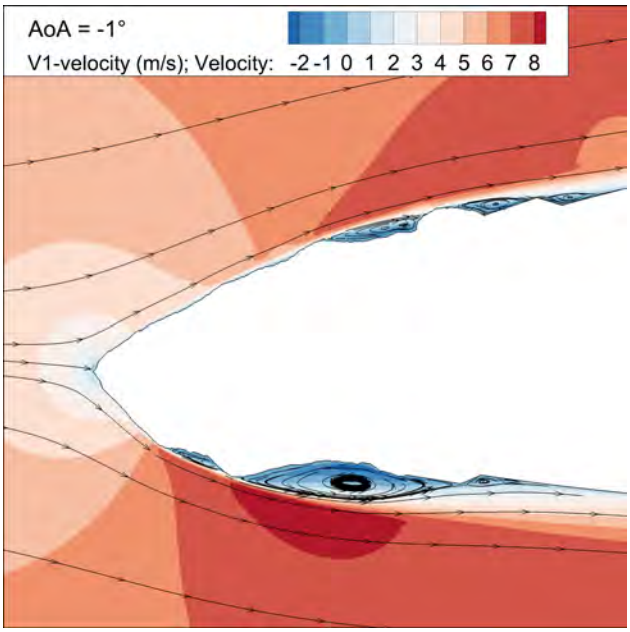

(a) Rime ice Re=200,000

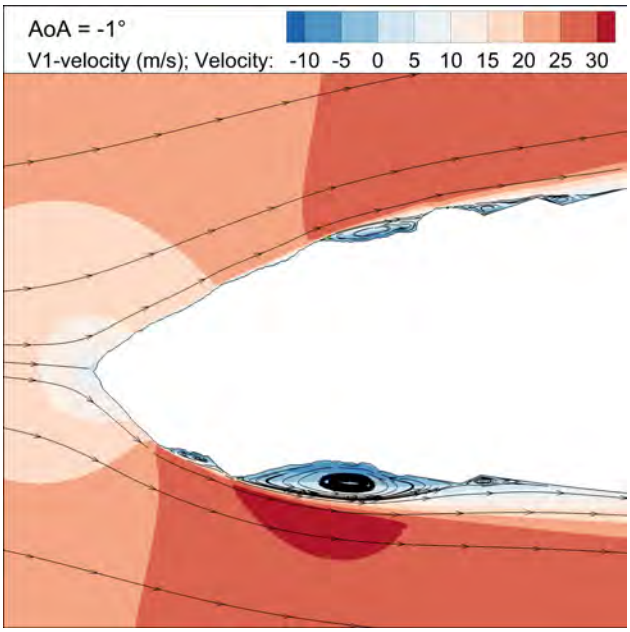

(b) Rime ice Re=750,000

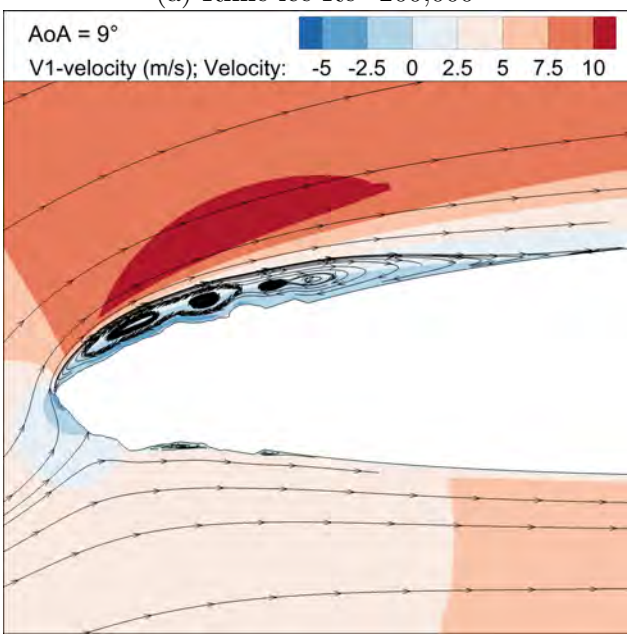

(c) Rime ice Re=200,000

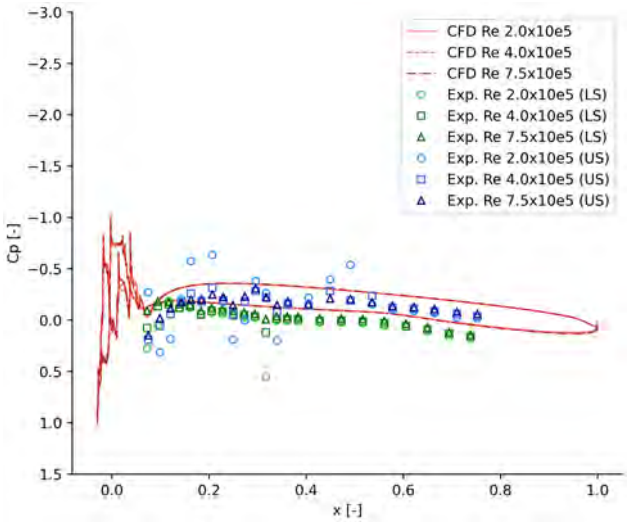

(d) c_p at AoA=-1.3°

Fig. 3.22.: Leading edge close up of the rime iced RG-15C velocity contour plot for selected AoA and Reynolds numbers (a-c). FENSAP and experimental plot of c_p over dimensionless chord location x at AoA=-1.3° and all three Reynolds numbers (d).

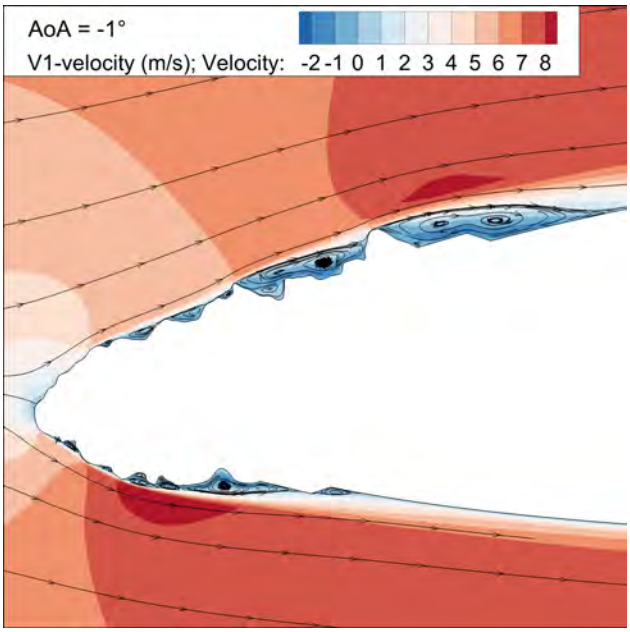

(a) Mixed ice Re=200,000

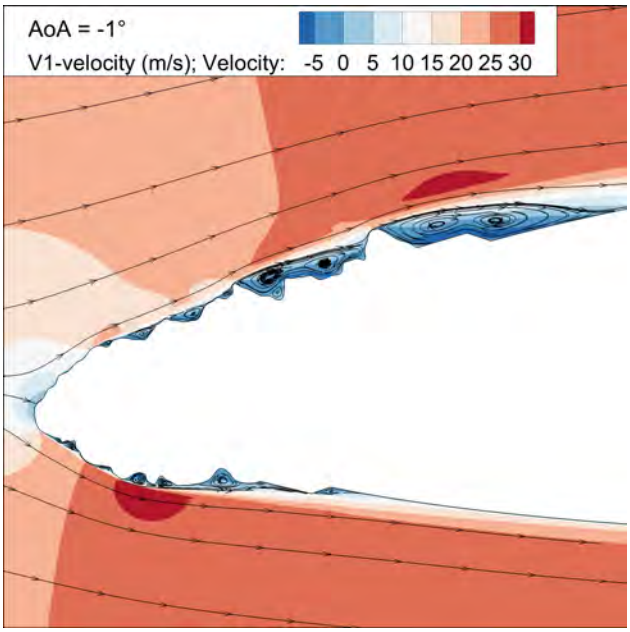

(b) Mixed ice Re=750,000

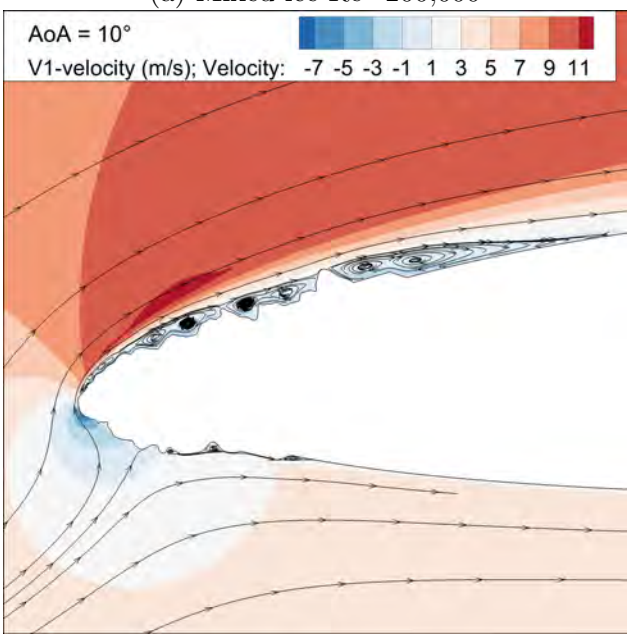

(c) Mixed ice Re=200,000

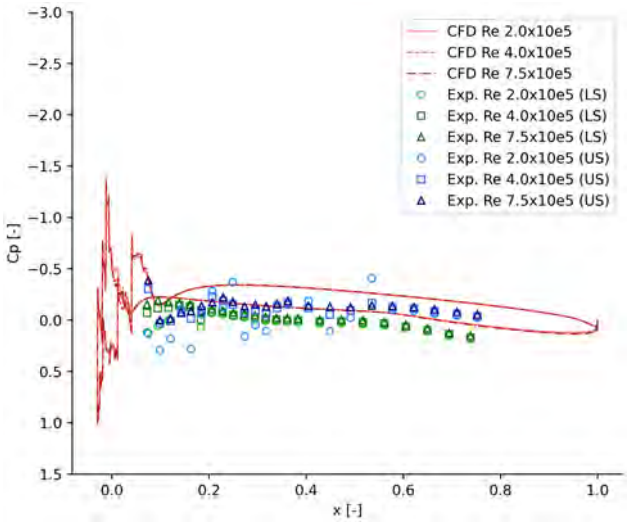

(d) c_p at AoA=-1.3°

Fig. 3.23.: Leading edge close up of the mixed iced RG-15C velocity contour plot for selected AoA and Reynolds numbers (a-c). FENSAP and experimental plot of c_p over dimensionless chord location x at AoA=-1.3° and all three Reynolds numbers (d).

4. Comparison and Discussion

The comparison between the conducted numerical and experimental studies focuses on major aerodynamic coefficient results to enable a conclusion on the validity of the CFD simulations with the ANSYS FENSAP module and the Spalart-Allmaras turbulence model per Reynolds number regime. In the follow-on discussion, the conclusions of the comparisons are summarized and critically evaluated regarding the chosen numerical methodological approach. Furthermore, the experimentally observed high pressure sensor uncertainties, the suspected wing movement, and the non-continuos drag increase of the clean airfoil experiments are addressed and explanations for the observed flow phenomena are provided in the course of the discussion.

4.1. Comparison and validity of the CFD simulations

The experimental and numerical results are compared to each other for each conducted Reynolds number regime. The experimental aerodynamic coefficients of the mixed and rime ice shape cases are compared to linear interpolated FENSAP module predictions at an AoA=-1.3° since ultimately no experimental angular sweep was performed for these two ice shapes. At the end of each subsection, a conclusion on the validity of the FENSAP prediction at the specific Reynolds number is stated. It has to be noted, that according to Bragg et al. [13, p. 356] the Reynolds number has a minor influence on the aerodynamic performance of iced airfoils at manned aviation Reynolds number regimes compared to the Reynolds number influence on the aerodynamic performance of clean airfoils. An evaluation of the Reynolds number influence for the considered one order of magnitude lower Reynolds number regimes of typical medium-sized fixed-wing UAVs is provided subsequent to the Reynolds number specific comparisons.

4.1.1. Comparison and validity of the CFD simulations at Re 200,000

In Figure 4.1, the aerodynamic parameters of the FENSAP CFD simulations are displayed in comparison to the acquired experimental data for the clean airfoil case and the glaze-ice case. The minimum predicted drag levels are 80% lower for the clean RG-15C simulations compared to the experimental clean case. These 80% are equal to 68 drag counts. The experiment shows a non-continuous drag increase for AoA>4.8°, which is not present at the 2D steady state simulations of FENSAP and other experiments on an RG-15 airfoil at equal Reynolds numbers (see Figure 3.8 (right)). Apart from an increased base drag level, the experimental drag coefficient and the FENSAP drag coefficients are alike for AoA≤4.8°. The experiments are showing an 14% higher $c_{l,max}$ for the clean airfoil case and the onset of stall is 2° later compared to the clean RG-15C simulation prediction. Nevertheless, the slope of both lift coefficients are alike. Summarised in the L/D ratio plot, the CFD simulation over-predicts the L/D_{max} of the experiments by 29% at a similar AoA. This was ascribable to the increased base drag level of the experiments, since the lift coefficients of the experiment and simulation were alike.

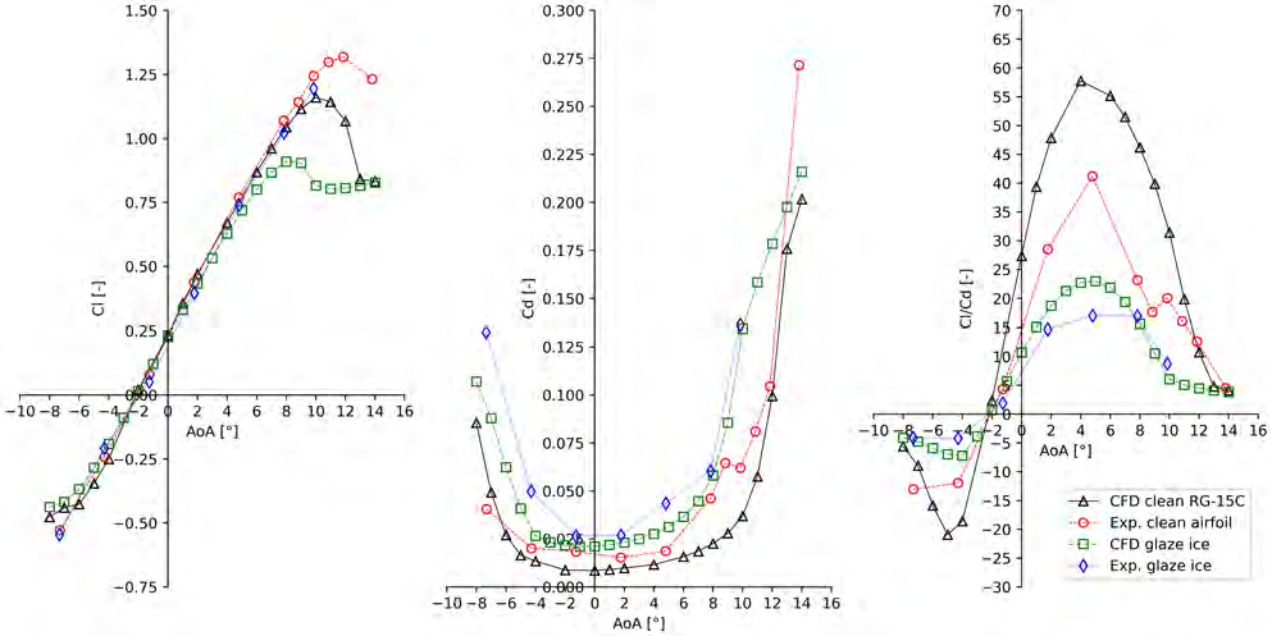

Fig. 4.1.: Clean and glaze ice case comparison at Re=200,000 of c_l (left), c_d (centre) and L/D (right) over AoA of the FENSAP prediction and the experimental results.

By comparing the numerical and experimental results regarding the ice shapes, glaze ice stands out in both cases as the most severe regarding the ice shape induced aerodynamic penalties at a Reynolds number of 200,000. The glaze ice experiments were not conducted until the onset off stall. However, the CFD simulations shows a clear deficit in predicting the onset off stall: While the glaze ice simulation is stalling at AoA=9°, the experimental glaze ice shows no stall behaviour at an AoA=9.8° and records at the same AoA a 32% higher lift coefficient. For lower AoA, the general slopes of the lift coefficients are alike for both glaze ice cases. The minimum drag levels fairly match at the same AoA=-1°, but FENSAP under-predicts the $c_{d,min}$ of the glaze ice experiment by 25%. The CFD glaze ice simulation over-predicts the maximum L/D ratio of the experiment by 25%. Nevertheless, the maximum L/D ratio is reached for both cases at similar AoA=4°.

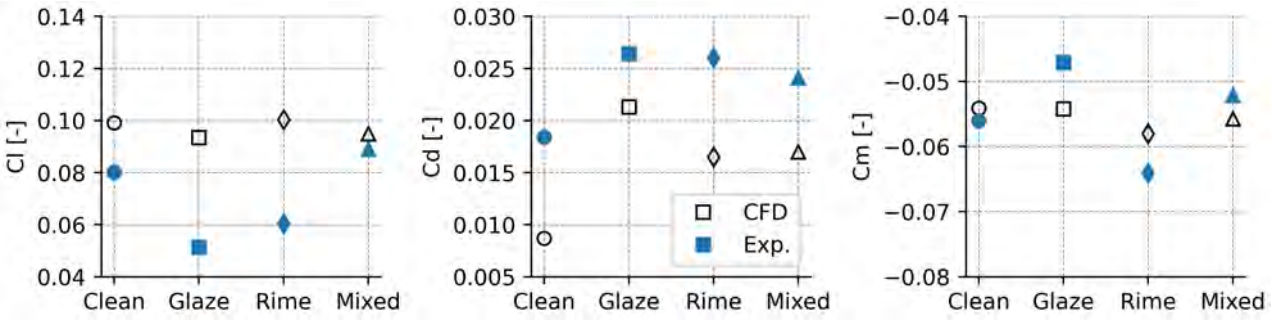

Fig. 4.2.: Aerodynamic parameters c_l (left), c_d (centre), and c_m (right) at a Reynolds number of 200,000 displayed at an AoA=-1.3° for the experiments (blue) and the FENSAP CFD simulations (black).

The other ice shapes were only tested at the AoA=-1.3°. A direct comparison of the glaze, rime, and mixed ice aerodynamic parameters at an AoA=-1.3° is displayed for the experiments (blue) and CFD simulations (black) in Figure 4.2. Near the AoA=-1.3°, the experiments and simulations are deviating especially regarding the lift and drag coefficients. While the mixed ice c_l is fairly

matched, the experiments shows up to 82% lesser c_l for the glaze ice compared to the simulations. The experiments are showing an ice shape dependant $\Delta c_{l,-1.3}$ penalty, whereas the lift levels of the simulated RG-15C are barely affected by the different ice shapes. The opposite is the case for the drag penalties: herein all experimental ice shapes induced a similar $\Delta c_{d,-1.3}$ of around 40% onto the clean airfoil while the simulations are emphasizing the glaze ice. The deviation in the predicted drag coefficient is the greatest for the rime ice with -36%. Besides that, the moment coefficients are alike with a maximum deviation of 15% for the glaze ice case.

In summary the clean RG-15C numerical simulations at a Reynolds number of 200,000 were adequately capturing the available literature data expect the onset of stall. Similar behaviour was observed for the glaze ice simulations regarding the onset of stall in comparison to the wind tunnel measurements. Especially the $c_{l,max}$ penalty was more severe in the FENSAP simulations. The experimental ice shape cases' lift coefficients were over-predicted for the glaze and rime ice by the chosen CFD approach at an AoA=-1.3°. At the same AoA, the drag coefficients were predicted with limitations. The drag coefficient penalties of the experimental glaze ice were higher as the more conservative FENSAP predictions, but in general captured. This yields that FENSAP was able to reasonably predict the drag increase from glaze ice, but was limited at predicting the onset of stall with the chosen Spalart Allmaras turbulence model and the assumption of an instantaneous tripping airflow.

4.1.2. Comparison and validity of the CFD simulations at Re 400,000

In Figure 4.3 the numerical and experimental retrieved lift and drag coefficients are displayed for the clean airfoil and the artificial glaze iced airfoil at the Reynolds number regime of 400,000. The experimental clean airfoil shows a 9% higher $c_{l,max}$ at an 1° higher $\alpha_{c_{l,max}}$ of 11.9° compared to the FENSAP CFD simulation. The onset off stall for the glaze ice case is not captured by the FENSAP simulation: The predicted glaze ice stall occurs at AoA=8°, while stall conditions were not achieved for the experimental glaze ice case at the highest tested AoA=9.9°. Furthermore, the experimental reached $c_{l,max}$ of the glaze ice is 31% higher than numerically predicted. Nevertheless, the slopes of the lift coefficients are alike for the clean and glaze ice cases. The non-continuous drag increase of the clean airfoil experiments at AoA>4.8° is not present at the FENSAP simulations. Between -4.3°<AoA<4.8° the experiments shows a 60% higher base drag level for the clean airfoil, which equals at $c_{d,min}$ 50 drag counts. In the numerical simulations, the aerodynamic drag increase induced by the glaze ice shape is under-predicted by 25% and the absolute $c_{d,min}$ deviation of 50 drag counts is equal to the clean airfoil case. Overall, the propagation of the drag coefficient is fairly matching for the glaze ice, especially at the higher AoA>8°. Motivated by the differences in the drag levels, the L/D ratios are over-predicted by the FENSAP simulations with up to 44% at the clean airfoil case, but show good agreement in the maximum L/D ratio AoA (see Figure 4.3 (right)).

The inclusion of the rime and mixed ice shape to the comparison and validity evaluation of the FENSAP simulations is limited to the AoA=-1.3°, since no further AoA were tested for these ice shapes throughout the experimental campaign. Figure 4.4 summarizes the deviations of the aerodynamic parameters between the CFD prediction and the experimental determination. Herein, the lift coefficient shows a good agreement for the clean and mixed iced airfoil, whereas the lift coefficients of the glaze and rime ice are over-predicted by 80%. FENSAP ice shows no significant lift coefficient penalty for any of the ice shapes onto the clean airfoil with $\Delta c_{l,-1.3}$=-4%...-10%, which is not the case on the experimental side for glaze and rime ice with $\Delta c_{l,-1.3}$=-50%. Although the drag coefficients of the clean, glaze, and rime ice case are under-predicted by around 50 drag counts by the FENSAP

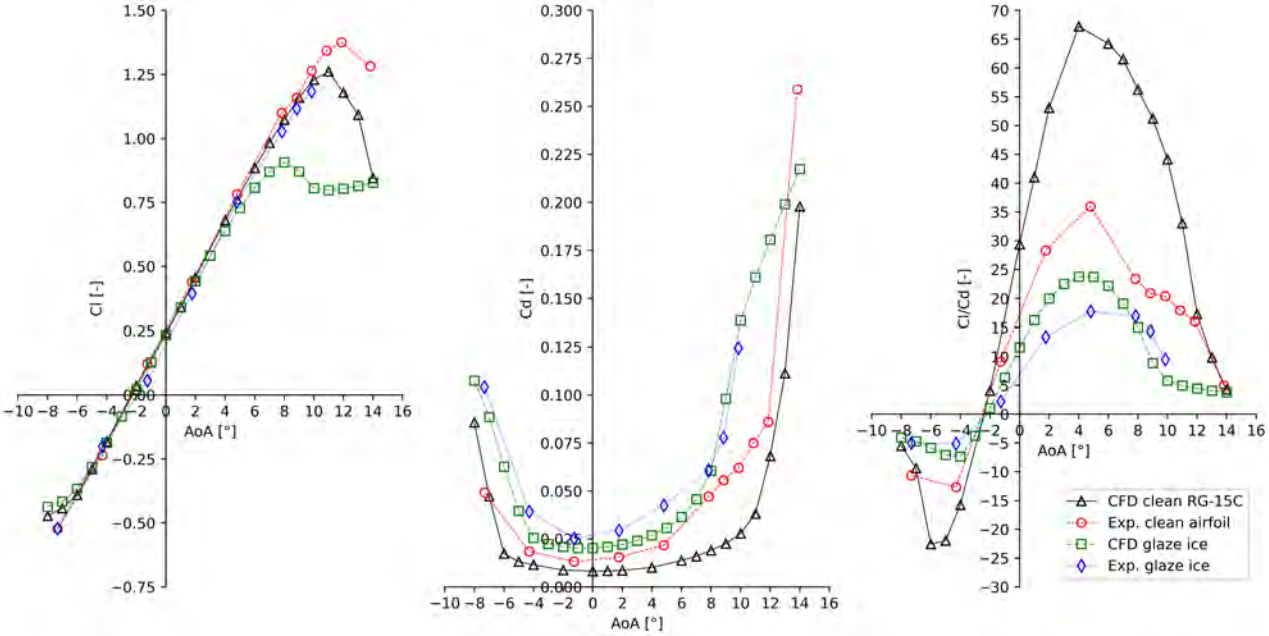

Fig. 4.3.: Clean and glaze ice case comparison at Re=400,000 of c_l (left), c_d (centre) and L/D (right) over AoA of the FENSAP prediction and the experimental results.

simulations, the induced penalty tendency is captured. This is not the case for the mixed ice, which induces in the experiments the highest $\Delta c_{d,-1.3}$ penalty. Regarding the experimental and numerical moment coefficients, the glaze and rime ice cases are alike, while the clean and mixed ice cases records 16% lower values at the CFD simulations.

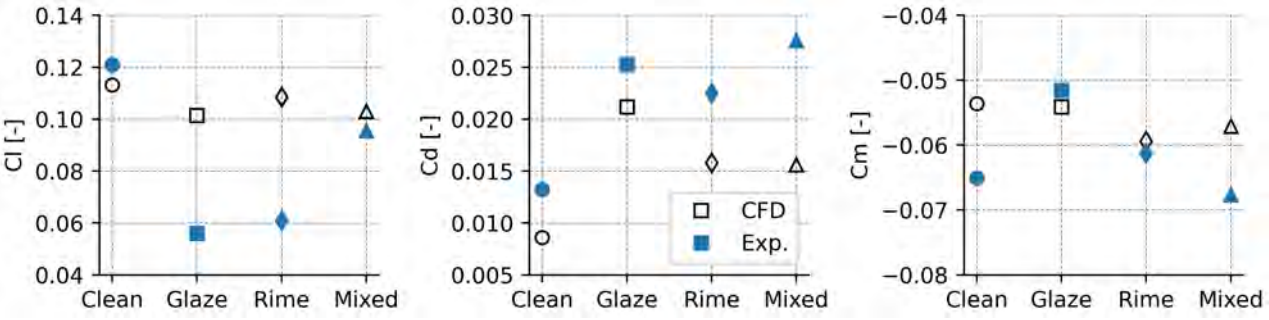

Fig. 4.4.: Aerodynamic parameters c_l (left), c_d (centre), and c_m (right) at a Reynolds number of 400,000 displayed at an AoA=-1.3° for the experiments (blue) and the FENSAP CFD simulations (black).

The comparison of the experimental retrieved aerodynamic coefficients to the chosen FENSAP simulation approach showed that FENSAP was not able to sufficiently predict the onset off stall and the maximum lift coefficient penalty of the glaze ice shape. A detailed look at the AoA=-1.3° revealed limitations of the FENSAP module and the chosen Spalart Allmaras turbulence model to adequately simulate the aerodynamic coefficients of the artificial ice shapes at a Reynolds number regime of 400,000. The deficits were especially high at the over-predicted lift coefficients of the glaze and rime ice, as well as at the under-predicted drag and moment coefficient of the mixed ice. However, the drag coefficient propagation and moment coefficient penalty of the experimental glaze ice shape was reasonably predicted.

4.1.3. Comparison and validity of the CFD simulations at Re 750,000

In Figure 4.5 the experimental and numerical retrieved aerodynamic coefficients of the clean airfoil cases are displayed. A comparison of the experiments and simulations is restricted to -8°<AoA<5° due to the occurrence of unphysical behaviour at the higher AoA measurements. Both are agreeing on the AoA of the minimum drag coefficient and on the AoA of the highest L/D ratio. The slopes of the lift coefficient curve are also alike in the considered AoA region. The minimum drag coefficient is barely under-predicted by FENSAP with a difference of -19% to the experiments, which equals 18 drag counts. However, the slope of the linear moment coefficient region is more negative in the experiments and the maximum L/D ratio is over-predicted by +53%.

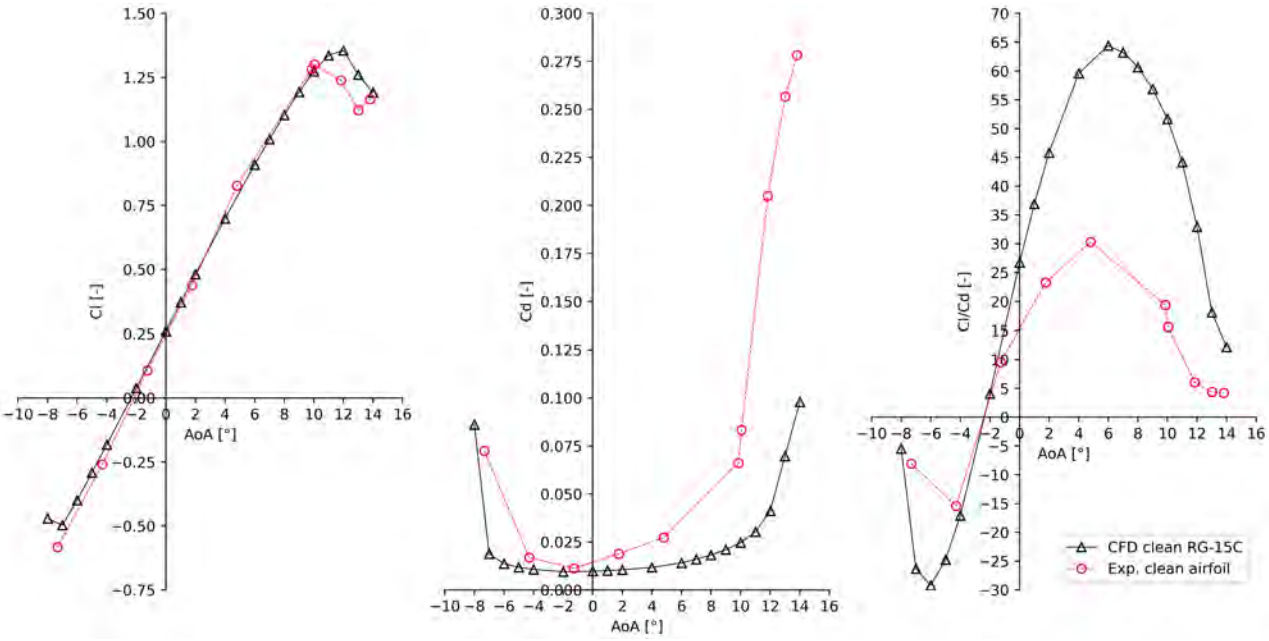

Fig. 4.5.: Clean case comparison at Re=750,000 of c_l (left), c_d (centre) and L/D (right) over AoA of the FENSAP prediction (black) and the experimental results (red).

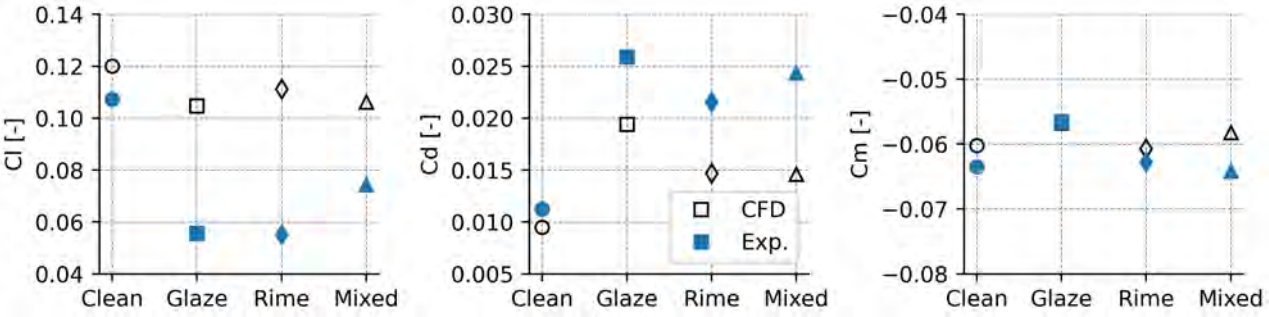

Fig. 4.6.: Aerodynamic parameters c_l (left), c_d (centre), and c_m (right) at a Reynolds number of 750,000 displayed at an AoA=-1.3° for the experiments (blue) and the FENSAP CFD simulations (black).

At the specific AoA=-1.3°, a comparison between the simulated and tested artificial ice shapes is shown in Figure 4.6. Herein, the predicted moment coefficient shows a good agreement with the experimental retrieved ones. Although the drag coefficient is fairly matching at the clean airfoil case, the experimental ice shape drag coefficients are generally under-predicted by -25% in the glaze ice case and up to -40% in the mixed ice case, which equals -60 to -100 drag counts. Similar is observable

for the lift coefficient, which is especially over-predicted in the FESNAP CFD simulations for rime ice by +102%.

In conclusion, the ANSYS FENSAP module CFD simulations were reasonably able to predict the clean airfoil experiments between the considered -8°<AoA<5°. Due to the lack of resilient data at higher AoA, no statement could be made regarding the onset of stall. The FENSAP module in combination with the one-equation Spalart Allmaras turbulence model was able to adequately capture the moment coefficients of the three different ice shapes but showed limitations in the drag and especially lift coefficient predictions.

4.1.4. Influence of the Reynolds number

Figure 4.7 displays the experimental results of the artificial glaze iced and clean RG-15 aerodynamic coefficients at multiple Reynolds number regimes. The displayed results of the glaze ice show no significant deviations of the drag polars between the Reynolds number regime of 200,000 and 400,000 at positive AoA (see Figure 4.7 (left)). A difference between the aerodynamic performance of the glaze ice shape at the Reynolds number regime of 200,000 and 400,000 is observable for the negative AoA especially at the moment coefficient over AoA plot (see Figure 4.7 (right)): At the Reynolds number of 200,000 and negative AoA, the artificial glaze ice induced higher drag penalties and a more negative moment coefficient. The comparison of the glaze ice experimental aerodynamic

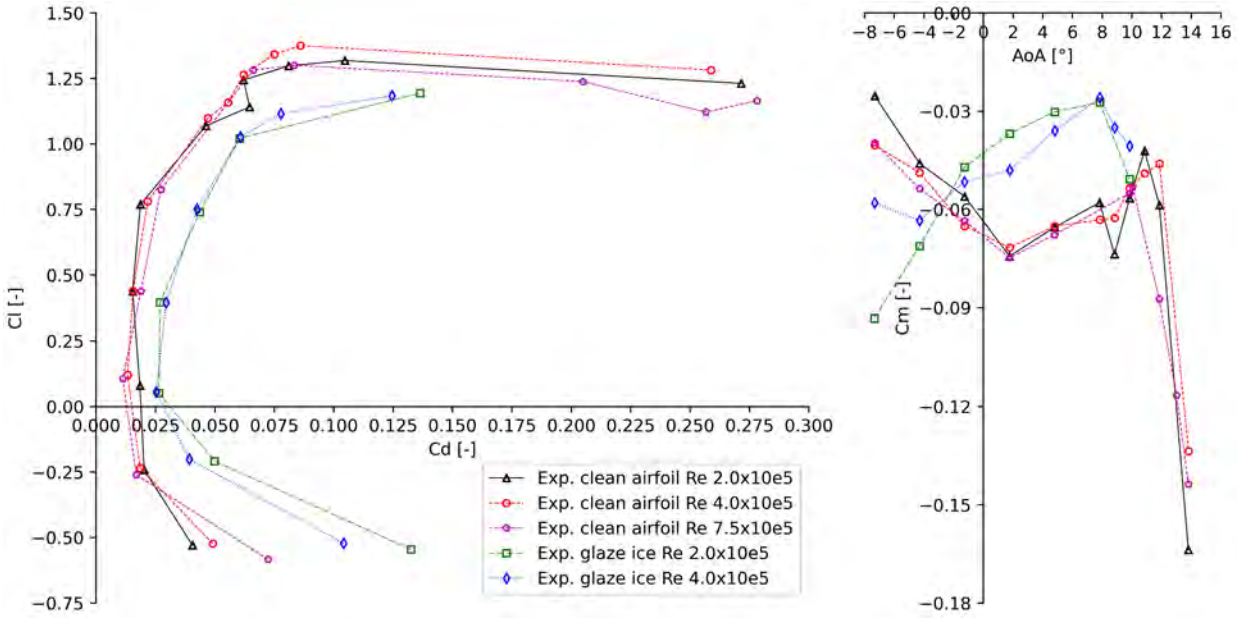

Fig. 4.7.: Comparison of the experimental aerodynamic coefficient results at multiple Reynolds number regimes with c_l over c_d (left) and c_m over AoA (right). The plots indicate a minor influence of the Reynolds number on the aerodynamic performance of the artificial glaze iced and clean RG-15 at positive AoA.

performance regarding the influence of the Reynolds number showed, that the iced airfoil Reynolds number effect evaluation of Bragg et al. [13, p. 356] seems to be also applicable on the tested one order of magnitude lower Reynolds number regimes for positive AoA. Bragg et al. stated a minor influence of the Reynolds number on the aerodynamic performance of iced airfoils, since the boundary-layer separation is dominated by the ice shape topology and location and less dependant on the Reynolds number as it is the case for clean airfoils [13, p. 356].

4.2. Limitations of the Spalart-Allmaras turbulence model at low Reynolds numbers

The analysis of the aerodynamic penalties and comparison of the experimental and numerical results revealed the limitations of the ANSYS FENSAP module and the chosen Spalart-Almaras turbulence model. These were partly situated in the prediction of the maximum lift and stall behaviour of the clean airfoil, which was in general more conservative at the Reynolds number regimes of 200,000 and 400,000. However, the experimentally observed minor effect of the Reynolds number regime on the aerodynamic performance of the glaze iced RG-15 at positive AoA was captured by the CFD simulations. The predicted drag coefficient was in good agreement with literature data at the Reynolds number of 200,000, but showed severe discrepancies by generally under-predicting the conducted experiments.

Chung and Addy [15] evaluated amongst other things the performance of different turbulence models in numerical iced airfoil simulations like the Spalart-Allmaras turbulence model. Therefore, they conducted aerodynamic performance experiments of an horn-iced and streamwise iced NLF-0414 airfoil at a manned aviation Reynolds number of 6.4 million and compared the results to numerical simulations. Chung and Addy concluded, that the Spalart-Allmaras turbulence model was the best to capture the aerodynamic performance of the horn-iced NLF-0414, whereas the Shear Stress Turbulence model was the best to capture the aerodynamic performance of the streamwise iced NLF-0414. They addressed also a relatively poor agreement of the pressure distribution after the horn-ice shape between the experiments and the numerical simulations with the Spalart-Allmaras turbulence model. Similar was observed throughout the comparison of the previous section and in section 3.3.

While the overall drag penalties introduced by the glaze ice shape were fairly captured by the FENSAP simulations for the Reynolds numbers of 200,000 and 400,000, the simulations and experiments disagreed in the onset of stall and maximum achievable lift prediction. The c_p plots of the glaze ice shape revealed an under-prediction of the suction pressure levels after the end of the ice shape geometry at higher AoA: The maximum lift was therefore under-predicted and the onset of stall occurred 2° earlier in the simulations than the highest tested AoA. The evaluation at the specific AoA=-1.3° pointed out further limitations regarding the lift and drag predictions of the iced RG-15C airfoil at all investigated Reynolds number regimes: While the lift coefficient of the clean RG-15C was barely affected by the simulated ice shapes, the baseline lift coefficient of the experiments was affected by the ice shapes and the extend of the lift penalty was dependant on the ice shape type. On the one hand side, the over-prediction of the lift coefficient was especially present at the glaze and rime ice case, but on the other hand side, FENSAP was able to capture the tendency of the induced drag penalties by these two ice shapes. However, the opposite was the case for the mixed ice case: The drag coefficient was severely under-predicted, while the lift coefficient was alike except for the Reynolds number regime of 750,000. This seemingly inconsistent and limited prediction behaviour was suspected to be caused by the chosen turbulence model.

The Spalart-Allmaras turbulence model was originally designed for wing airflows with a risk for the onset of stall [44, p. 147] and calibrated with flat-plate boundary layers [12]. According to Schwarze [44, p. 147], the one-equation turbulence model is rather inadequate for the modulation of complex, more generalized airflows. It is most likely, that the computation time saving approach to not fully resolve the near wall viscous sub-layers by the high Reynolds number turbulence model like the Spalart-Allmaras and describe them instead with a wall function causes the observed limitations at the simulated low Reynolds number regimes. Schwarze [44, p. 152] mentions on this topic that especially highly 3D flow fields with upstream and tangential directed pressure gradients are

problematic for the approach to use a high Reynolds number turbulence model with a wall function for simulating low Reynolds number flow fields. This type of turbulent 3D flow field was suspected to be present during the ice shape experiments, since the contour plots of the steady state 2D simulations showed already large separation bubbles induced by the ice shapes.

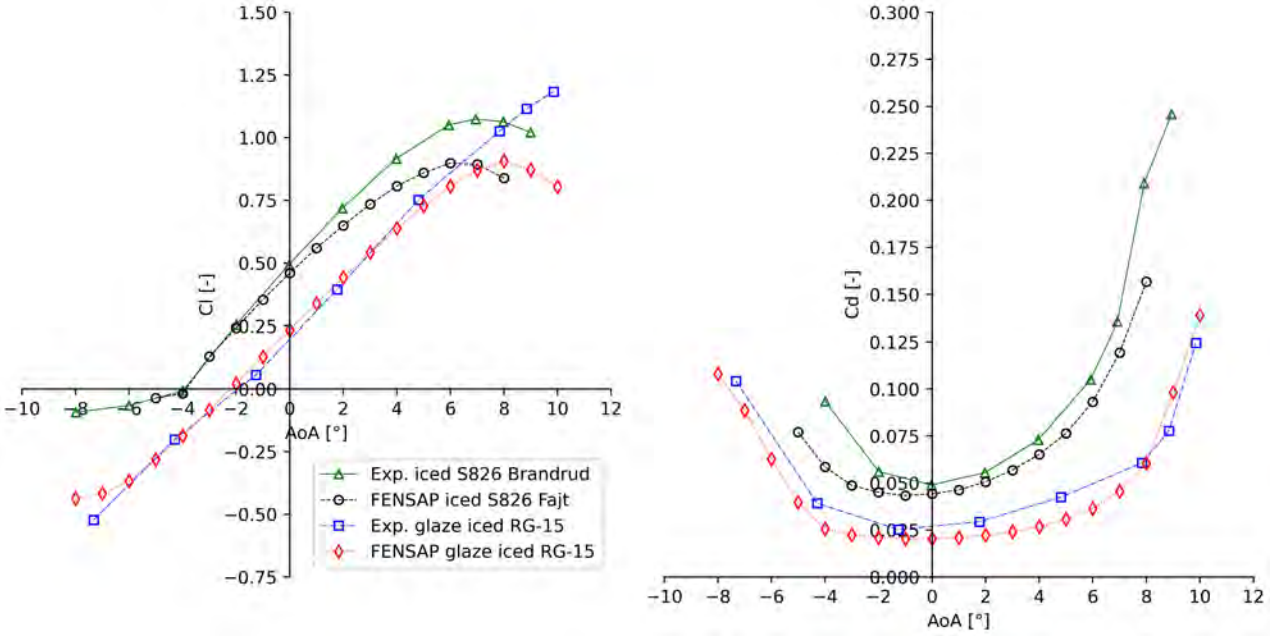

Fig. 4.8.: Comparison of the FENSAP CFD simulation approach with the Spalart-Allmaras turbulence model by Fajt [20] (black) and an iced S826 NREL airfoil [14] (green) with this thesis experimental glaze ice case (blue) and glaze iced RG-15C FENSAP CFD simulation (red). Each displayed data was retrieved at a Reynolds number regime of 400,000.

Another reason why the Spalart-Allmaras turbulence model might have caused the observed inconsistent and limited prediction behaviour for the iced RG-15C cases was inferable from the grid dependency study of Fajt [20] on his ice performance grid. As mentioned in section 2.8, his grid generation approach was adapted in the course of this thesis, since he assumed during his ice performance grid validation that the Spalart-Allmaras model is reasonably capable of capturing ice shapes without severe horn features. Figure 4.8 displays Fajt's chosen experimental validation reference case in comparison to the glaze ice experiments and simulation. All tests and FENSAP simulations were conducted at a Reynolds number regime of 400,000. Fajt's experimental reference case was an horn iced S826 NREL airfoil conducted at the NTNU by Brandrud and Krøgenes [14] (see Figure 4.9). The CFD modelling of Fajt and this thesis is similar and utilizes each the Spalart-Allmaras turbulence model. A comparison of the respective experiments and simulations yielded that both FENSAP simulations were limited in reasonably predicting the achievable lift levels and onset off stall. The drag coefficients were fairly matching, but in general under-predicted. Consequently, the Spalart-Allmaras turbulence model seems also to be limited applicable for estimating the aerodynamic penalties of less pronounced horn ice featured ice topologies at low Reynolds number regimes. This is why it was concluded, that higher order turbulence models, such as Reynolds stress and non-linear eddy viscosity models, might be more suitable for predicting the ice-induced aerodynamic penalties of typical UAV airfoils at low Reynolds number regimes. Readdressing Chang and Addy's [15] studies on numerical predictions of an iced NLF-0414, they also suggested further investigations on turbulence models, which are the best performing ones for different ice shapes.

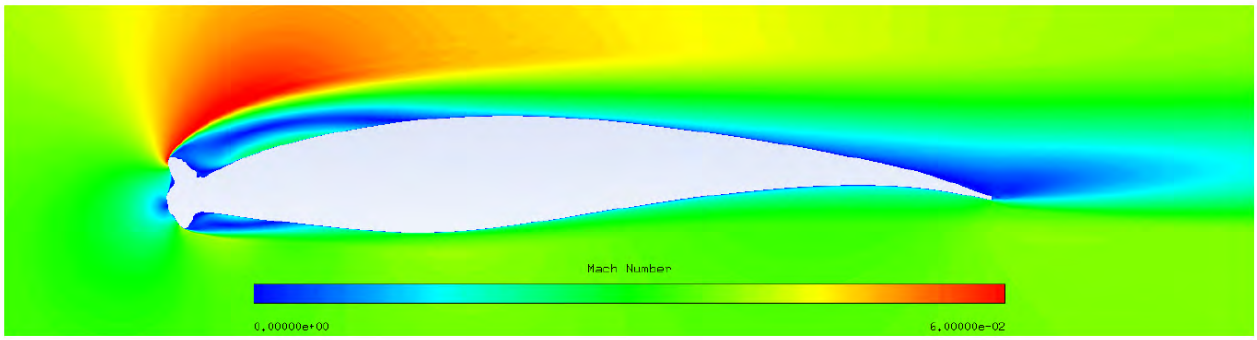

Fig. 4.9.: Mach contour plot of the iced S826 NREL airfoil tested by Brandrud and Krøgenes [14] at an AoA=5° and a Reynolds number of 400,000. The large horn ice features are causing severe flow separation downstream of the horn ice. From Fajt (2019) [20].

4.3. Limitations of the experimental methodological approach

The experimental campaign suffered from a tight schedule inside the L1-B regarding the available testing time. It was restricted to two weeks of which one was consumed by setting up the wind tunnel wing model and measurement equipment. This made straight forward decisions necessary to be able to conduct at least some of the originally planed experiments. One of these decisions was to shift the six component balance calibration to a later time after the experimental campaign. Consequently, due to the lack of the balance calibration matrix, no forces were available throughout the runs to cross-check the acquired values with the expected ones. The arising non-continuous drag increase at the clean airfoil tests might have been already noticed throughout the experimental campaign. Furthermore, it was originally not planned to utilize the *AMS5812 Standard Pressure* sensors type, since their large range and bias error was not designed for the expected fine pressure measurements of the conducted experiments. This was another straight forward decision caused by troubles with saturating pressure sensors and availability of certain pressure sensor types with adequate pressure ranges. The pressure levels had been evaluated with the aid of XFOIL in advance of the experimental campaign and the original finer sensors had been selected on the basis of this evaluation. Therefore it is most likely, that the saturation of some sensors was caused by the later observed constant negative angular offset of the wind tunnel wing model, which is mentioned in section 2.2. As this AoA offset was not discovered during the experimental campaign, the exchange of the saturating pressure sensors with the higher pressure range *AMS5812 Standard Pressure* sensors enabled the execution of the experimental campaign in the given amount of time.

In the following, the several limitations of the experimental methodological approach are addressed firstly with the high pressure uncertainties. Secondly, the source of the in section 3.1 mentioned non-physical aerodynamic coefficient propagations at the Reynolds number regime of 750,000 for higher AoA is discussed. Finally, the also observed non-continuous drag level increase of the clean airfoil experiments is correlated to the effects of the side wall boundary layer interactions with the airfoil and the gap between the wing model and the side walls.

4.3.1. Uncertainties of the pressure measurements

The consequences of the chosen *AMS5812 Standard Pressure* sensors ranges are displayed exemplarily in Figure 4.10 for all experimental pressure coefficient plots. Herein, the determined pressure coefficients of the clean airfoil measurements at an AoA=4.8° are displayed for all three tested Reynolds

numbers with their respective uncertainties as error bars. The upper airfoil side (US) c_p's are given in blue and the lower airfoil side (LS) c_p's are coloured green. Figure 4.10 clearly shows, that at the tested Reynolds number regime of 200,000 and 400,000 the δc_p uncertainties are too high for the *AMS5812 Standard Pressure* sensors to allow a reasonable pressure analysis of the affected pressure tap locations. The affected pressure taps were located on the upper airfoil side between the leading edge and 0.55c and on the lower airfoil side at the first and sixth position. Since the measured local static pressure was not exceeding 20Pa at Re=200,000 and 150Pa at 400,000, the bias error of the *AMS5812 Standard Pressure* sensors were up to 45 times greater. Consequently, the pressure coefficient uncertainties are dominated by the bias error of the *AMS5812 Standard Pressure* sensors. This is why the pressure tap locations of the upper airfoil side until 0.55c were only considered as a general pressure trend.

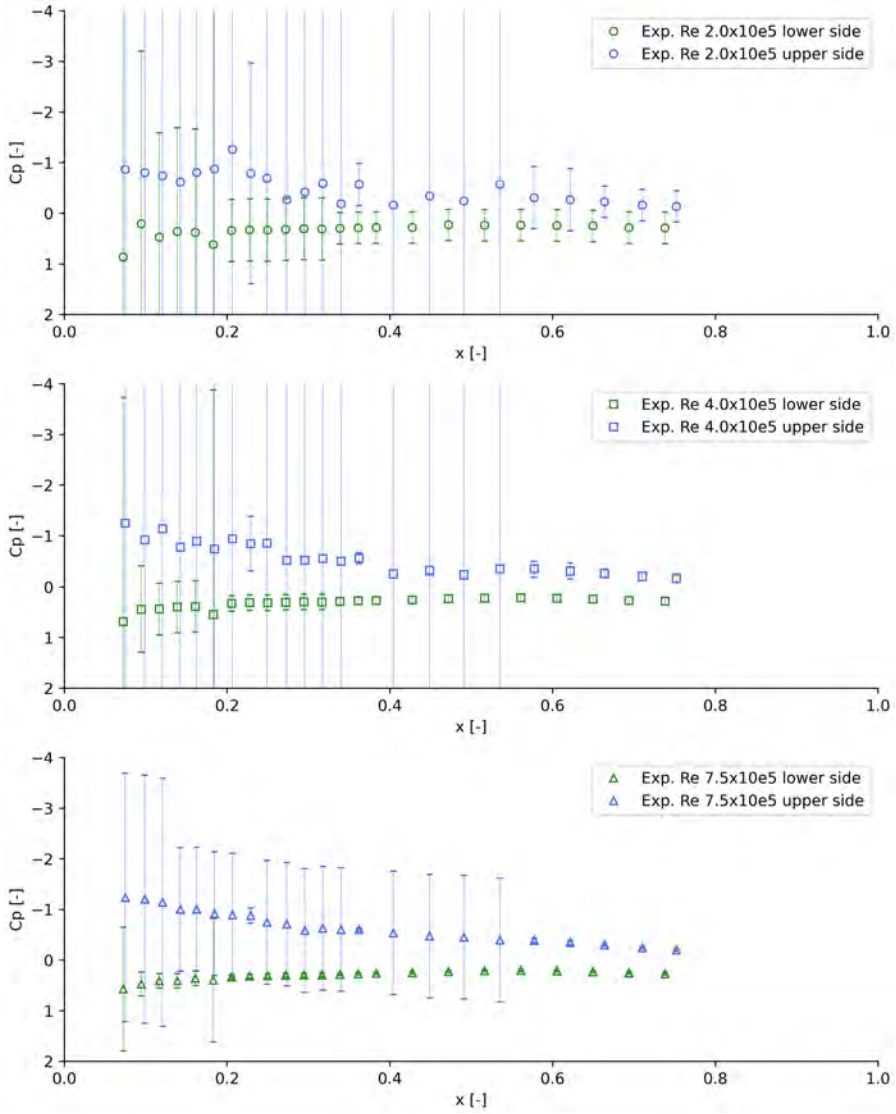

Fig. 4.10.: Clean airfoil c_p over dimensionless chord location x with high uncertainties of the upper airfoil side pressure taps until 0.55c, where the bias error of the installed ams5812 standard pressure sensors dominates the measurements. Displayed are the determined c_p's of the clean airfoil experiments at an AoA=4.8° for the Reynolds numbers 200,000 (top), 400,000 (centre), and 750,000 (bottom), with the upper airfoil side's c_p in blue and the lower airfoil side's c_p in green.

4.3.2. Wing movement correlated with AoA

Before an adaptation with the aid of the pressure coefficient plots, the experimental aerodynamic coefficient plots of the clean airfoil tests at the Reynolds number regime of 750,000 were showing non-physical behaviour for AoA>4.8° (see Figure 3.5). It was possible to correlate the affected aerodynamic coefficients to higher AoA, since a reasonable amount of time was taken into account to reach steady flow conditions before the data acquisition was performed. Furthermore, the observed non-physical behaviour of Figure 3.5 was also present at the aerodynamic coefficient plots of the second time velocity runs at equal AoA (see in the Appendix A.6 the Figures A.6, A.8, and A.10). Consequently the wing rotation took place while reaching the highest tested free stream velocity of 25m/s. An investigation of the wing's break system and dissembling of the wing's rotation axis yielded an insufficient stiffness of the aluminium rods, since the slotted part was slightly twisted (see Figure 4.11). Furthermore, the friction based joint between the wing and the aluminium rods was not able to sufficiently withstand the torques acting on the wing throughout the tests at higher AoA and the highest free stream velocity. This was concluded, since green resin powder was found on top of the slotted aluminium rod part as well as the fact, that the aluminium rod was freely rotatable inside the wing box after the AoAc=13.75° test (see Figure 4.12). However, to further proceed with the testing campaign and be able to test the glaze ice shape at higher AoA, the conducted hands-on solution was to first glue the axes with a two component special adhesive back into the wing box and limit the air speeds to 13.1 m/s for AoA other than -1.3°.

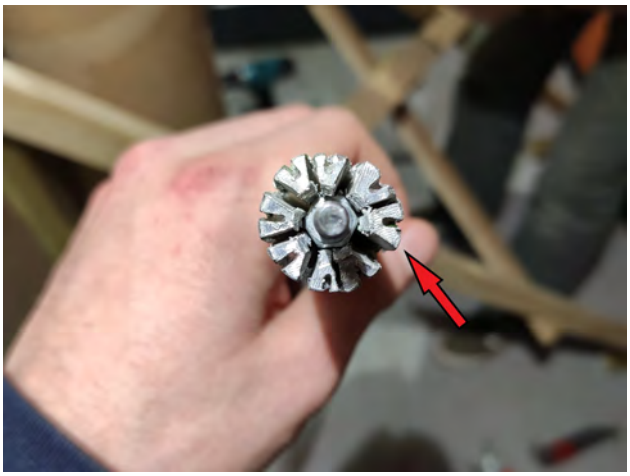

Fig. 4.11.: In axe direction view of the aluminium rod dissembled from the wing. The twisted part is indicated with the red arrow.

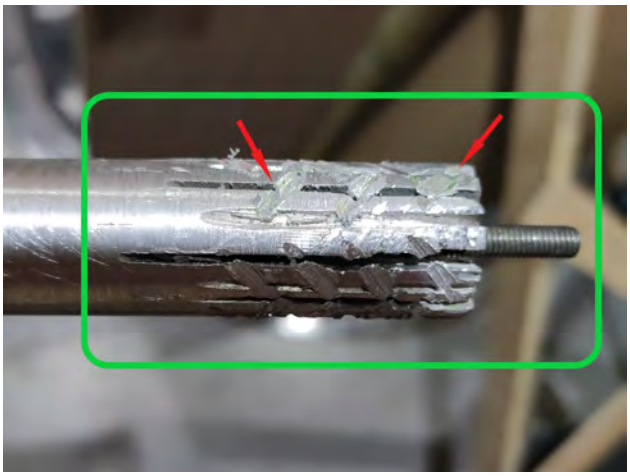

Fig. 4.12.: Top-down view of the dissembled aluminium rod. The part, which is placed inside the wing, is indicated by the green box. Remains of green resin powder is visible inside the carvings (red arrows).

4.3.3. Clean airfoil non-continuous drag level raise

All clean airfoil aerodynamic coefficients plots regardless the Reynolds number exhibited an higher base drag level compared to the CFD simulations and available literature data like Selig [46] or Sartorius [42]. Additionally, a non-continuous drag increase starting from AoA>4.8° was observed as well. E.g. for the Reynolds number regime of 200,000 at the AoA=9°, the experimental drag coefficients were up to 90% greater as the literature experimental data and up to 130% greater as the CFD

simulations. However, the affected region 4.8°>AoA>10.8° shows regarding the pressure distribution good agreement between the CFD simulations and the conducted experiments (see Figure 3.17). The pressure taps were located half-span of the wind tunnel wing model and therefore barely affected by 3D flow effects introduced by e.g. the gap between wooden side walls and wing model. This is why it was concluded that the observed non-continuous drag increase was introduced by 3D effects located at the wing model ends.

The work of Barber [7] and Jacobs et al. [51] encouraged this conclusion. Barber investigated intersection losses at the junction of a planar side wall and a symmetric airfoil at low Reynolds numbers. He discovered an horseshoe vortex to arise at the junction which is schematically displayed in Figure 4.13. Furthermore, Barber found out, that the produced losses are strongly dependant on the initial boundary layer thickness at the blunt protuberance of the airfoil nose. The losses are mainly reflected at low speed flows in form of additional drag caused by the onset of a separation zone at the rear airfoil junction with the side wall [32]. The size of the separation zone is dependant on the side wall's initial boundary layer thickness and the greater, the thinner the boundary layer is (see Figure 4.14). Jacob et al. [51] conducted aerodynamic experiments at a Reynolds number of 330,000

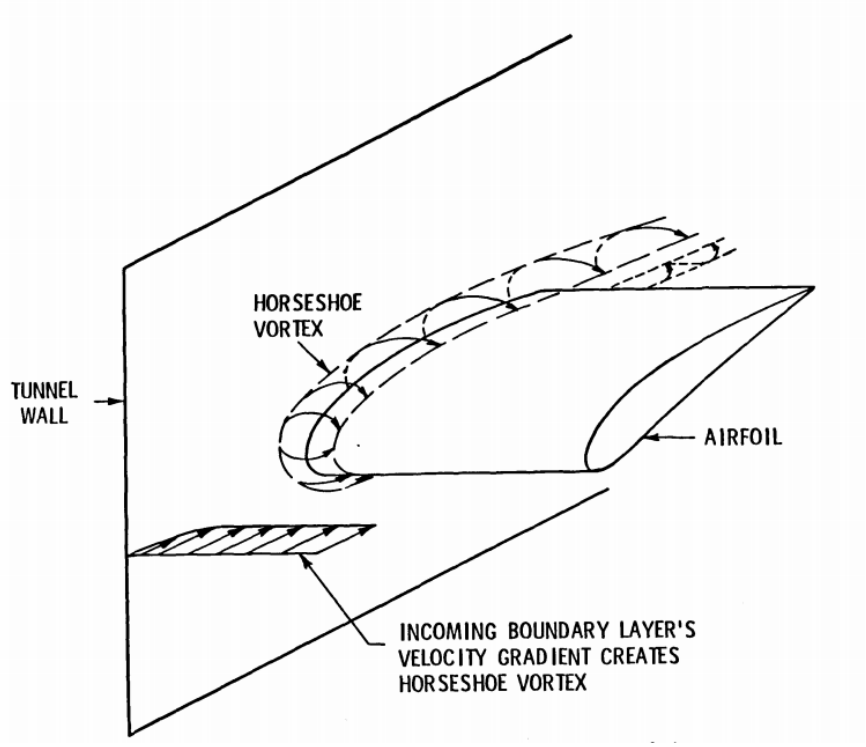

Fig. 4.13.: Horseshoe vortex at the junction of the wind tunnel side wall and airfoil which arises due to the interaction of the wind tunnel side wall boundary layer with the airfoil. From Jacobs et al. (1984) [51].

on a NACA 0012 airfoil and observed a significant difference in the measured drag when changing the drag measurement methodology. They emphasized the insufficiency of "the traditional corrections discussed by Pope [39] and Allen and Vincenti [2] [...]" [51, p. 8] for 2D wind tunnel testing with three component balances. Jacob et al. [51] compared two drag measurement methodologies: A reference case, where the airfoil's drag was determined based on momentum principles of the downstream wake at the midsection with a kiel probe, whose drag levels were alike previous tests on the same airfoil. And a test case, whose drag was measured with a three component balance as it was the case during this thesis' experiments. Both experiments showed a difference of the three component balance

measurements to the reference kiel probe measurements of up to one order of magnitude [51]. This was also observed during this thesis data analysis (see section 3.1). Jacob et al. concluded that the discrepancy in the drag data resulted from a "contamination of the two-dimensional flow by an interaction of the airfoil and the sidewall boundary layer" [51, p. 12] since the contribution to the force measurements of the exposed balance shaft (wing rotation axis) and the gap between wing and side wall of less than 0.25mm could be neglected after a deeper analysis [51]. Therefore, they proposed a semi-empirical correction for balance-measured drag data, which is to be applied on the drag data after the traditional corrections (see Equation 4.3.1). Herein, the geometry of the airfoil is included by the airfoil's aspect ratio AR and dimensionless maximum thickness $\frac{t}{c}$. The side wall boundary layer thickness is introduced by $\frac{\delta}{c}$. The balance-measured drag reference point is the drag coefficient at zero lift c_{d_0}. The slope of the linear part of the lift coefficient versus the AoA is described by $c_{l_{\alpha_0}}$ and the local slope of the lift coefficient versus the AoA is c_{l_α}.

$$\Delta c_d = 1.9 \cdot 10^{-5} \frac{c_l c_{d_0} \sqrt{\frac{c_{l_\alpha}}{c_{l_{\alpha_0}}}}}{\frac{\delta}{c}\left(\frac{t}{c}\right)^4 \sqrt{AR}} \tag{4.3.1}$$

$$\delta \approx 5\sqrt{\frac{\nu x}{v_\infty}} \tag{4.3.2}$$

It was assumed that the boundary layer of the wind tunnel side wall is still laminar at the airfoil position, since the Reynolds number after an approximated development length of x=0.7m is $<1 \cdot 10^6$ for v_∞=25.13$\frac{m}{s}$. The estimation of the boundary layer thickness at the airfoil position according to Equation 4.3.2 proposed by Schlichting [43, p. 140] yielded with a kinematic viscosity of ν=1.4722 $\cdot 10^{-5} \frac{m^2}{s}$:

- δ=6.2mm for v_∞=6.63$\frac{m}{s}$
- δ=4.4mm for v_∞=13.26$\frac{m}{s}$
- δ=3.2mm for v_∞=25.13$\frac{m}{s}$

Picking up the previous stated observation by Barber, the decreasing side wall boundary layer thickness should introduce higher drag losses at the respective velocity test case. However, a higher drag loss was only present at the highest velocity and AoA>10° in comparison to the two other tested velocity cases. In addition, three points prevented a meaningful application of Jacob et al.'s correction onto the retrieved experimental data:

1. The base drag level at c_l=0 was significantly higher than comparable literature data on the RG-15 at a Reynolds number of 200,000 and as the obtained one by Jacob et al. on their NACA0012 airfoil at a Reynolds number of 330,000.
2. The estimated boundary layer thickness at the wing model position was significantly thinner as the measured boundary layer thickness of Jacob et al.'s experiments (δ=4.4mm at v_∞=13.26$\frac{m}{s}$ vs. Jacob et al.'s δ=57.2mm at v_∞=15.24$\frac{m}{s}$).
3. The gap between the side wall and the airfoil was significantly lower during Jacob et al.'s experiments and their limit of the gap-to-chord ratio of <0.002, which allows to reasonably neglect the gap effect, was exceeded during this thesis' experiments with a gap-to-chord ratio of 0.006.

Furthermore, according to Mokry et al. [32], the validity of semi-empirical corrections for low aspect ratio wings is not reliably applicable. Since in these thesis, no flow visualization techniques or boundary layer measurements were conducted, making a statement on the flow distortion at the

junction was difficult. In conclusion, the increased base drag level and non-continuous drag increase at higher AoA was correlated phenomenologically to the distortion of the 2D-flow over the airfoil near the junction of the airfoil and the side wall, which was most likely induced by the interaction between the side wall's boundary layer and the airfoil nose.

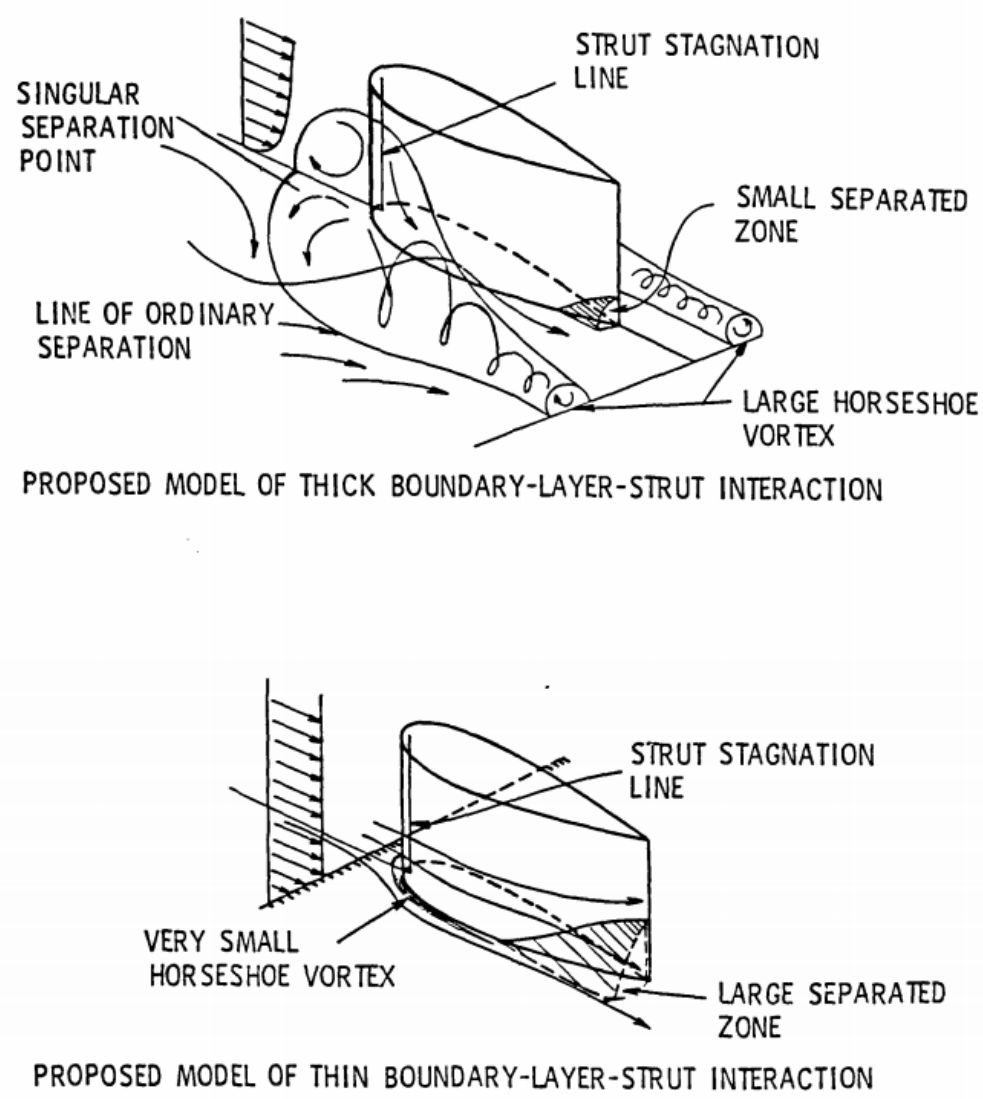

Fig. 4.14.: Effect of the initial side wall boundary layer thickness on the size of the separation cell at the airfoil rear junction with the side wall: The thinner the initial boundary layer thickness of the side wall at the protuberance of the airfoil nose, the greater the separation cell's size and induced drag losses. From Jacobs et al. (1984) [51] who adapted it from Barber (1978) [7].

5. Summary

Experimental and numerical studies in the field of atmospheric in-flight icing at low Reynolds numbers of a typical fixed-wing and medium sized UAV type airfoil were conducted throughout this thesis. The studies were motivated by the lack of available experimental data on the aerodynamic icing penalties at low Reynolds numbers on typical UAV airfoils. As the UAV market sees annual growth rates of up to 25% and operational envelopes of the commercial and military sector UAVs require all weather capabilities, also the interest in UAV research and key limitations of UAVs is emerging. One key limitation had been identified to be the atmospheric in-flight icing of fixed-wing and medium sized UAVs with ceiling heights of up to 6000m. Existing numerical tools are validated for Reynolds numbers, which are typically one order of magnitude higher than those of the mentioned UAV type. Experimental and numerical studies have shown a strong dependency on the Reynolds number of the ice accretion and on the resulting aerodynamic penalties. To enable the development of ice-protection technologies also for UAV applications, the existing numerical tools must be validated for the low Reynolds number regimes of these UAV applications. This is why, this thesis aimed to contribute to the validation process of the ANSYS FENSAP module with experimental data on the aerodynamic penalties of a typical and artificially iced UAV airfoil.

The experimental campaign was conducted inside the large L1-B wind tunnel of the VKI at three different Reynolds number regimes of 200,000, 400,000, and 750,000. To retrieve 2D testing conditions, a smaller 2D-wind tunnel out of wood was constructed inside the larger L1-B test section. The utilized wing model was based on the standard radio controlled model sailplane RG-15 airfoil by Rolf Girsberger and had a chord length of 450mm. 23 pressure taps per wing side enabled besides the load measurements with a six-component platform balance also the determination of the pressure coefficient propagation. A clean airfoil sweep was performed and served as a baseline to resolve the ice induced aerodynamic penalties. The RG-15 wind tunnel wing model was artificially iced by adding 3D-printed ice geometries to the leading edge of the wing model. These ice geometries were retrieved throughout an icing wind tunnel experiment on a similar RG-15 airfoil by the NTNU. A 2D cut of the accreted ice topologies was extruded to the full span-width of the wind tunnel wing model to simplify the experiments to 2D flow conditions. The baseline airfoil was tested from -7.3°<AoA<13.8° with a general angular resolution of 3° and a 1° resolution starting from AoA=7.8° at the Reynolds number regimes of 200,000, 400,000, and 750,000. The experimental campaign was initially set up to perform angular sweeps for all artificial ice shapes. Ultimately, time restrictions limited the experimental parametric study to test only the glaze ice shape from -7.3°<AoA<9.8° with a general angular resolution of 3° and a 1° resolution starting from AoA=7.8° at the Reynolds number regimes of 200,000 and 400,000. Nevertheless, it was possible to test each of the artificial ice shapes at an AoA=-1.3° at the three Reynolds number regimes of the baseline RG-15.

The experimental campaign revealed the glaze ice shape to introduce the highest aerodynamic penalties to the RG-15 wind tunnel wing model. The minimum drag of the baseline RG-15 wind tunnel wing model was increased by the glaze ice shape with +130%, followed by the mixed ice shape with +117% and by the rime ice shape with +92% at the highest tested Reynolds number regime of 750,000. It was observed that the lower the Reynolds number was, the lower the ice shape induced

aerodynamic penalties were. E.g. at a Reynolds number regime of 200,000, the minimum drag of the baseline RG-15 wind tunnel wing model was approximately increased for all ice shape types by +40% and at the Reynolds number regime of 400,000, the minimum drag increase reached up to +108% for the mixed ice shape. Besides the drag penalties, the achievable lift at minimum drag was reduced the lowest by the mixed ice shape with -20% up to -31% and equally reduced by rime and glaze ice with approximately -50% at the Reynolds number regimes of 400,000 and 750,000. Furthermore, the glaze ice shape introduced in general an unstable "nose-down" moment coefficient propagation to the baseline RG-15 wind tunnel wing model, which was more severe at lower Reynolds numbers. For positive AoA, the aerodynamic performance of the glaze iced RG-15 airfoil showed no significant dependency on the Reynolds number. All clean airfoil experiments exhibited non-continuous drag level increases for AoA>4.8° and showed an higher base drag level compared to literature data at a Reynolds number of 200,000 and the FENSAP CFD simulations in general. This was correlated to the interaction between the wind tunnel side wall boundary layer and the airfoil nose at the junction of the airfoil and the side wall. According to Barber [7], an from this interaction arising horseshoe vortex causes a separation region at the rear airfoil near the junction, which contaminates mainly the balance-measured drag. Furthermore, at higher AoA and the highest tested Reynolds number regime of 750,000, it was observed for the clean airfoil case that the wing's rotation axis could not withstand the acting torques anymore and a movement of the wing took place before the acquisition of the run. With the aid of the pressure coefficient plots, it was possible to correlate the aerodynamic coefficients to a more reasonable AoA, since special care was taken to acquire each test in steady flow conditions. However, the high uncertainties of the upper aifroil side pressure sensors at the Reynolds number regimes of 200,000 and 400,000 made a statement on the pressure coefficient propagation and an analysis of the flow transition difficult.

The numerical campaign was conducted with the ANSYS FENSAP module and the one-equation Spalart-Allmaras turbulence model, which is of first-order closure. The flow transition locations of the baseline RG-15C were predicted by the software tool XFOIL and superimposed to the steady-state 2D RANS CFD simulations. The general numerical simulation approach was adapted from Fajt [20], since he conducted a grid dependency study on a similar RG-15 airfoil. A hybrid O-grid was selected for the performance grids of the iced and clean RG-15C airfoil. The initial wall spacing of the structured grid near the airfoil was $\Delta s = 1.0 \cdot 10^{-6} m$ to cope with the condition of the dimensionless wall distance of the nearest wall grid point $y+ \leq 1$ and adequately resolve the viscous sub- and transient layers of the airfoil boundary layer. The hybrid O-grid was settled in the medium resolution region according to Mavriplis et al.[31]. The baseline RG-15 airfoil was simulated in general with an 1° angular resolution in between -8°<AoA<14°. In between -4°<AoA<6° the resolution was set to 2° to limit the number of to be generated meshes per transition location change with AoA and Reynolds number regime. It was assumed for the iced RG-15C airfoil that no flow transition from laminar to turbulent flow occurs and the ice shapes force the flow to instantaneously trip. Therefore, the iced RG-15C was each simulated for the artificial glaze, mixed, and rime ice shape with an angular resolution of 1° in between -8°<AoA<14°. An equivalent sand-grain roughness of $\varepsilon = 19.1 \mu m$ was superimposed to the ice shapes based on literature of 3D-printed surface roughness by Arnold et al. [6]. The reference conditions of the FENSAP CFD simulations were adapted from the experimental campaign ambient conditions. A validation of the clean RG-15C airfoil case was conducted with literature data on the RG-15 airfoil at a Reynolds number of 200,000 and yielded that the chosen simulation approach was in general capable of adequately predicting the experimental data with some limitations regarding the onset of stall.

The numerical simulation approach showed limitations in the prediction of the maximum lift and stall behaviour of the clean RG-15C airfoil, which was in general more conservative. The drag coefficient

of the RG-15 wind tunnel wing model was in general under-predicted but was also suspected to be contaminated by the mentioned interaction between the side wall boundary layer and the airfoil. The drag coefficients of the simulated and experimental glaze ice case were fairly matching but also under-predicted. A detailed comparison of the numerical and experimental ice shape cases at the AoA=-1.3° and a comparison to an iced S826 NREL airfoil at a similar Reynolds number lead to the conclusion that the Spalart-Allmaras turbulence model seemed to be limited applicable for estimating the ice induced aerodynamic penalties at low Reynolds numbers. To justify this conclusion, further experiments must be conducted with major improvements to the experimental methodological approach. A selection of proposed improvements was provided in the course of this thesis, e.g. the change of the drag measurement technique or the utilization of adequate pressure sensor ranges with high manufacturing accuracy.

6. Outlook and future work

The critical analysis of the conducted experimental campaign allows the proposal of several improvements to the methodological approach, which are presented in the following:

- Approximately two weeks are to be expected to account for the calibration of the wind tunnel, the set-up of the wing model and the calibration of the testing equipment. The calibration of the six component platform balance can consume up to one week. Dependant on the amount of pressure sensors to be calibrated, a thumb-rule might be that 8-12 sensors per day are possible to be calibrated by an inexperienced student. It might be also wise to schedule one additional week of buffer time to the overall estimated wind tunnel campaign time to compensate unexpected measurement equipment behaviour.
- As observed during this thesis and previous wind tunnel tests from literature, the balance-measured drag of low aspect ratio wings is prone to contaminations by interactions between the 2D airflow of the airfoil and the wind tunnel side wall boundary layer. This issue might be compensated by either the utilization of a different methodological approach for the drag measurement like wake rakes, or the utilization of high aspect ratio wings with gab-to-chord ratios of <0.002. In any case, a boundary layer thickness measurement of the 2D wind tunnel side walls should be conducted in the curse of the wind tunnel calibration.
- An estimation and analysis of the measurement uncertainties should be performed prior to the experimental campaign. This allows a reasonable selection of the measurement equipment regarding the introduced bias errors and the required number of samples to achieve desired uncertainty limits.
- It is advisable to utilize a fail-safe or even better a safe-life design approach for the wing, the joint between wing and rotation axis, the rotation axis itself, the wing support struts and the rotation axis' break system. E.g. would be one axis out of rigid steel with protuberant elements inside the wing box to transfer and withstand the arising torques and forces throughout the experiments. Although this is most likely correlated to increased costs, the advantages predominate since this enables cleaner measurements, better results, and less troubles during the experimental campaign.
- Barlow et al. [8, pp. 265-271] mention besides other things that closed 2D wind tunnel test sections are prone to a sightly upstream directed incoming airflow. To compensate and apply corrections for the introduced AoA change and contamination of the balance-measured loads, they suggest to estimate the upstream directed airflow influence by measuring a sweep of the upside down airfoil.

Multiple possible suggestions for future studies arose throughout this thesis. A 3D numerical simulation of the 2D wind tunnel experiments could be used to better understand the effects of the interaction between the side-wall boundary layer and the wing model.

Since it was not possible to test the rime and mixed ice shapes at AoA other than -1.3° , stall conditions were not reached for the glaze ice shape, the angular resolution was rather coarse and

especially the drag measurements were suspected to be contaminated by 3D flow effects, further wind tunnel experiments are necessary and recommended to validate the ANSYS FENSAP module for the low Reynolds number regimes of fixed-wing and medium sized UAVs.

It is also recommended to investigate other turbulence models of higher order such as Reynolds stress and non-linear eddy viscosity models, because the one-equation Spalart-Allmaras turbulence model showed clear limitations.

Especially the inclusion of flow visualization techniques like particle image velocimetry would allow a cross-validation of the numerical and experimental flow fields.

Furthermore, the influence of the spanwise ridge ice was not covered by this thesis. As heating based de-icing techniques sometimes causes the leading edge ice to slide on a thin liquid water film farther downstream and freeze again to the wing surface instead of shading away, research on the spanwise ridge ice aerodynamic performance penalties might be also of great interest.

Bibliography

[1] T. Adams, C. Grant, and H. Watson, *A Simple Algorithm to Relate Measured Surface Roughness to Equivalent Sand-grain Roughness*, International Journal of Mechanical Engineering and Mechatronics, vol. 1, issue 1 (2012), pp. 66–71, https://doi.org/10.11159/ijmem.2012.008.

[2] H. J. Allen and W. G. Vincenti, *Wall interference in a two-dimensional-flow wind tunnel, with consideration of the effect of compressibility*, report NACA-TR-782, NASA, Work of the US Gov. Public Use Permitted, 1944, https://ntrs.nasa.gov/citations/19930091861.

[3] Analog Microelectronics GmbH, *AMS 5812*, Datasheet, 2012, https://www.analog-micro.com/products/pressure-sensors/board-mount-pressure-sensors/ams5812/ams5812-datasheet.pdf (accessed 2021-04-04).

[4] ANSYS, Inc., *ANSYS FENSAP-ICE User Manual v18.2*, ANSYS, Inc., Canonsburg, Pennsylvania, USA, 2017.

[5] Ansys, Inc, *Ansys FENSAP-ICE, Ice Accretion Simulation Software*, 2021, https://www.ansys.com/products/fluids/ansys-fensap-ice (accessed 2021-03-21).

[6] C. Arnold, D. Monsees, J. Hey, and R. Schweyen, *Surface Quality of 3D-Printed Models as a Function of Various Printing Parameters*, Materials, vol. 12, no. 12 (2019), https://doi.org/10.3390/ma12121970.

[7] T. J. Barber, *An Investigation of Strut-Wall Intersection Losses*, Journal of Aircraft, vol. 15, no. 10 (1978), pp. 676–681, https://doi.org/10.2514/3.58427.

[8] J. B. Barlow, J. W. H. Rae, and A. Pope, *LOW-SPEED WIND TUNNEL TESTING*, vol. 3, John Wiley and Sons Inc., USA, 1999.

[9] J. Bartl, K. F. Sagmo, T. Bracchi, and L. Sætran, *Performance of the NREL S826 airfoil at low to moderate Reynolds numbers—A reference experiment for CFD models*, European Journal of Mechanics - B/Fluids, vol. 75 (2019), pp. 180–192, https://doi.org/10.1016/j.euromechflu.2018.10.002.

[10] B. C. Bernstein and C. Le Bot, *An Inferred Climatology of Icing Conditions Aloft, Including Supercooled Large Drops. Part II: Europe, Asia, and the Globe*, Journal of Applied Meteorology and Climatology, vol. 48, no. 8 (2009), pp. 1503–1526, https://doi.org/10.1175/2009JAMC2073.1.

[11] B. C. Bernstein, C. A. Wolff, and F. McDonough, *An Inferred Climatology of Icing Conditions Aloft, Including Supercooled Large Drops. Part I: Canada and the Continental United States*, Journal of Applied Meteorology and Climatology, vol. 46, no. 11 (2007), pp. 1857–1878, https://doi.org/10.1175/2007JAMC1607.1.

[12] J. Blazek, *Computational Fluid Dynamics: Principles and Applications*, Butterworth-Heinemann, 3 ed., 2015, https://doi.org/10.1016/C2013-0-19038-1.

[13] M. B. Bragg, A. P. Broeren, and L. A. Blumenthal, *Iced-airfoil aerodynamics*, Progress in Aerospace Sciences, vol. 41 (2005), pp. 323–362, https://doi.org/10.1016/j.paerosci.2005.07.001.

[14] L. Brandrud and L. Krøgenes, *Aerodynamic Performance of the NREL S826 Airfoil in Icing Conditions*, master's thesis, Norwegian University of Science and Technology (NTNU), 2017.

[15] J. Chung and J. H. Addy, *A numerical evaluation of icing effects on a natural laminar flow airfoil*, in 38th Aerospace Sciences Meeting and Exhibit, Reno, Nevada, USA, AIAA, 2000, https://doi.org/10.2514/6.2000-96.

[16] N. I. Corp., *What is LabVIEW?*, 2021, https://www.ni.com/en-no/shop/labview.html (accessed 2021-03-21).

[17] N. Coudou, *WIND TURBINE / FARM WAKE(S) MEANDERING STUDY IN AN ABL WIND TUNNEL*, research report 2016-05, von Karman Institute for Fluid Dynamics, Rhode Saint Genèse, Belgium, 2016.

[18] M. Drela, *XFOIL: An Analysis and Design System for Low Reynolds Number Airfoils*, in Low Reynolds Number Aerodynamics. Lecture Notes in Engineering, T. J. Mueller, ed., vol. 54, Springer, Berlin, Heidelberg, 1989, pp. 1–12, https://doi.org/10.1007/978-3-642-84010-4_1.

[19] M. Drela and H. Youngren, *XFOIL, Subsonic Airfoil Development System*, https://web.mit.edu/drela/Public/web/xfoil/ (accessed 2021-03-21).

[20] N. Fajt, *The Influence of Meteorological Conditions on the Icing Performance Penalties on a UAV Airfoil*, master's thesis, Institute of Aerodynamics and Gas Dynamics of the University of Stuttgart, 2019.

[21] N. Fajt, R. Hann, and T. Lutz, *The Influence of Meteorological Conditions on the Icing Performance Penalties on a UAV Airfoil*, Proceedings of the 8th European Conference for Aeronautics and Space Sciences, Madrid, Spain, 2019, https://doi.org/10.13009/EUCASS2019-240.

[22] Federal Aviation Administration, *FAA Aerospace Forecast Fiscal Years 2019-2039*, report, USA, 2019.

[23] R. Hann, *UAV Icing: Ice Accretion Experiments and Validation*, in SAE Technical Paper Series, No. 2019-01-2037, SAE International, 2019, https://doi.org/10.4271/2019-01-2037.

[24] R. Hann, *Atmospheric Ice Accretions, Aerodynamic Icing Penalties, and Ice Protection Systems on Unmanned Aerial Vehicles*, phd thesis ntnu2020:200, Norwegian University of Science and Technology, 2020.

[25] R. Hann and T. A. Johansen, *Unsettled Topics in Unmanned Aerial Vehicle Icing*, SAE EDGE Research Report EPR2020008, 2020, https://doi.org/10.4271/EPR2020008.

[26] R. Hann and T. A. Johansen, *UAV Icing: The Influence of Airspeed and CHord Length on Performance Degradation*, Aircraft Engineering and Aerospace Technology, (accepted 2021).

[27] imageJ v1.53i, *ImageJ, Image Processing and Analysis in Java*, 2021, https://imagej.nih.gov/ij/index.html (accessed 2021-03-20).

[28] T. Jokela and R. Prieto, *Icing wind tunnel*, 2021, https://www.vttresearch.com/sites/default/files/2020-06/Wind%20power_Icing_wind_tunnel.pdf (accessed 2021-02-11).

[29] T. G. Lee and olprod, *Welcome to the Visual Studio IDE*, https://docs.microsoft.com/de-de/visualstudio/get-started/visual-studio-ide?view=vs-2019 (accessed 2021-03-21).

[30] T. Lutz, W. Würz, and S. Wagner, *Numerical Optimization and Wind-Tunnel Testing of Low Reynolds-Number Airfoils*, in Proceedings Conference on: Fixed, Flapping and Rotary Wing Vehicles At Very Low Reynolds Numbers, University of Notre Dame, Indiana, USA, June 2000.

[31] D. J. Mavriplis, J. C. Vassberg, E. N. Tinoco, M. Mani, O. P. Brodersen, B. Eisfeld, R. A. Wahls, J. H. Morrison, T. Zickuhr, D. Levy, and M. Murayama, *Grid Quality and Resolution Issues from the Drag Prediction Workshop Series*, no. AIAA 2008-930, 46th AIAA Aerospace Sciences Meeting and Exhibit, Reno, Nevada, USA, 2008, https://doi.org/10.2514/6.2008-930.

[32] M. Mokry, Y. Y. Chan, and D. J. Jones, *Two-dimensional Wind Tunnel Wall Interference*, Advisory Group for Aerospace Research and Development, North Atlantic Treaty Organization, Neuilly sur Seine, France, 7 ed., 1983.

[33] A. S. Morris and R. Langari, *Measurement and Instrumentation*, Elsevier Inc., San Diego, California, USA, 2012.

[34] M. M. O'Meara and T. J. Mueller, *Laminar Separation Bubble Characteristics on an Airfoil at Low Reynolds Numbers*, American Institute of Aeronautics and Astronautics (AIAA) Journal, vol. 25, No. 8 (1987), pp. 1033–1041, https://doi.org/10.2514/3.9739.

[35] N. L. Oo, P. J. Richards, and R. N. Sharma, *Ice-Induced Separation Bubble on RG-15 Airfoil at Low Reynolds Number*, American Institute of Aeronautics and Astronautics (AIAA) Journal, (2020), pp. 1–12, https://doi.org/10.2514/1.j059257.

[36] J. Partlow and olprod, *Work with Python in Visual Studio on Windows*, https://docs.microsoft.com/de-de/visualstudio/python/overview-of-python-tools-for-visual-studio?view=vs-2019 (accessed 2021-03-21).

[37] Pointwise, *Mesh and Grid Generation Software for CFD*, 2021, https://www.pointwise.com/pointwise/software (accessed 2021-03-21).

[38] M. K. Politovich, *Aircraft icing*, in Encyclopedia of Atmospheric Sciences, Elsevier, 2003, pp. 68–75, https://doi.org/10.1016/b0-12-227090-8/00055-5.

[39] A. Pope and J. J. Harper, *Low-Speed Wind Tunel Testing*, John Wiley & Sons, Inc., New York, USA, 1 ed., 1966.

[40] K. Pretz, *UBIQ Aerospace Brings the First Drone De-Icing System to Market*, IEEE Spectrum, (2020), https://spectrum.ieee.org/the-institute/ieee-member-news/ubiq-aerospace-brings-the-first-drone-deicing-system-to-market (accessed 31-03-2021).

[41] QY Research, *Global Commercial Drones Market Report, History and Forecast 2014-2025, Breakdown Data by Manufacturers, Key Regions, Types and Application*, 2019, https://www.qyresearch.com/index/detail/1140178/global-commercial-drones-market (accessed 2021-01-29).

[42] D. Sartorius, *Hitzdrahtmessungen zur Grenzschicht- und Nachlaufentwicklung bei Ablöseblasen in der Nähe der Profilhinterkante*, Diplomarbeit, Institut für Aerodynamik und Gasdynamik,

Universität Stuttgart, 2001.

[43] H. Schlichting, *Boundary-Layer Theory*, McGraw-Hill, Inc., 7 ed., 1979.

[44] R. Schwarze, *CFD-Modellierung*, vol. 1, Springer Vieweg, 2013, https://doi.org/10.1007/978-3-642-24378-3.

[45] M. Selig, *UIUC Applied Aerodynamics Group Department of Aerospace Engineering*, 2021, https://m-selig.ae.illinois.edu/ads/coord_database.html (accessed 2021-01-08).

[46] M. Selig, J. Guglielmo, A. Broeren, and P. Giguère, *Summary of Low-Speed Airfoil Data*, vol. 1, SoarTech Publications, Virginia Beach, Virginia, USA, 1995.

[47] H. Shakhatreh, A. H. Sawalmeh, A. Al-Fuqaha, Z. Dou, E. Almaita, I. Khalil, N. S. Othman, A. Khreishah, and M. Guizani, *Unmanned Aerial Vehicles (UAVs): A Survey on Civil Applications and Key Research Challenges*, IEEE Access, vol. 7 (2019), pp. 48572–48634, https://doi.org/10.1109/ACCESS.2019.2909530.

[48] K. Szilder and S. McIlwain, *In-Flight Icing of UAVs - The Influence of Reynolds Number on the Ice Accretion Process*, in SAE Technical Paper Series, SAE International, 2011, https://doi.org/10.4271/2011-01-2572.

[49] K. Szilder and W. Yuan, *In-flight icing on unmanned aerial vehicle and its aerodynamic penalties*, in Progress in Flight Pyhsics, vol. 9, EDP Sciences, 2017, pp. 173–188, https://doi.org/10.1051/eucass/2016090173.

[50] The World Airsports Federation, *FAI AEROMODELLING COMMISSION (CIAM)*, 2020, https://www.fai.org/page/f3-radio-control-soaring (accessed 2021-01-02).

[51] A. L. Treaster, J. P. P. Jacobs, and G. B. Gurney, *Sidewall Boundary Layer Corrections in Subsonic, Two-Dimensional Airfoil/Hydrofoil Testing*, technical memorandum TM 84-43, Pensylvania State University, Applied Research Laboratory, Pensylvania, USA, 1984.

[52] Unpublished, *Low speed investigation of the S3 composite configuration by means of CFD and Experiments in the L1 wind tunnel of VKI*, research report EAR1346, von Karman Institute for Fluid Dynamics, Rhode Saint Genèse, Belgium.

[53] N. Williams, A. Benmeddour, G. Brian, and M. Ol, *The effect of icing on small unmanned aircraft low Reynolds number airfoils*, in AIAC 2017, 17th Australian International Aerospace Congress, Melbourne, Australia, 2017.

[54] J. Winslow, H. Otsuka, B. Govindarajan, and I. Chopra, *Basic Understanding of Airfoil Characteristics at Low Reynolds Numbers*, Journal of Aircraft, vol. 55, No. 3 (2018), pp. 1050–1061, https://doi.org/10.2514/1.C034415.

[55] xftlr5 v6.48, *xflr5, General description*, 2021, http://www.xflr5.tech/xflr5.htm (accessed 2021-03-20).

A. Appendix

A.1. Test matrices

Tab. A.1.: Conducted test matrix with test date at Reynolds numbers of 750,000.

AoA [°]	AoAc [°]	Clean	Glaze	Rime	Mixed	Tripped
-6	-7.25	09.12.20	n.a.	n.a.	n.a.	n.a.
-3	-4.25	08.12.20	n.a.	n.a.	n.a.	n.a.
0	-1.25	09.12.20	11.12.20	11.12.20	14.12.20	10.12.20
3	1.75	09.12.20	n.a.	n.a.	n.a.	n.a.
6	4.75	09.12.20	n.a.	n.a.	n.a.	n.a.
9	7.75	09.12.20	n.a.	n.a.	n.a.	n.a.
11	9.75	09.12.20	n.a.	n.a.	n.a.	n.a.
12	10.75	09.12.20	n.a.	n.a.	n.a.	n.a.
13	11.75	09.12.20	n.a.	n.a.	n.a.	n.a.
15	13.75	09.12.20	n.a.	n.a.	n.a.	n.a.

Tab. A.2.: Conducted test matrix with test date at Reynolds numbers of 200,000 and 400,000.

AoA [°]	AoAc [°]	Clean	Glaze	Rime	Mixed	Tripped
-6	-7.25	09.12.20	11.12.20	n.a.	n.a.	n.a.
-3	-4.25	08.12.20	11.12.20	n.a.	n.a.	n.a.
0	-1.25	09.12.20	11.12.20	11.12.20	14.12.20	10.12.20
3	1.75	09.12.20	11.12.20	n.a.	n.a.	n.a.
6	4.75	09.12.20	11.12.20	n.a.	n.a.	n.a.
9	7.75	09.12.20	11.12.20	n.a.	n.a.	n.a.
10	8.75	14.12.20	14.12.20	n.a.	n.a.	14.12.20
11	9.75	09.12.20	14.12.20	n.a.	n.a.	n.a.
12	10.75	09.12.20	n.a.	n.a.	n.a.	n.a.
13	11.75	09.12.20	n.a.	n.a.	n.a.	n.a.
15	13.75	09.12.20	n.a.	n.a.	n.a.	n.a.

A.2. Pressure sensor calibration

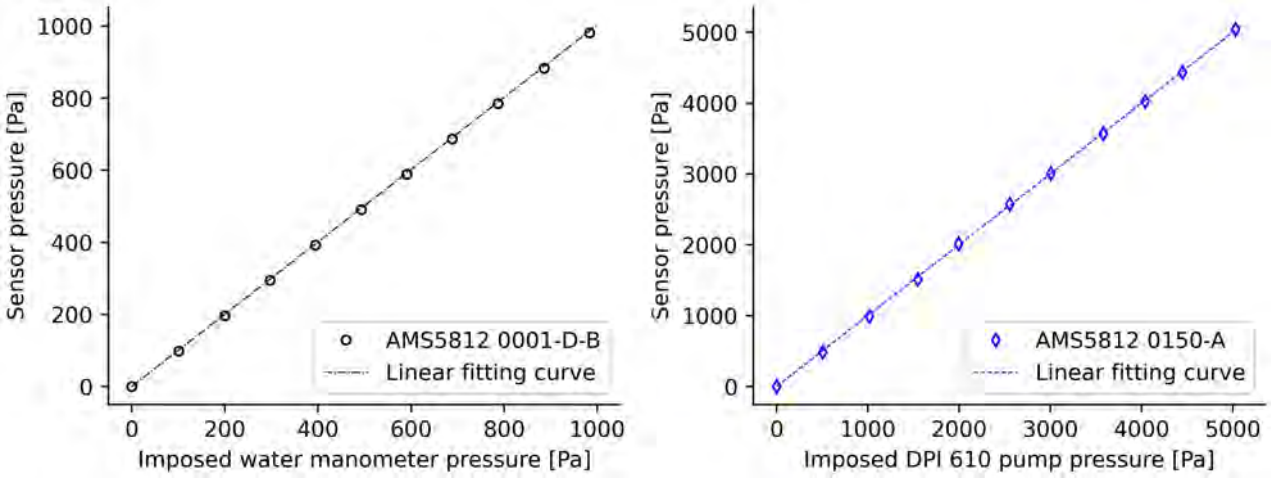

Fig. A.1.: Example of the linear interpolated calibration factors for the pressure sensor calibrations with the water manometer (left) and the DPI 610 pneumatic calibrator pump (right).

Tab. A.3.: Pressure sensor calibration of the upper airfoil side.

Sensor position $\left[\frac{x}{c}\right]$	AMS5812 Sensor Type	Linear interpolated calibration factor	R^2
0.0748	0300-A	0.9968	1.0000
0.0987	0300-A	0.9973	1.0000
0.1206	0300-A	0.9986	1.0000
0.1425	0150-A	1.0003	1.0000
0.1624	0150-A	0.9966	0.9999
0.1845	0150-A	0.9955	1.0000
0.2066	0150-A	1.0008	1.0000
0.2288	0008-D-B	1.0017	1.0000
0.2488	0150-A	0.9996	0.9998
0.2732	0150-A	1.0014	1.0000
0.2954	0150-A	0.9989	0.9999
0.3176	0150-A	1.0025	1.0000
0.3399	0150-A	1.0025	1.0000
0.3621	0003-D	1.0003	1.0000
0.4043	0150-A	1.0017	1.0000
0.4487	0150-A	0.9847	1.0000
0.4909	0150-A	1.0070	1.0000
0.5353	0150-A	1.0022	1.0000
0.5774	0001-D-B	1.0028	1.0000
0.6217	0001-D-B	1.0029	1.0000
0.6637	0000-D-B	1.0110	1.0000
0.7102	0000-D-B	1.0175	1.0000
0.7521	0000-D-B	1.0067	1.0000

Tab. A.4.: Pressure sensor calibration of the lower airfoil side.

Sensor position $\left[\frac{x}{c}\right]$	AMS5812 Sensor Type	Linear interpolated calibration factor	R^2
0.0722	0150-A	1.0010	1.0000
0.0943	0050-D	0.9989	1.0000
0.1165	0030-D	0.9967	1.0000
0.1387	0015-D	0.9999	1.0000
0.1609	0015-D	1.0002	1.0000
0.1831	0150-A	0.9968	1.0000
0.2053	0001-D-B	1.0042	1.0000
0.2276	0001-D-B	1.0035	1.0000
0.2498	0001-D-B	1.0058	1.0000
0.2720	0001-D-B	1.0052	1.0000
0.2942	0001-D-B	1.0035	1.0000
0.3164	0001-D-B	1.0049	1.0000
0.3387	0000-D-B	1.0079	1.0000
0.3609	0000-D-B	1.0073	1.0000
0.3831	0000-D-B	1.0094	1.0000
0.4275	0000-D-B	1.0082	1.0000
0.4719	0000-D-B	1.0070	1.0000
0.5164	0000-D-B	1.0101	1.0000
0.5608	0000-D-B	1.0066	1.0000
0.6051	0000-D-B	1.0078	1.0000
0.6495	0000-D-B	1.0078	1.0000
0.6938	0000-D-B	1.0076	1.0000
0.7381	0000-D-B	1.0075	1.0000

Tab. A.5.: Pressure sensor calibration of the Pitot probe sensors.

Pressure measurement	AMS5812 Sensor Type	Linear interpolated calibration factor	R^2
Dynamic pressure q	0000-D	1.0057	1.0000
Total pressure p_0	0300-A	0.9986	1.0000

A.3. AMS5812 pressure sensor data sheet

AMS 5812
Amplified pressure sensor with analog and digital output (I²C)

PRESSURE RANGES

Sensor type (code)	Pressure type	Pressure range in PSI	Burst pressure[1] in PSI	Pressure range in mbar	Burst pressure[1] in bar
Ultra low pressure					
AMS 5812-0000-D	differential / relative	0…0.075	>5	0…5.17	>0.35
AMS 5812-0001-D	differential / relative	0 … 0.15	>5	0 ...10.34	>0.35
AMS 5812-0000-D-B	bidirectional differential	-0.075 / +0.075	>5	-5.17 / +5.17	>0.35
AMS 5812-0001-D-B	bidirectional differential	-0.15 / +0.15	>5	-10.34 / +10.34	>0.35
Low pressure					
AMS 5812-0003-D	differential / relative	0 … 0.3	>7	0 … 20.68	>0.5
AMS 5812-0008-D	differential / relative	0 … 0.8	>15	0 … 55.16	>1
AMS 5812-0015-D	differential / relative	0 … 1.5	>15	0 … 103.4	>1
AMS 5812-0003-D-B	bidirectional differential	-0.3 / +0.3	>7	-20.68 / +20.68	>0.5
AMS 5812-0008-D-B	bidirectional differential	-0.8 / +0.8	>15	-55.16 / +55.16	>1
AMS 5812-0015-D-B	bidirectional differential	-1.5 / +1.5	>15	-103.4 / +103.4	>1
Standard pressure					
AMS 5812-0030-D	differential / relative	0 … 3	72	0 … 206.8	5
AMS 5812-0050-D	differential / relative	0 … 5	72	0 … 344.7	5
AMS 5812-0150-D	differential / relative	0 … 15	72	0 … 1034	5
AMS 5812-0300-D	differential / relative	0 … 30	225	0 … 2068	15.5
AMS 5812-0600-D	differential / relative	0 … 60	225	0 … 4137	15.5
AMS 5812-1000-D	differential / relative	0 … 100	225	0 … 6895	15.5
AMS 5812-0030-D-B	bidirectional differential	-3 / +3	72	-206.8 / +206.8	5
AMS 5812-0050-D-B	bidirectional differential	-5 / +5	72	-344.7 / +344.7	5
AMS 5812-0150-D-B	bidirectional differential	-15 / +15	72	-1034 / +1034	5
AMS 5812-0150-B	barometric	11 … 17.5	72	758.4 … 1206	5
AMS 5812-0150-A	absolute	0 … 15	72	0 … 1034	5
AMS 5812-0300-A	absolute	0 … 30	72	0 … 2068	5

Table 1: **AMS 5812 standard pressure ranges (other ranges on request)**

Notes:

1) Burst pressure is defined as the maximum pressure which may be applied to one pressure port relative to the other port (or while only one pressure port is connected) without causing leaks in the sensor.

MAXIMUM RATINGS

Parameter	Minimum	Typical	Maximum	Units
Maximum supply voltage: V_S (max)			6.0	V
Operating temperature: T_{op}	-25		85	°C
Storage temperature: T_{amb}	-40		125	°C
Common mode pressure p_{CM} [1)]			175	PSI

Table 2: **Maximum ratings**

Notes:

1) The common mode pressure is defined as the maximum pressure that can be applied on both pressure ports of a differential pressure sensor simultaneously without damaging the sensors housing.

SPECIFICATIONS

All parameters apply to V_S = 5.0V and T_{op} = 25°C, unless otherwise stated.

Parameter	Minimum	Typical	Maximum	Units
Analog output signal (pressure only) [2)]				
@ specified minimum pressure (see "pressure range")[1)]		0.5		V
@ specified maximum pressure (see "pressure range")[1)]		4.5		V
Full span output (FSO) [3)]		4		V
without pressure (bidirectional differential)		2.5		V
Digital output signal (pressure) [4)]				
@ specified minimum pressure (see "pressure range")[1)]		3277		counts
@ specified maximum pressure (see "pressure range")[1)]		29491		counts
Full span output (FSO) [3)]		26214		counts
without pressure (bidirectional differential)		16384		counts
Digital output signal (temperature) [5)]				
@ minimum temperature T = -25°C		3277		counts
@ maximum temperature T = 85°C		29491		counts
Accuracy [6)] (pressure measurement) @ T = 25°C				
Ultra low pressure sensors (0.075, 0.15 PSI)			±1.5	%FSO
Low pressure sensors (0.3, 0.8, 1.5 PSI)			±1.0	%FSO
Standard pressure sensors			±0.5	%FSO
Overall error [7)] (pressure meas.) @ T = -25...85°C				
Ultra low pressure sensors (0.075, 0.15 PSI)			±2.0	%FSO
Low pressure sensors (0.3, 0.8, 1.5 PSI)			±1.5	%FSO
Standard pressure sensors			±1.0	%FSO
Total error for temperature measurement				
All types of AMS 5812 T = -25...85°C			±3.0	%FSO
Long term stability			<0.5	%FSO/a
Ratiometricity error (@V_S = 4.75 …5.25V)			500	ppm

Parameter	Minimum	Typical	Maximum	Units
Resolution A/D converter		14		bits
Resolution D/A converter		11		bits
Resolution analog output signal		0.05		%FSO
Resolution digital output signals	12			bit
Reaction time (10%...90% rise time)		1	2	ms
Supply voltage (V_S)	4.75	5	5.25	V
Current consumption			5	mA
Load resistance at output RL	2k			Ω
Capacitive load			50	nF
I2C-interface				
Input High Level	90		100	% V_S
Input Low Level	0		10	% V_S
Output Low Level	0		10	% V_S
Load capacitance @ SDA			400	pF
Clock frequency SCL			400	kHz
Pull-up resistor	500			Ω
Pressure changes	10^6			
Compensated temperature range	-25		85	°C
Weight		3		g
Media compatibility	See "Specification notes" [8) 9)]			

Table 3: **Specifications**

SPECIFICATION NOTES

1) See *Table 1*
2) The analog output signal (pressure measurement only) is ratiometric to the supply voltage.
3) The Full Span Output (FSO) is the algebraic difference between the output signal at the specified minimum pressure and the output signal at the specified maximum pressure (see "Pressure range").
4) The digital output pressure signal is not ratiometric to the supply voltage.
5) The digital output temperature signal is not ratiometric to the supply voltage. The temperature value is measured at the piezoresistive measuring cell and is the sensor temperature (including self heating).
6) Accuracy is defined as the maximum deviation of the measurement value from the ideal characteristic curve at room temperature (RT) in %FSO including the adjustment error (offset and span), nonlinearity, pressure hysteresis and repeatability. Nonlinearity is the measured deviation from the best fit straight line (BFSL) across the entire pressure range. Pressure hysteresis is the maximum deviation of the output value at any pressure within the specified range when this pressure is cycled to and from the minimum or maximum rated pressure. Repeatability is the maximum deviation of the output value at any pressure within the specified range after 10 pressure cycles.
7) The overall error is defined as the maximum deviation of the measurement value from the ideal characteristic curve in %FSO across the entire temperature range (-25 … 85°C).
8) Media compatibility of pressure port 1 (for a description of port 1, see *Figure 5*): clean, dry gases, non-corrosive to silicon, RTV silicone rubber, gold (alkaline or acidic liquids can destroy the sensor).
9) Media compatibility of pressure port 2 (for a description of port 2, see *Figure 5*): fluids and gases non-corrosive to silicon, Pyrex, RTV silicone rubber.

A.4. Wind tunnel wing model contour measurement

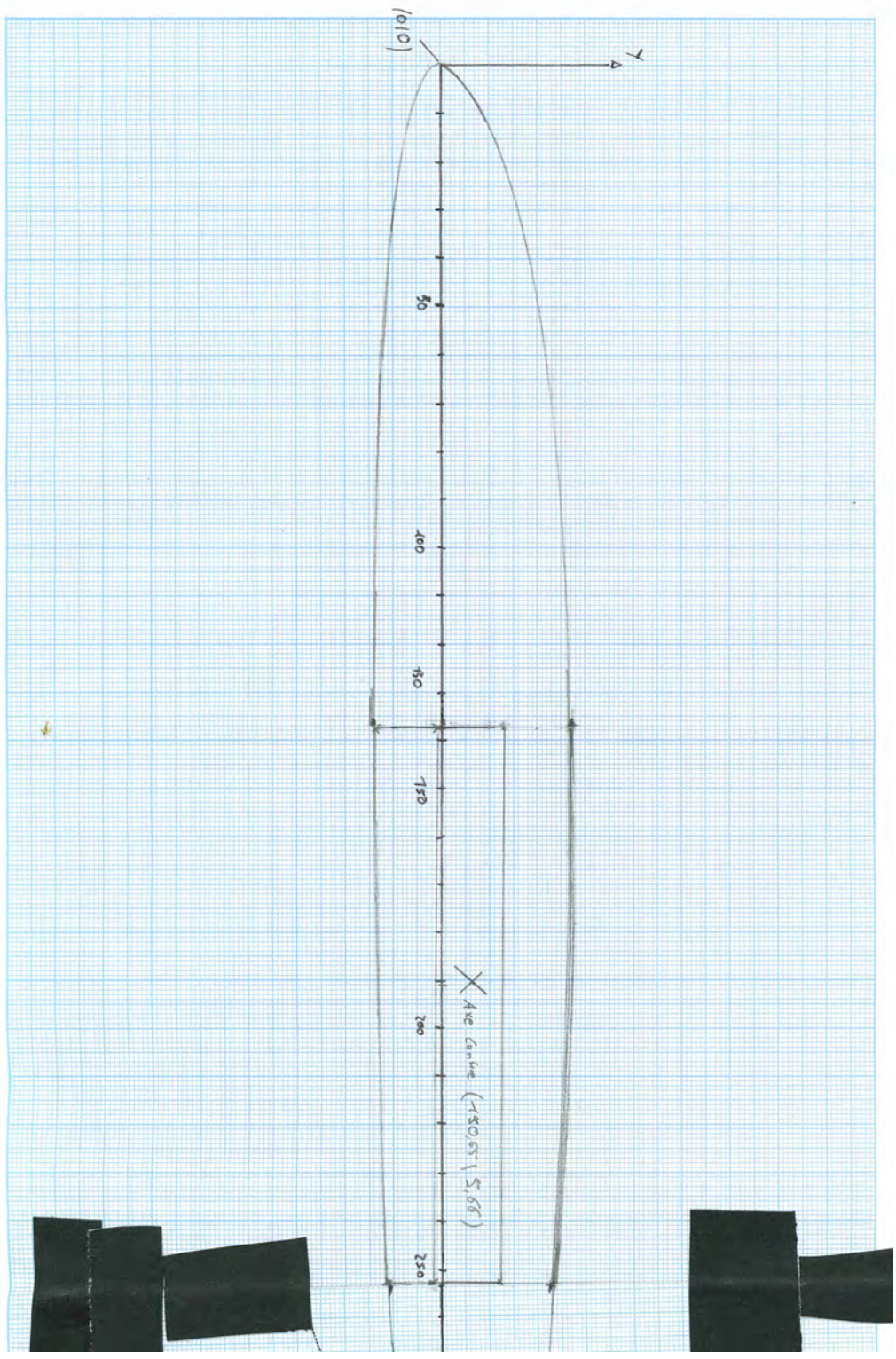

Fig. A.2.: Scan [1:2] of the wind tunnel wing model profile contour trace plot.

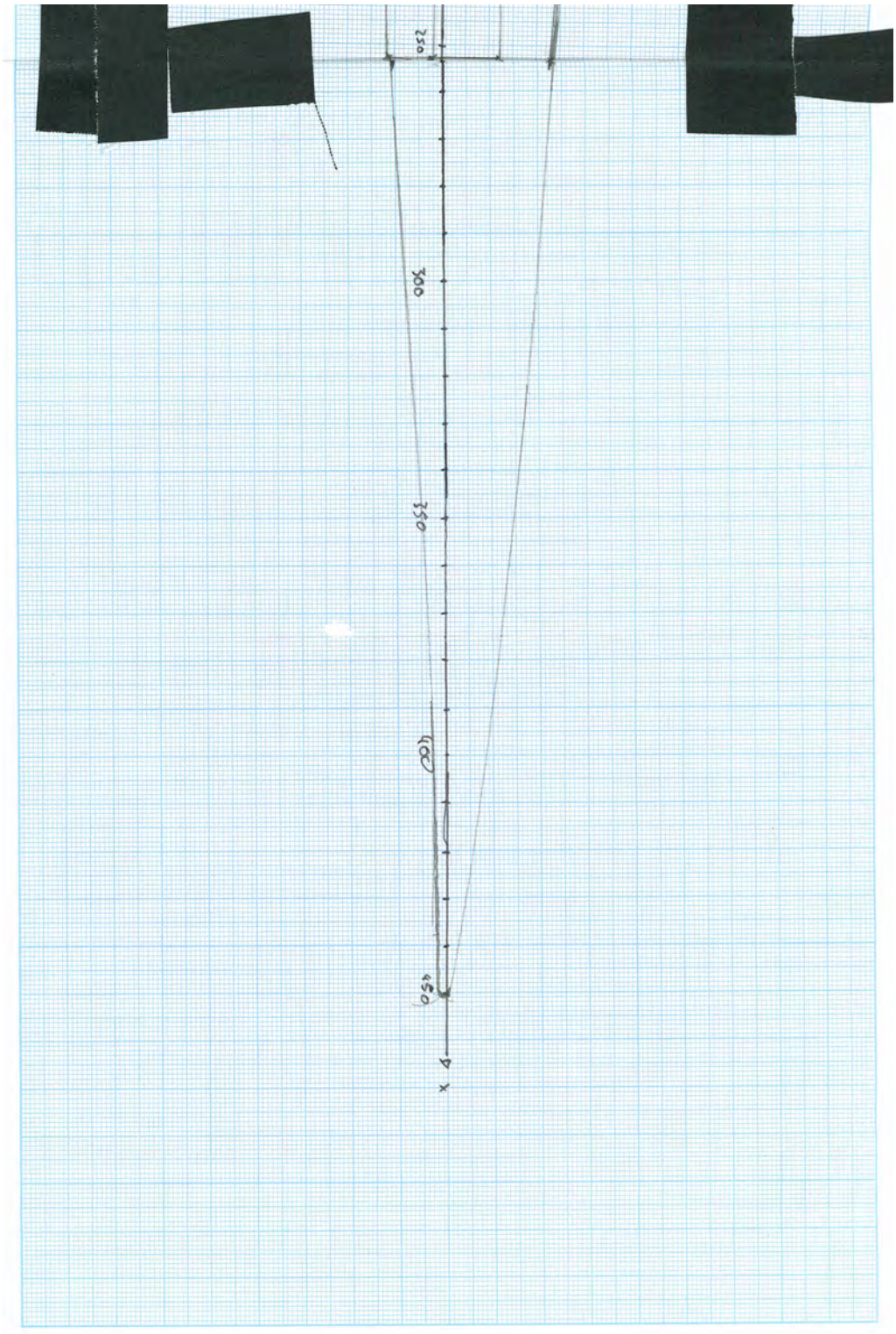

Fig. A.3.: Scan [2:2] of the wind tunnel wing model profile contour trace plot.

A.5. Six component platform balance

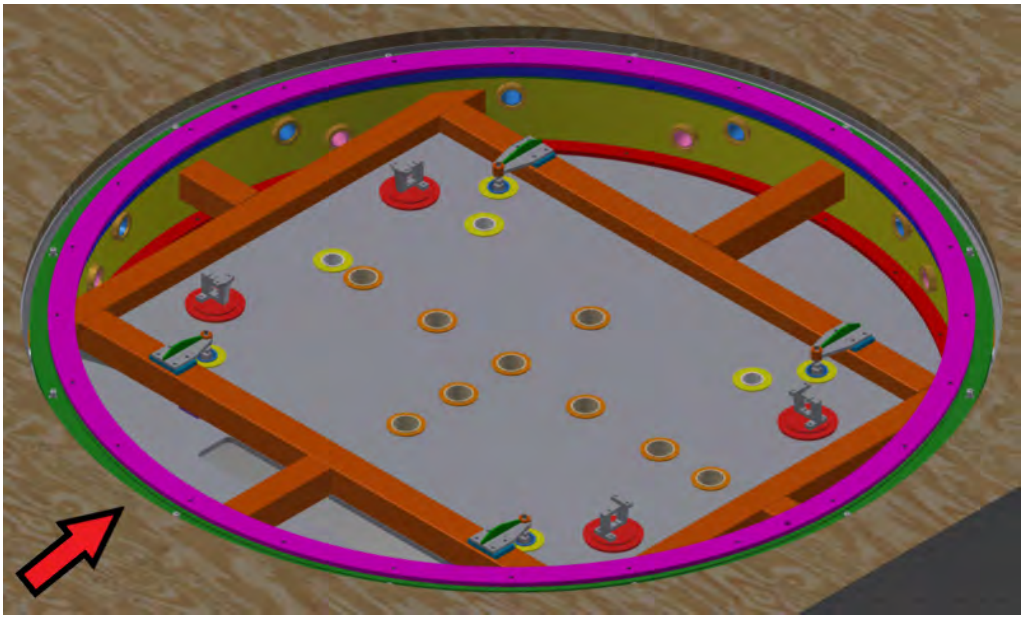

Fig. A.4.: CAD-view of the balance with its top plate removed to reveal the four lift force measuring cells visible with red base plates, the flexure suspensions of the lower plate to the orange coloured steel frame are also displayed, the red arrow indicates the flow direction. From VKI internal project report EAR1346 [52].

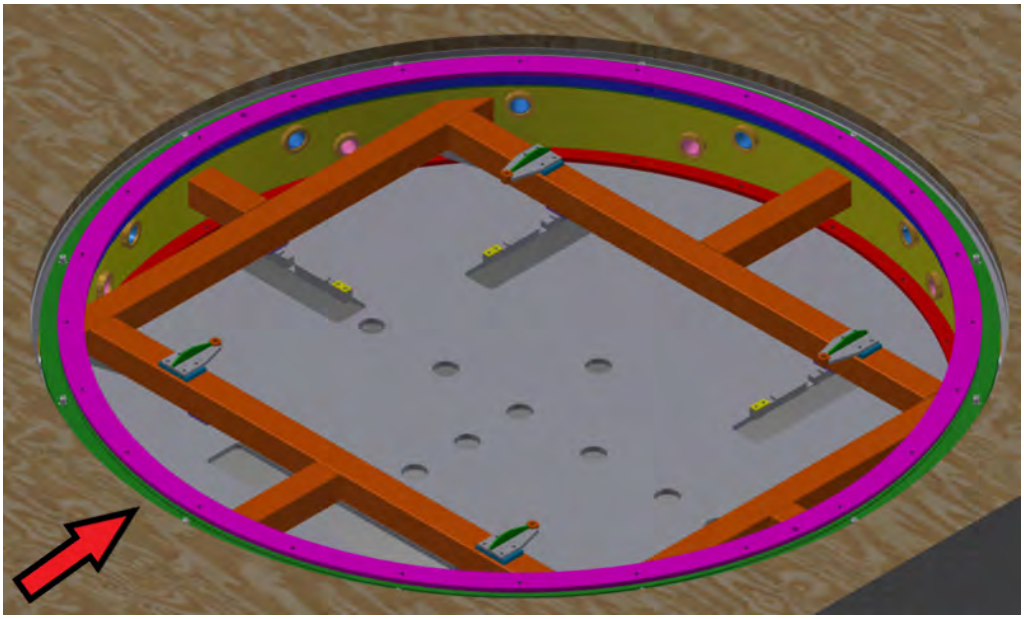

Fig. A.5.: CAD-view of the balance with lower and top plate removed to make the lateral sensors for drag, side force, and yawing moment visible, the red arrow indicates the flow direction. From VKI internal project report EAR1346 [52].

A.6. Additional experimental campaign results

A.6.1. Experimental aerodynamic coefficients at Re 200,000 second run

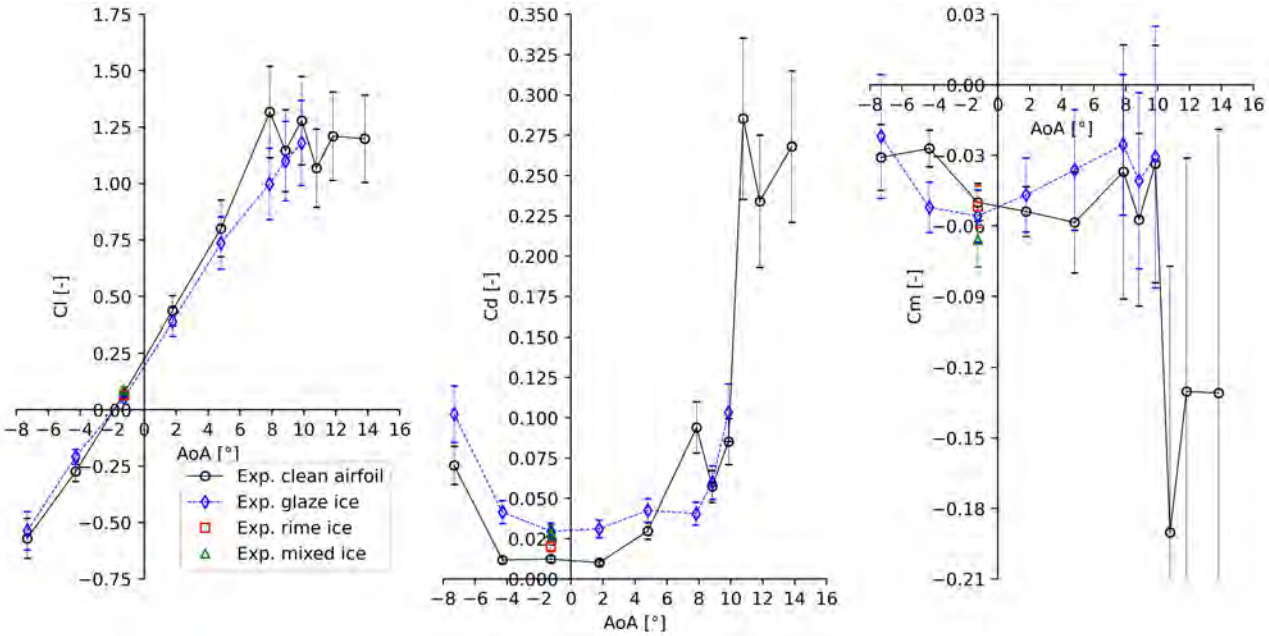

Fig. A.6.: Second velocity run plot of c_l over AoA (left), c_d over AoA (mid), and c_m over AoA (right) of the experimental campaign at Re 200,000.

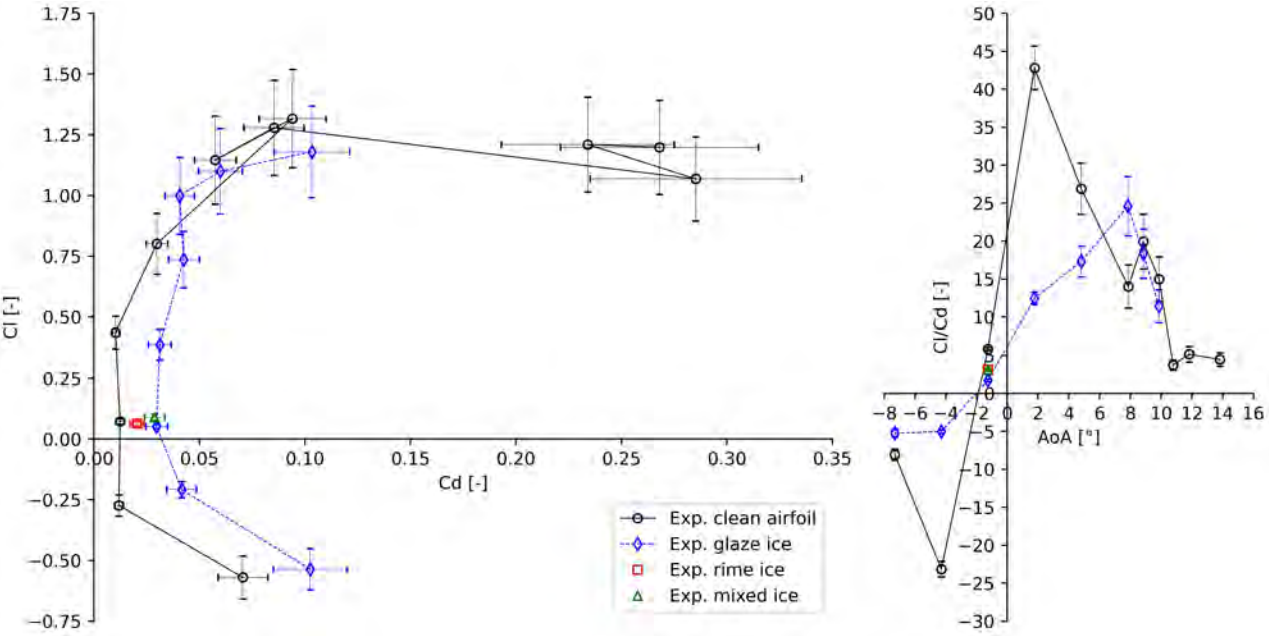

Fig. A.7.: Second velocity run plot of the drag polar (left) and the L/D ratio over AoA (right) of the experimental campaign at Re 200,000.

Tab. A.6.: Second run experimental aerodynamic penalties for Re 200,000.

Case	$\Delta c_{l,-1.3}$	$\Delta c_{d,-1.3}$	$\Delta c_{m,-1.3}$	$\Delta L/D_{-1.3}$	$\Delta\alpha_{L/D}$	$\Delta L/D$	$\Delta\partial c_m$
Glaze ice	-29%	+140%	12%	-70%	6°	-43%	$0.299\frac{1}{\text{rad}}$
Rime ice	-12%	+64%	+4%	-47%	n.a.	n.a.	n.a.
Mixed ice	+23%	+132%	+32%	-47%	n.a.	n.a.	n.a.

A.6.2. Experimental aerodynamic coefficients at Re 400,000 second run

Tab. A.7.: Second run experimental aerodynamic penalties for Re 400,000.

Case	$\Delta c_{l,-1.3}$	$\Delta c_{d,-1.3}$	$\Delta c_{m,-1.3}$	$\Delta L/D_{-1.3}$	$\Delta\alpha_{L/D}$	$\Delta L/D$	$\Delta\partial c_m$
Glaze ice	-50%	+112%	-8%	-76%	6°	-48%	$0.210\frac{1}{\text{rad}}$
Rime ice	-47%	+63%	-7%	-67%	n.a.	n.a.	n.a.
Mixed ice	-30%	+78%	-8%	-61%	n.a.	n.a.	n.a.

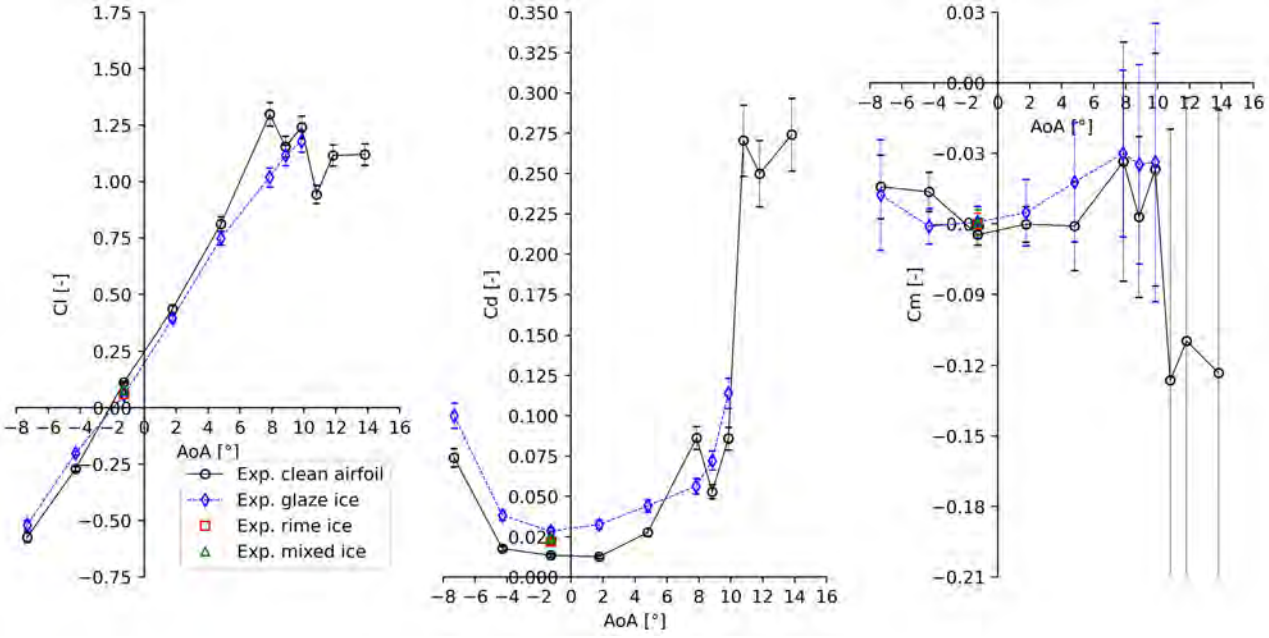

Fig. A.8.: Second velocity run plot of c_l over AoA (left), c_d over AoA (mid), and c_m over AoA (right) of the experimental campaign at Re 400,000.

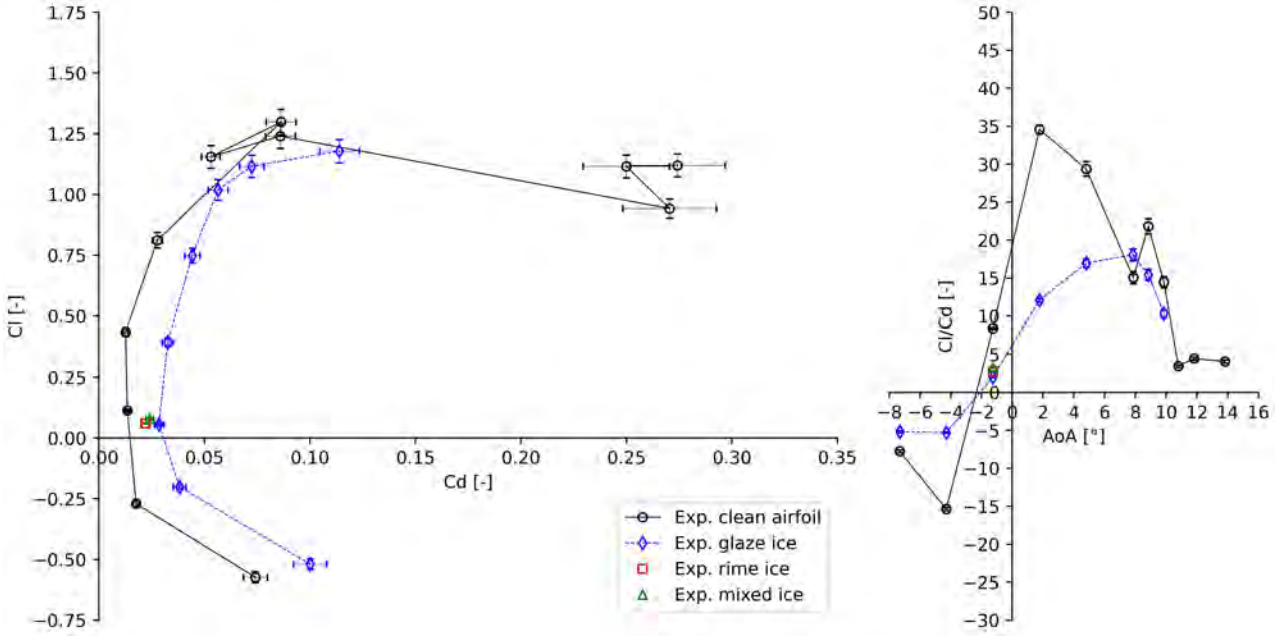

Fig. A.9.: Second velocity run plot of the drag polar (left) and the L/D ratio over AoA (right) of the experimental campaign at Re 400,000.

A.6.3. Experimental aerodynamic coefficients at Re 750,000 second run

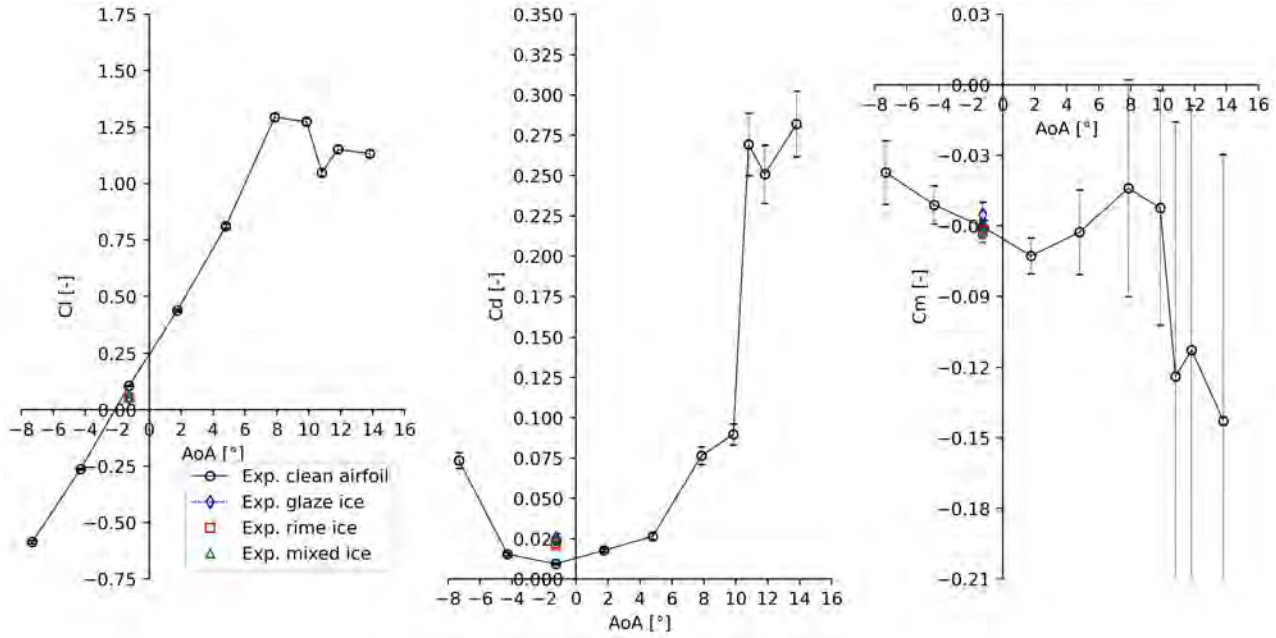

Fig. A.10.: Second velocity run plot of c_l over AoA (left), c_d over AoA (mid), and c_m over AoA (right) of the experimental campaign at Re 750,000.

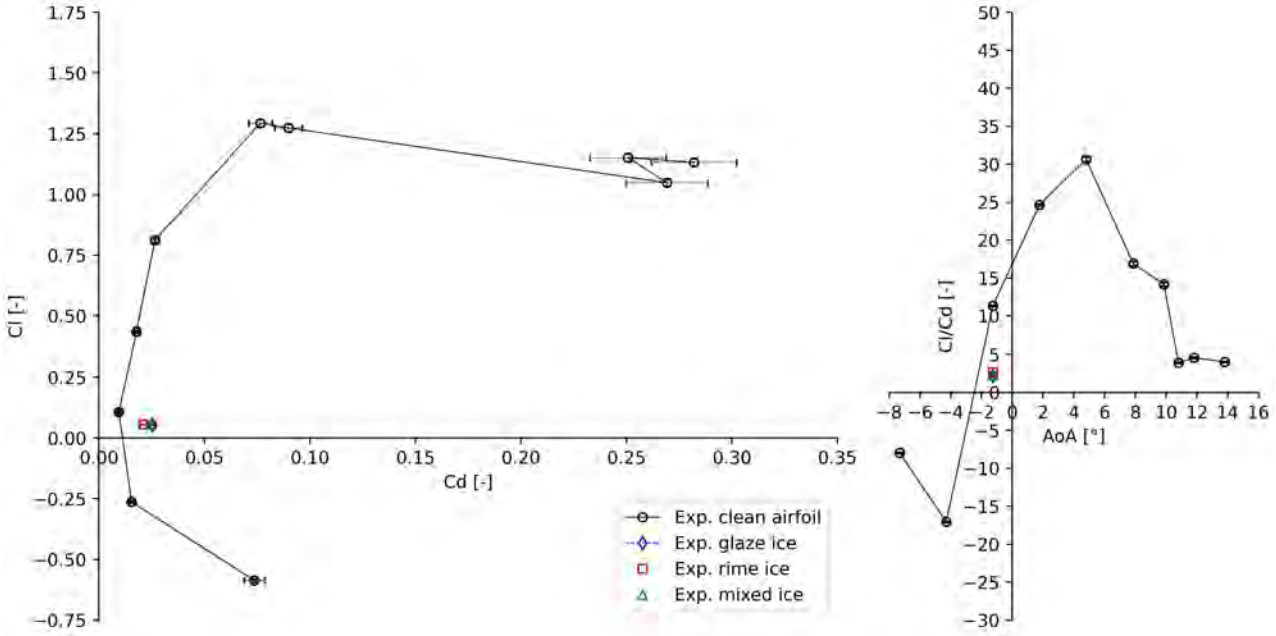

Fig. A.11.: Second velocity run plot of the drag polar (left) and the L/D ratio over AoA (right) of the experimental campaign at Re 750,000.

Tab. A.8.: Second run experimental aerodynamic penalties for Re 750,000.

Case	$\Delta c_{l,-1.3}$	$\Delta c_{d,-1.3}$	$\Delta c_{m,-1.3}$	$\Delta L/D_{-1.3}$
Glaze ice	-49%	+169%	-9%	-81%
Rime ice	-48%	+123%	+2%	-77%
Mixed ice	-47%	+161%	+4%	-80%

A.7. Velocity contour plots of the Clean RG-15C FENSAP CFD simulations

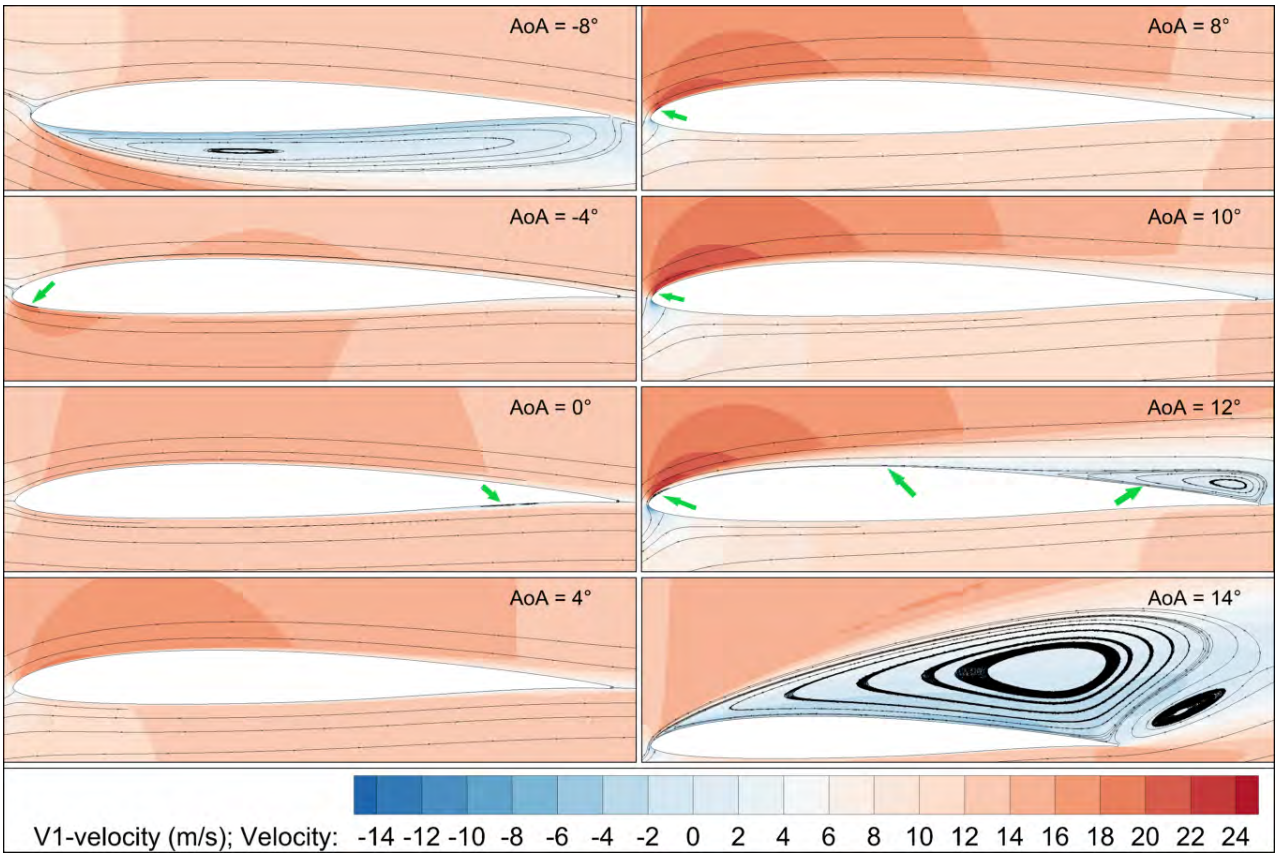

Fig. A.12.: Velocity contour plot of the RG-15C at different AoA and a Reynolds number regime of 400,000. LSB positions and the onset of bound trailing edge separation are indicated by green arrows.

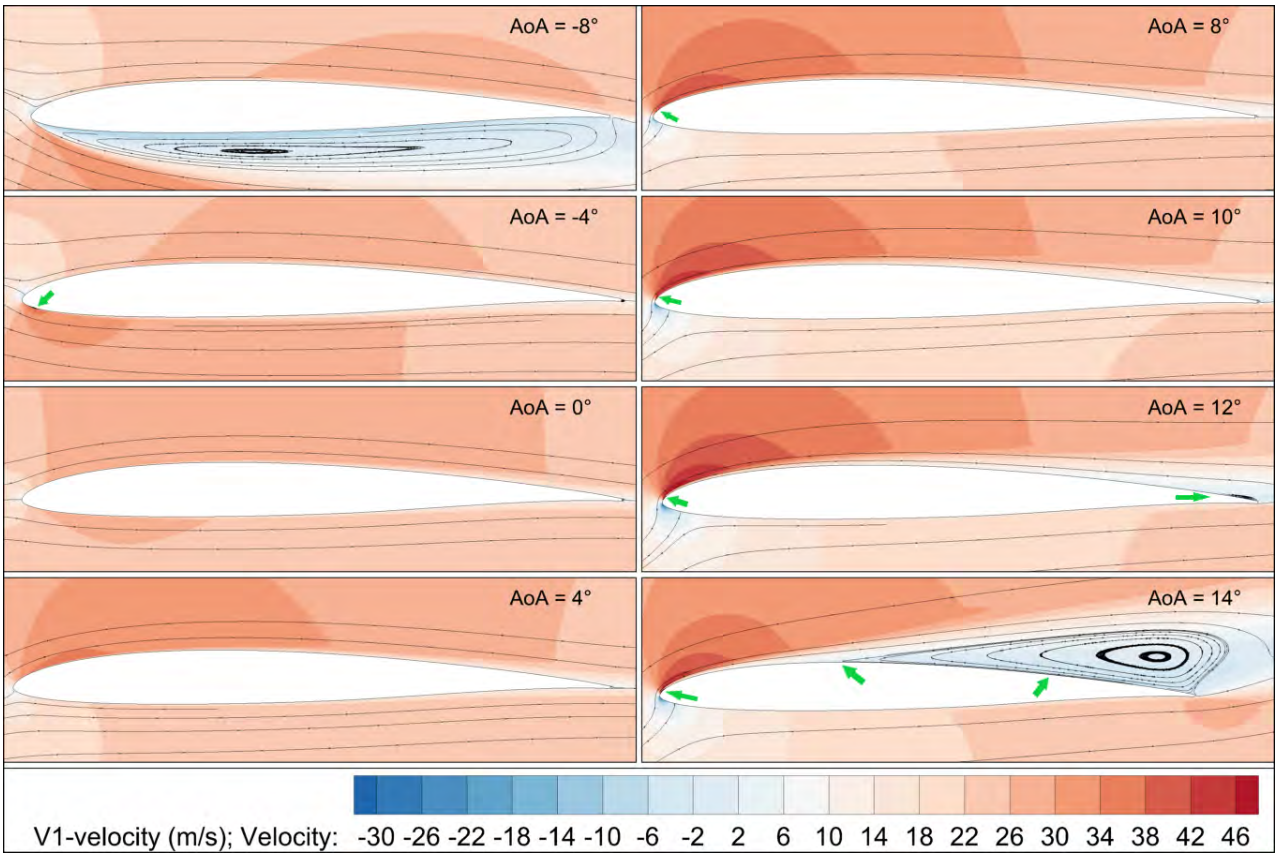

Fig. A.13.: Velocity contour plot of the RG-15C at different AoA and a Reynolds number regime of 750,000. LSB positions and the onset of bound trailing edge separation are indicated by green arrows.

A.8. Experimental Data

Tab. A.9.: First run experimental data for Re 200,000.

AoAc	c_l [-]	c_d [-]	c_m [-]	L [N]	D [N]	M [Nm]
Clean RG-15 at Re 197,400						
-7,31	-0,529	0,0406	-0,025	-4,03	0,31	-0,08
-4,29	-0,241	0,0202	-0,046	-1,82	0,15	-0,15
-1,26	0,08	0,0184	-0,056	0,61	0,14	-0,19
1,76	0,437	0,0153	-0,074	3,33	0,12	-0,26
4,8	0,769	0,0187	-0,065	5,81	0,14	-0,23
7,83	1,069	0,0462	-0,058	8,48	0,36	-0,21
8,83	1,141	0,0646	-0,074	8,76	0,49	-0,26
9,85	1,244	0,062	-0,057	9,48	0,47	-0,2
10,86	1,298	0,0809	-0,042	9,93	0,61	-0,16
11,85	1,318	0,1046	-0,059	10,24	0,81	-0,22
13,81	1,231	0,2715	-0,164	9,68	2,12	-0,58
Glaze ice at Re 196,500						
-7,34	-0,545	0,1326	-0,093	-4,2	1,01	-0,31
-4,3	-0,208	0,0498	-0,071	-1,64	0,39	-0,25
-1,26	0,051	0,0264	-0,047	0,4	0,2	-0,16
1,77	0,395	0,0269	-0,037	3,05	0,21	-0,13
4,81	0,74	0,0436	-0,03	5,67	0,33	-0,11
7,84	1,022	0,0604	-0,027	7,79	0,46	-0,1
8,84	1,074	0,0203	-0,045	8,29	0,16	-0,17
9,85	1,194	0,1364	-0,051	9,16	1,04	-0,18
Rime ice at Re 196,500						
-1,27	0,06	0,026	-0,064	0,47	0,2	-0,22
Mixed ice at Re 201,300						
-1,26	0,089	0,0241	-0,052	0,71	0,19	-0,19

Tab. A.10.: Second run experimental data for Re 200,000.

AoAc	c_l [-]	c_d [-]	c_m [-]	L [N]	D [N]	M [Nm]
Clean RG-15 at Re 199,900						
-7.32	-0.57	0.0706	-0.031	-4.5	0.55	-0.1
-4.29	-0.273	0.0118	-0.027	-2.07	0.09	-0.09
-1.26	0.072	0.0124	-0.05	0.57	0.1	-0.17
1.77	0.437	0.0102	-0.054	3.45	0.08	-0.19
4.8	0.801	0.0298	-0.059	6.21	0.23	-0.21
7.86	1.317	0.0941	-0.037	10.57	0.75	-0.14
8.84	1.146	0.0575	-0.057	8.86	0.44	-0.21
9.86	1.279	0.0853	-0.034	10.31	0.68	-0.13
10.78	1.068	0.2852	-0.19	8.52	2.26	-0.69
11.82	1.21	0.234	-0.13	9.57	1.83	-0.47
13.82	1.199	0.268	-0.131	9.59	2.12	-0.48
Glaze ice at Re 196,100						
-7.31	-0.536	0.1024	-0.022	-4.19	0.79	-0.07
-4.29	-0.208	0.0415	-0.052	-1.59	0.31	-0.18
-1.27	0.051	0.0297	-0.056	0.39	0.22	-0.19
1.77	0.388	0.0311	-0.047	2.93	0.23	-0.16
4.81	0.737	0.0425	-0.036	5.71	0.33	-0.13
7.84	0.999	0.0406	-0.025	7.69	0.31	-0.1
8.84	1.1	0.0599	-0.041	8.43	0.46	-0.15
9.85	1.18	0.1033	-0.031	9.14	0.79	-0.12
Rime ice at Re 198,500						
-1.27	0.089	0.0287	-0.066	0.7	0.22	-0.23
Mixed ice at Re 200,000						
-1,26	0,089	0,0241	-0,052	0,71	0,19	-0,19

Tab. A.11.: First run experimental data for Re 400,000.

AoAc	c_l [-]	c_d [-]	c_m [-]	L [N]	D [N]	M [Nm]
Clean RG-15 at Re 394,600						
-7.32	-0.523	0.0491	-0.04	-16.18	1.51	-0.54
-4.29	-0.235	0.0185	-0.049	-7.17	0.56	-0.65
-1.26	0.121	0.0132	-0.065	3.75	0.41	-0.9
1.76	0.439	0.0155	-0.072	13.66	0.48	-1.01
4.8	0.781	0.0217	-0.065	23.76	0.65	-0.91
7.83	1.099	0.047	-0.063	33.75	1.43	-0.9
8.84	1.159	0.0555	-0.063	35.54	1.69	-0.9
9.85	1.264	0.0621	-0.054	38.7	1.88	-0.78
10.86	1.342	0.0749	-0.049	41.24	2.28	-0.72
11.86	1.375	0.0859	-0.046	41.6	2.58	-0.67
13.82	1.282	0.2588	-0.134	39.63	7.93	-1.89
Glaze ice at Re 389,500						
-7.32	-0.522	0.1042	-0.058	-16.18	3.2	-0.78
-4.29	-0.201	0.0392	-0.063	-6.13	1.18	-0.85
-1.26	0.056	0.0253	-0.052	1.71	0.76	-0.7
1.77	0.394	0.0294	-0.048	11.89	0.88	-0.66
4.81	0.752	0.0425	-0.036	22.35	1.25	-0.5
7.84	1.027	0.0607	-0.026	30.42	1.78	-0.38
8.84	1.116	0.0778	-0.035	33.88	2.34	-0.51
9.85	1.184	0.1245	-0.041	36.28	3.78	-0.6
Rime ice at Re 389,700						
-1.27	0.061	0.0225	-0.061	1.85	0.68	-0.83
Mixed ice at Re 396,100						
-1.27	0.096	0.0276	-0.068	2.96	0.85	-0.94

Tab. A.12.: Second run experimental data for Re 400,000.

AoAc	c_l [-]	c_d [-]	c_m [-]	L [N]	D [N]	M [Nm]
Clean RG-15 at Re 396,800						
-7.32	-0.573	0.0741	-0.044	-18.07	2.31	-0.6
-4.29	-0.271	0.0176	-0.046	-8.39	0.54	-0.63
-1.26	0.113	0.0134	-0.065	3.52	0.42	-0.9
1.77	0.435	0.0126	-0.06	13.72	0.39	-0.86
4.8	0.812	0.0276	-0.061	25.01	0.84	-0.87
7.86	1.299	0.0863	-0.033	39.77	2.62	-0.5
8.84	1.155	0.053	-0.057	35.62	1.62	-0.83
9.86	1.24	0.0859	-0.037	38.1	2.62	-0.55
10.79	0.943	0.2704	-0.126	29.41	8.37	-1.79
11.82	1.116	0.2499	-0.11	34.6	7.68	-1.55
13.81	1.12	0.2741	-0.123	34.95	8.48	-1.75
Glaze ice at Re 390,200						
-7.32	-0.519	0.1001	-0.048	-16.16	3.08	-0.64
-4.29	-0.201	0.0382	-0.061	-6.16	1.16	-0.82
-1.27	0.057	0.0284	-0.059	1.74	0.86	-0.81
1.77	0.394	0.0326	-0.055	11.93	0.98	-0.76
4.81	0.749	0.0442	-0.042	22.4	1.31	-0.59
7.84	1.019	0.0564	-0.03	30.27	1.66	-0.43
8.84	1.116	0.0723	-0.035	33.99	2.18	-0.51
9.85	1.179	0.114	-0.034	36.26	3.48	-0.51
Rime ice at Re 390,600						
-1.27	0.06	0.0219	-0.06	1.84	0.66	-0.82
Mixed ice at Re 397,900						
-1.27	0.079	0.024	-0.06	2.47	0.74	-0.83

Tab. A.13.: First run experimental data for Re 750,000.

AoAc	c_l [-]	c_d [-]	c_m [-]	L [N]	D [N]	M [Nm]
Clean RG-15 at Re 747,600						
-7.32	-0.583	0.0724	-0.04	-64.73	7.96	-1.88
-4.3	-0.26	0.0168	-0.054	-28.61	1.84	-2.6
-1.26	0.107	0.0112	-0.064	11.89	1.24	-3.15
1.76	0.438	0.0188	-0.075	48.09	2.05	-3.71
4.8	0.826	0.0273	-0.068	91.18	2.99	-3.43
7.85	1.282	0.0661	-0.055	141.26	7.22	-2.87
9.86	1.301	0.0834	-0.053	143.86	9.14	-2.79
10.81	1.122	0.2566	-0.117	122.41	27.77	-5.81
11.84	1.238	0.2049	-0.087	136.6	22.42	-4.46
13.81	1.165	0.2782	-0.144	128.24	30.36	-7.2
Glaze ice at Re 737,000						
-1.27	0.056	0.0259	-0.057	6.06	2.8	-2.75
Rime ice at Re 736,400						
-1.27	0.055	0.0215	-0.063	6	2.32	-3.05
Mixed ice at Re 751,700						
-1.27	0.074	0.0244	-0.064	8.3	2.7	-3.2

Tab. A.14.: Second run experimental data for Re 750,000.

AoAc	c_l [-]	c_d [-]	c_m [-]	L [N]	D [N]	M [Nm]
Clean RG-15 at Re 747,600						
-7.32	-0.586	0.0736	-0.037	-65.32	8.12	-1.77
-4.29	-0.263	0.0154	-0.051	-28.99	1.69	-2.48
-1.26	0.107	0.0094	-0.06	11.83	1.04	-3
1.76	0.438	0.0178	-0.073	48.37	1.95	-3.64
4.8	0.811	0.0265	-0.063	89.81	2.91	-3.2
7.86	1.294	0.0765	-0.044	142.64	8.36	-2.33
9.85	1.274	0.0898	-0.052	141.03	9.86	-2.75
10.8	1.049	0.2692	-0.124	114.89	29.24	-6.18
11.82	1.152	0.2508	-0.113	127.57	27.54	-5.7
13.81	1.133	0.282	-0.143	124.79	30.8	-7.15
Glaze ice at Re 737,000						
-1.27	0.055	0.0253	-0.055	5.97	2.74	-2.69
Rime ice at Re 736,400						
-1.27	0.055	0.021	-0.062	6.01	2.27	-2.99
Mixed ice at Re 751,700						
-1.27	0.056	0.0246	-0.063	6.3	2.72	-3.12